

Report Title

Final Report

InP Transferred Electron Cathodes: Basic to Manufacturing Methods

Grant No. DAAD19-02-1-0396

ABSTRACT

InP has gained an emerging importance as a negative electron affinity (NEA) transferred electron photocathode (TEP) material in imaging technologies. InP provides itself as a substrate to grow these small band gap materials, and also serves as an efficient electron emitter with a low work function at the surface. The high quantum efficiency (QE) of these TEP is realized by depositing Cs and O₂ on the surface of heavily doped p-type semiconductors, where they form the thin activation layer. The atomic structure of this Cs/O activation layer is, however, not well-known, and the properties of photoelectrons from InP-based cathodes also require careful study. In this study, InP photocathodes were studied in three parts: (1) the atomic arrangement of Cs oxides in the activation layer, (2) the decay mechanism of InP photocathodes in an open UHV system and the simulation of commercial sealed photocathode tubes for the elongation of lifetime, and (3) the energy and angular distribution of photoelectrons from InP photocathodes.

List of papers submitted or published that acknowledge ARO support during this reporting period. List the papers, including journal references, in the following categories:

(a) Papers published in peer-reviewed journals (N/A for none)

Preparation of clean InP(100) surfaces studied by synchrotron radiation photoemission Sun, Y; Liu, Z; Machuca, F; Pianetta, P; Spicer, WE
Source: Journal of Vacuum Science and Technology A: Vacuum, Surfaces and Films; January/February 2003; v.21, no.1, p.219-225

Optimization and characterization of III-V surface cleaning Liu, Z; Sun, Y; Machuca, F; Pianetta, P; Spicer, WE; Pease, RFW
Source: Journal of Vacuum Science and Technology B: Microelectronics and Nanometer Structures; July/August 2003; v.21, no.4, p.1953-1958

Optimized cleaning method for producing device quality InP(100) surfaces Sun, Y; Liu, Z; Machuca, F; Pianetta, P; Spicer, WE
Source: Journal of Applied Physics; June 2005; v.97, p. 124902

Surface dipole formation and lowering of the work function by Cs adsorption on InP(100) surface Sun, Y; Liu, Z; Pianetta, P
Source: Journal of Vacuum Science and Technology A: Vacuum, Surfaces and Films; Sept/Oct 2007 V. 25, No. 5

Number of Papers published in peer-reviewed journals: 4.00

(b) Papers published in non-peer-reviewed journals or in conference proceedings (N/A for none)

Number of Papers published in non peer-reviewed journals: 0.00

(c) Presentations

Decay Mechanism of Negative Electron Affinity (Cs/O Activated) InP(100) Photocathode Yun Sun, Dong-ick Lee, Zhi Liu, Shiyu Sun, Piero Pianetta AVS 53rd International Symposium, San Francisco CA, Nov. 2006

Angular Dependent Energy Distribution Curve Measurements of InP NEA Photocathode Yun Sun, Dong-ick Lee, Zhi Liu, Shiyu Sun, Piero Pianetta 33rd SSRL user meeting, Menlo Park CA, Oct. 2006

Nature of Cs/O complex on a III-V semiconductor photocathode Dong-Ick Lee, Yun Sun, Zhi Liu, Shiyu Sun, Piero Pianetta 32nd SSRL user meeting, Menlo Park CA, Oct. 2005

Synchrotron Radiation Photoemission Study of Cs/O co-adsorbed InP(100) for applications in NEA devices Dong-Ick Lee, Shiyu Sun, Samuel P. A. Peterson, Zhi Liu, Yun Sun, William E. Spicer, Piero Pianetta, the Materials Research Society 2005 Spring Meeting, San Francisco, CA, 03/2005

Synchrotron Radiation Photoemission Study on Cs/O co-adsorbed InP(100) for applications in NEA devices Dong-Ick Lee, Shiyu Sun, Zhi Liu, William E Spicer, Piero Pianetta, The Physical Electronics Conference, Davis, CA, 06/2004

Cs/O Activation of III-V Semiconductors as Negative Electron Affinity Photocathodes: InP, GaAs and GaN Yun Sun, Zhi Liu, Francisco Machuca, Piero Pianetta, William E Spicer and Fabian Pease 29th SSRL user meeting, Meolo Park CA, 10/2002

Synchrotron Radiation Photoemission Study of Surface Cleaning Chemistry of InP(100) by Hydrogen Peroxide Based Solutions Yun Sun, Zhi Liu, Francisco Machuca, Piero Pianetta and William E Spicer 2002 Material Research Society (MRS) Spring Meeting, April1-5, 2002

The Study of InP(100) Chemical Cleaning by Synchrotron Radiation Photoemission Spectroscopy Yun Sun, Zhi Liu, Francisco Machuca, Piero Pianetta and William E Spicer IUVSTA 15th International Vacuum Congress, AVS 48th International Symposium, 11th International Conference on Solid Surfaces, Oct. 28 – Nov. 2, 2001

Number of Presentations: 8.00

Non Peer-Reviewed Conference Proceeding publications (other than abstracts):

Number of Non Peer-Reviewed Conference Proceeding publications (other than abstracts): 0

Peer-Reviewed Conference Proceeding publications (other than abstracts):

Number of Peer-Reviewed Conference Proceeding publications (other than abstracts): 0

(d) Manuscripts

Formation of Cesium Peroxide and Cesium Superoxide on InP Photocathode Activated by Cesium and Oxygen Sun, Y; Liu, Z; Lee, D; Pianetta, P; Accepted by Journal of Applied Physics

The Distribution of Oxide Species in the Cs/O Activation Layer on InP(100) Negative Electron Affinity Photocathodes Lee, D; Sun, Y; Liu, Z; Sun, S; Peterson, S; Pianetta, P; Accepted by Journal of Applied Physics

Angular dependence of photoelectron energy distribution of InP(100) and GaAs(100) negative electron affinity photocathodes Lee, D; Sun, Y; Liu, Z; Sun, S; Pianetta, P; submitted Applied Physics Letters

Number of Manuscripts: 3.00

Number of Inventions:

Graduate Students

| <u>NAME</u> | <u>PERCENT SUPPORTED</u> |
|------------------------|--------------------------|
| Dong-Ick Lee | 0.50 |
| FTE Equivalent: | 0.50 |
| Total Number: | 1 |

Names of Post Doctorates

| <u>NAME</u> | <u>PERCENT SUPPORTED</u> |
|------------------------|--------------------------|
| FTE Equivalent: | |
| Total Number: | |

Names of Faculty Supported

| <u>NAME</u> | <u>PERCENT SUPPORTED</u> | National Academy Member |
|------------------------|--------------------------|-------------------------|
| Piero Pianetta | 0.10 | No |
| William E. Spicer | 0.20 | No |
| FTE Equivalent: | 0.30 | |
| Total Number: | 2 | |

Names of Under Graduate students supported

| <u>NAME</u> | <u>PERCENT SUPPORTED</u> |
|------------------------|--------------------------|
| FTE Equivalent: | |
| Total Number: | |

Student Metrics

This section only applies to graduating undergraduates supported by this agreement in this reporting period

| | |
|--|------|
| The number of undergraduates funded by this agreement who graduated during this period: | 0.00 |
| The number of undergraduates funded by this agreement who graduated during this period with a degree in science, mathematics, engineering, or technology fields:..... | 0.00 |
| The number of undergraduates funded by your agreement who graduated during this period and will continue to pursue a graduate or Ph.D. degree in science, mathematics, engineering, or technology fields:..... | 0.00 |
| Number of graduating undergraduates who achieved a 3.5 GPA to 4.0 (4.0 max scale): | 0.00 |
| Number of graduating undergraduates funded by a DoD funded Center of Excellence grant for Education, Research and Engineering: | 0.00 |
| The number of undergraduates funded by your agreement who graduated during this period and intend to work for the Department of Defense | 0.00 |
| The number of undergraduates funded by your agreement who graduated during this period and will receive scholarships or fellowships for further studies in science, mathematics, engineering or technology fields: | 0.00 |

Names of Personnel receiving masters degrees

| <u>NAME</u> |
|----------------------|
| Dong-Ick Lee |
| Total Number: |

Names of personnel receiving PhDs

NAME

Steven (Yun) Sun

Zhi Liu

Dong-Ick Lee

Total Number:

3

Names of other research staff

NAME

PERCENT SUPPORTED

FTE Equivalent:

Total Number:

Sub Contractors (DD882)

Inventions (DD882)

Final Report

InP Transferred Electron Cathodes: Basic to Manufacturing Methods

Grant No. DAAD19-02-1-0396

P. Pianetta, D. Lee, Y. Sun, Z. Liu, W. E. Spicer

ABSTRACT

InP has gained an emerging importance as a negative electron affinity (NEA) transferred electron photocathode (TEP) material in imaging technologies due to its lattice matching with small and variable band gap materials such as $\text{Ga}_x\text{In}_{1-x}\text{As}_y\text{P}_{1-y}$. InP provides itself as a substrate to grow these small band gap materials, and also serves as an efficient electron emitter with a low work function at the surface. The high quantum efficiency (QE) of these TEP is realized by depositing Cs and O_2 on the surface of heavily doped p-type semiconductors, where they form the thin activation layer. The atomic structure of this Cs/O activation layer is, however, not well-known, and the properties of photoelectrons from InP-based cathodes also require careful study. In this study, InP photocathodes were studied in three parts: (1) the atomic arrangement of Cs oxides in the activation layer, (2) the decay mechanism of InP photocathodes in an open UHV system and the simulation of commercial sealed photocathode tubes for the elongation of lifetime, and (3) the energy and angular distribution of photoelectrons from InP photocathodes.

The atomic arrangement of Cs oxides was investigated by Angle Dependent Photoemission Spectroscopy (ADPES). Two distinct peaks in our $\text{O}1s$ core level and

valence band spectra led to the discovery of molecular oxygen species incorporated in the thin activation layer; Cs peroxides (O_2^{2-}) and Cs superoxides (O_2^-). The different angular dependences of these oxides in the photoemission spectra result from the different vertical locations of oxygen molecules in each Cs oxide, and the lateral distribution model of Cs peroxides and Cs superoxides was suggested based on this angular dependence and the estimated thickness of Cs/O layer ($\sim 7\text{\AA}$). Linear squares fitting of ADPES data based on this model was performed, and good agreement between calculation and experimental data was achieved.

The QE of InP photocathodes in an open UHV system decreases with time, while commercial sealed photocathode tubes last for years without decay. This QE decay is due to the chemical transformation from Cs peroxides to Cs superoxides and subsequent substrate oxidation as observed on the peak evolutions in the valence band, O1s core level, and In4d core level photoemission spectra. This transformation is thermodynamically favorable when residual oxygen is available, and the decrease of Cs peroxides is in agreement with the lateral distribution model. The simulation of commercial sealed tubes was performed by repetitively dosing Cs atoms during decay, which is called ‘recesiation’, since sealed tubes have Cs overpressure environment. It is found that the QE can be maintained at a certain level by recesiation since redeposited Cs atoms partially recover the weakened dipoles in Cs/O activation layer and prevent Cs peroxides from transforming to Cs superoxide by acting as a protect layer against residual oxygen. The long-term QE decay, however, cannot be avoided due to the substrate oxidation.

Finally, this work is directed toward to the energy and angular distribution of photoelectrons from InP photocathodes. These properties have the practical importance in terms of the resolution and focusing capability of photocathodes. Two different kinds of photoelectrons were observed in energy distribution curve (EDC) measurements. They are thermalized electrons in Γ valley and electrons transferred into L valley, and we observed the increase of L valley electrons when higher photon energy is used. The L valley electrons have larger angular distribution than Γ valley electrons, and this can be explained by larger effective mass of L valley than Γ valley. Better beam properties can be expected from Γ valley electron because of its narrow angular spread, but L valley emission cannot be avoided if higher QE is needed.

TABLE OF CONTENTS

| | |
|--|-----------|
| 1. INTRODUCTION | 1 |
| 1.1 Introduction | 1 |
| 1.2 NEA Photocathodes: Applications in Night Vision, and Principles | 3 |
| 1.2.1 NEA Photocathodes and Traditional Night Vision Devices | 3 |
| 1.2.2 Next Generation Night Vision Devices | 4 |
| 1.2.3 Spicer Three-Step Model | 5 |
| 1.3 InP Material Properties | 7 |
| 1.4 Techniques | 8 |
| 1.4.1 Photoemission Spectroscopy (PES) | 8 |
| 1.4.2 Synchrotron Radiaton | 10 |
| 1.4.3 Near Edge X-ray Absorption Fine Structure (NEXAFS) | 10 |
| 1.4.4 Instrument | 12 |
| 1.5 Overview of the Dissertation | 12 |
| 1.6 References | 14 |
| | |
| 2. ACTIVATION LAYER OF INP(100) PHOTOCATHODES | 26 |
| 2.1 Introduction | 26 |
| 2.2 Experiment | 27 |
| 2.3 Results & Discussion | 28 |
| 2.3.1 Angle-Dependent Photoemission Spectroscopy (ADPES) | 28 |

| | |
|--|-----------|
| Measurements | |
| 2.3.2 Time Decay Results of ADPES of Valence Band | 33 |
| 2.4 Conclusion | 35 |
| 2.5 References | 36 |
| | |
| 3. DECAY MECHANISM OF INP(100) PHOTOCATHODE | 50 |
| 3.1 Introduction | 50 |
| 3.2 Experiment | 51 |
| 3.3 Results & Discussion | 51 |
| 3.3.1 Decrease in Photocurrent and Chemical Changes during Decay | 51 |
| 3.3.2 Recesiation Experiments | 60 |
| 3.4 Conclusion | 63 |
| 3.5 References | 63 |
| | |
| 4. ENERGY AND ANGULAR DISTRIBUTION OF PHOTOELECTRONS FROM INP(100) PHOTOCATHODE | 79 |
| 4.1 Introduction | 79 |
| 4.2 Experimental | 80 |
| 4.3 Results & Discussion | 82 |
| 4.3.1 Identification of the Origin of Photoelectrons | 82 |
| 4.3.2 Angular Distribution of Photoelectrons with Room Light | 86 |
| 4.3.3 Angular Distribution of Photoelectrons using Monochromatic Light | 90 |
| | 92 |

| | | |
|------------|--|------------|
| 4.3.4 | Energy Distribution at Different Biases | 94 |
| 4.3.5 | Inter-valley Scattering in the Band Bending Region | 95 |
| 4.3.6 | Energy Distribution after QE Decay | |
| 4.4 | Conclusion | 97 |
| 4.5 | References | 98 |
| | | |
| 5. | CONCLUSION | 117 |
| | | |
| 5.1 | Overview | 117 |
| | | |
| 5.2 | Contributions | 117 |
| | | |
| 5.3 | Future Work | 119 |

LIST OF FIGURES

Chapter 1 Introduction

- Figure 1.1** The process of photoemission from negative electron affinity photocathode: step 1 is the excitation of electrons, step 2 is the transport of electrons to the surface, and step 3 is the escape of electrons into the vacuum. **18**
- Figure 1.2** The schematic diagram of the image-intensifying process in a night vision tube **19**
- Figure 1.3** Electron Bombarded CCD (EBCCD) diagram is presented. **20**
- Figure 1.4** The absorption of photon in the semi-infinite slab is described. **21**
- Figure 1.5** Zincblende structure. a is a lattice constant. **22**
- Figure 1.6** Lattice constants and band-gaps of various III-V compound semiconductors **23**
- Figure 1.7** In4d fitting of a clean surface and an activated surface **24**
- Figure 1.8** Schematic diagram of the PES system viewed from above. A hemispherical analyzer is mounted at the magic angle with respect to the incoming photon beam. Thermocouple and Cs doser are also available. **25**

Chapter 2 Activation layer of InP photocathodes

- Figure 2.1** QE vs Time curve during activation. For this activation, there was no need to modulate the amount of oxygen once it is initially matched with Cs

| | | |
|-------------------|---|----|
| | flux. The normal cases of activation require further modulations of the amount of oxygen. | 39 |
| Figure 2.2 | Sample configuration with respect to the analyzer. In the configuration of (a), the probing depth is maximized to deliver relatively bulk sensitive information, while in the (b) configuration the probing depth is small so it is more surface sensitive. | 40 |
| Figure 2.3 | ADPES valence band spectra at $h\nu = 70$ eV (solid line: 90° emission angle, dotted line: 30° emission angle) at different times after activation. (a) 5 minutes (b) 70 minutes (c) 148 minutes (d) 424 minutes after activation | 41 |
| Figure 2.4 | O1s core level spectra at $h\nu = 640$ eV. Spectra are taken at four different emission angles. The 90° emission angle is the most bulk sensitive, while the 30° emission angle is the most surface sensitive. | 42 |
| Figure 2.5 | Polarization at each incidence angle (a) P-polarization at glancing incidence angle (b) S-polarization at normal incidence angle | 43 |
| Figure 2.6 | NEXAFS of O K-edge data on InP photocathode at different times after activation with (a) a glancing incidence angle (p-polarization) (b) a normal incidence angle (s-polarization) | 44 |
| Figure 2.7 | Layer model of cesium superoxides and peroxides in the activated surface of InP(100) photocathode. The total thickness of the activation layer (t) is $\sim 7\text{\AA}$. | 45 |
| Figure 2.8 | (a) Bulk Cs superoxide: calcium carbide structure (b) Bulk Cs peroxide: distorted calcium fluorite structure | 46 |

| | | |
|--------------------|--|-----------|
| Figure 2.9 | Relative intensity of peroxides ($I_s/(I_s+I_p)$) plot vs the emission angle and relative intensity of superoxides ($I_s/(I_s+I_p)$) plot vs the emission angle | 47 |
| Figure 2.10 | Valence band spectra at different times and at different take off angles. 90° take off angle is the most bulk sensitive, and 30° take off angle is the most surface sensitive. | 48 |
| Figure 2.11 | VB and O1s core level spectra at different angles and different times (a) VB photoemission spectra at 70 eV (b) O1s core level spectra at 640 eV photon energy | 49 |
| Chapter 3 | Decay mechanism of InP photocathodes | |
| Figure 3.1 | Decrease of photocurrent with time at different chamber pressures | 65 |
| Figure 3.2 | Band diagram of the NEA surface under an applied bias between the sample and an analyzer | 66 |
| Figure 3.3 | Electron Affinity (χ) at different times after activation. The electron affinity is calculated from the measured low KE cutoff of an energy distribution curve. The electron affinity at the beginning of decay is negative thus NEA. | 67 |
| Figure 3.4 | Photoemission spectra of an activated InP(100) sample at different times after activation. (a) O1s core level spectra at $h\nu = 640$ eV (b) valence band spectra at $h\nu = 70$ eV | 68 |
| Figure 3.5 | In4d core level spectra at different times after activation. In_bulk, In_Cs, and In_Ox are a bulk peak, Cs-induced peak, and oxide peak of In4d core level. They are resolved by the peak fitting of the spectra with the | |

branching ratio of 0.667, the spin-orbit splitting of 0.86, and the lorentzian width of 0.1. 69

Figure 3.6 (a) Band diagram and surface potential before building up the dipoles by activation (b) Surface potential decreases in a linear way by the formation of dipoles so photoelectrons can tunnel through and escape to the vacuum (c) Simplified band diagram because of the thin Cs/O layer 70

Figure 3.7 Schematic diagram of the transformation of Cs oxides in Cs/O layer based on the simplified structural model. (a) Residual oxygen molecules from a chamber approach the activation layer (b) oxygen molecules are placed on the plane of the first layer of Cs of Cs peroxide (c) the original oxygen molecules in Cs peroxide are forced down to the second layer of Cs (d) the oxygen molecules in the second layer of Cs dissociate and oxidize the InP substrate. 71

Figure 3.8 The log plot of Cs peroxide concentration vs time. Linear fitting was performed providing the time constant by taking the slope ($-1/\tau$) of a line. Time constant is found to be 32.7 hr. 72

Figure 3.9 The change in the coverage of Cs superoxide (ΔX_s) and the change in the coverage of Cs peroxide (ΔX_p) were plotted as the time decay proceeds. The discrepancy between two coverage changes is due to the substrate oxide in the O1s core level spectra. 73

Figure 3.10 The graph of the photocurrent vs. time. Recesiations were performed during decay as indicated in the graph 74

| | | |
|--------------------|---|------------|
| Figure 3.11 | (a) The graph of the photocurrent vs. time. Recesiations were performed after 7 hours during decay as indicated in the graph, the features before 7 hours are due to the results of recesiations in the early state of decay. (b) the photoemission spectra of O1s core level during recesiations. The peroxide peak remains at the same intensity, and the superoxide peak grows slightly. | 75 |
| Figure 3.12 | The graph of the photocurrent vs. time. (a) recesiation starts at ~7 hrs after activation, which is repeated for 8 hrs. (b) The enlarged curve of the first recesiation cycle. | 76 |
| Figure 3.13 | The model for the increase of the vacuum level. There are two contributions. one is due to the transformation of Cs peroxide and the other is due to substrate oxidation. | 77 |
| Figure 3.14 | A recesiation effect on the photocurrent vs time curve is explained by the model in Figure 3.13 | 78 |
| Chapter 4 | Energy and angular distribution of photoelectrons from INP(100) phtocathodes | |
| Figure 4.1 | Experimental setup for the energy distribution curve measurements | 100 |
| Figure 4.2 | EDCs of a InP photocathode taken at $h\nu = 2.1$ eV with different slit sizes. The intensities are normalized to the same height. Without normalization, the intensity of larger slit size is much higher than the intensity of smaller slit size. | 101 |
| Figure 4.3 | Calibration of the number of photons at each wavelength for the 600 l/mm, | |

| | | |
|--------------------|---|-----|
| | 750 nm blazing wavelength grating. | 102 |
| Figure 4.4 | Photocurrent vs photon energy curve, normally called “Yield Curve”. Photocurrent was obtained by measuring the drain current of sample. | 103 |
| Figure 4.5 | Band diagram with a surface band bending. The amount of the band bending is the subtraction of $E_F - E_{VBM, bulk}$ (b) from $E_F - E_{VBM, surface}$ (a). (a) is measured from the valence band photoemission spectra of InP and Au. (b) is calculated from the doping concentration of the sample. | 104 |
| Figure 4.6 | Energy distribution curve of InP photocathode at 1.96 eV photon energy with He-Ne Laser. | 105 |
| Figure 4.7 | Energy distribution curve of InP photocathode at 2.05 eV photon energy with 4 V bias between the sample and the electron energy analyzer. | 106 |
| Figure 4.8 | Energy distribution curves taken at different photon energy. Applied bias was 4V. All of spectra was normalized by the number of photons. | 107 |
| Figure 4.9 | InP band structure | 108 |
| Figure 4.10 | Angle-Dependent Energy Distribution Curve (AREDC) of InP photocathodes with room light (a) off-normal emission angles in one way (b) off-normal angles in the other way | 109 |
| Figure 4.11 | InP photocathode activated by Cs/O. (a) Low energy cutoff of EDC at different off-normal angle (b) Intensity of EDC at different off-normal angle | 110 |
| Figure 4.12 | Angular Dependent Energy Distribution Curve (ADEDC) of InP photocathode with 500 nm (2.46 eV) light excitation at 4V bias. All the angles are shifted by 15° to compensate the deflection we observed in our | |

| | | |
|--------------------|--|-----|
| | experiments. | 111 |
| Figure 4.13 | Angle-Dependent Energy Distribution Curve (ADEDC) of GaAs photocathodes with 500 nm (2.46 eV) light excitation at 4V bias. All the angles are shifted by 15° to compensate the deflection we observed in our experiments. | 112 |
| Figure 4.14 | Energy distribution curves taken with different biases. Photon energy was 2.05 eV. All of spectra was normalized by the number of photons. | 113 |
| Figure 4.15 | The effect of the electric field between the sample and the electron energy analyzer on the effective acceptance angle of the analyzer. | 114 |
| Figure 4.16 | The effect of bias on energy distributions at low photon energy (1.64 eV). L valley electrons are observed even though the excitation energy is too low. | 115 |
| Figure 4.17 | (a) EDCs of 2.05 eV photon energy at different times after the completion of activation (20 minutes and 5 hours) (b) EDCs of 2.46 eV photon energy at different time after the completion of activation (20 minutes and 5 hours) | 116 |

List of Tables

Chapter 1 Introduction

| | | |
|------------------|-------------------------------------|-----------|
| Table 1.1 | Selected physical properties of InP | 17 |
|------------------|-------------------------------------|-----------|

Chapter 2 Activation layer of InP photocathodes

| | | |
|------------------|--|-----------|
| Table 2.1 | Binding energies of multiplet peaks of cesium oxides in the valence band | |
| | Spectra | 38 |

1. INTRODUCTION

1.1 Introduction

The technology and applications of devices constructed of InP-based materials have made remarkable progress recently. InP is used in many electronic and optoelectronic devices, due to its various advantages, such as band gap energy suitable for light emitters and receivers in the long wavelength region, and the extremely high saturation velocity of electrons for active channels in high-power and high-speed devices. In addition to these advantages, InP has gained emerging importance as a negative electron affinity (NEA) transferred electron photocathode (TEP) material in imaging technologies, due to its lattice matching with small and variable band-gap materials, such as $\text{Ga}_x\text{In}_{1-x}\text{As}_y\text{P}_{1-y}$, which are utilized as sensitive detectors at wavelengths from 0.92 μm to 1.65 μm at 300 K [1]. InP provides itself as a substrate to grow these small band-gap materials, and also serves as an efficient electron emitter with a low work function barrier at the surface, in this TEP application [2]. The high quantum efficiency (QE) of these TE photocathodes is due to a surface phenomenon, specifically a negative electron affinity (NEA) state [3]. This NEA state is realized by depositing alkali metals (Cs) and gas (mainly O_2 , sometimes NF_3) on the surface of p-type semiconductors. However, the exact chemical composition or arrangement of atoms in the Cs oxide layer and at its interface with InP substrate is not well understood.

Achieving efficient emitting surfaces of InP-based long-wavelength TE photocathodes is critical to the overall performance of the photocathodes, so there has been increasing interest in TE photoemissions, including InP field-assisted TE

photoemission, InGaAs ternary alloy/InP TE photoemission, and InGaAsP quaternary alloy/InP TE photoemission. The foci of these studies, however, have been either on alloy growth and characterization [4] or on yield characterization in the long wavelength region [5 – 10]. The emitting surface (Cs oxide layer and its interface with InP) has been elusive and less studied. Even though some studies have focused on a Cs oxide activation layer and the reason for NEA states, the thickness estimation of the Cs oxide layer generally is too large [11 – 14] or the chemistry of Cs oxides is not satisfactorily explained [15 – 17].

In the current work, we tried to understand the chemistry of the Cs oxide layer and apply this knowledge to the performance of photocathodes, thereby helping to optimize the development of new photocathode devices with improved performance. This study led to the discovery of molecular oxygen species (O_2^{2-} , O_2^-) incorporated in the thin activation layer, and also proposed a model of lateral distributions of Cs peroxides (Cs_2O_2) and Cs superoxides (CsO_2). This model of Cs oxide distribution in the layer further helped to understand the QE decay of photocathodes, and explained the chemical changes that occur at the surface and in the substrate during the decay of QE.

After characterizing the surface of InP photocathodes, this work studies the energy distribution and angular distribution of photoelectrons from InP photocathodes. These properties have practical importance, in terms of the brightness and directionality of photocathodes. We studied the energy distribution and angular distribution of InP photoelectrons, which, in turn, affect the sensitivity and resolution of photocathodes, under near band-gap excitations, with the aid of energy distribution curve (EDC)

measurements, which distinguished two distinct kinds of photoelectrons and their angular distributions.

1.2 NEA Photocathodes: Applications in Night Vision, and Principles

1.2.1 NEA Photocathodes and Traditional Night Vision Devices

NEA photocathodes are photocathodes in which there is no potential barrier between the bulk conduction band minimum and the vacuum level at the surface, as illustrated in Figure 1.1. The deposition of Cs or Cs/O on semiconductor surfaces and the downward band bending by heavy p-type bulk dopings are necessary to achieve negative electron affinity. The development of NEA photocathodes in the 1970s led to great improvements in applicability and efficiency, in two ways. First, the QE of NEA photocathodes is significantly greater than that of old photocathodes. Second, and more importantly, for the first time, scientific engineering plays a key role in developing new photocathodes. Knowledge of the physics involved in photoemission events and of the technology of semiconductor materials are two main reservoirs to serve the development of NEA photocathodes [18].

III-V NEA photocathodes are employed in the latest night vision technologies, and they are much brighter than previous technologies. Night vision devices gather existing ambient light (starlight, moonlight or infra-red light) through a front lens. This light goes into a photocathode tube, which changes the photons to electrons, as shown in Figure 1.2. The electrons then are amplified to a much greater number through both an electrical and chemical process. Until recently, these electrons passed through a thin disk (a micro channel plate) that is about the size of a quarter and contains over 10 million

channels. As the electrons travel through and strike the walls of the channels, thousands more electrons are released. The electrons then are hurled against a phosphorus screen that changes the amplified electrons back into visible light that you can see through the eyepiece. The resulting image now is a clear, green-hued, amplified re-creation of the scene you initially had been observing.

1.2.2 Next generation night vision devices

The main requirements of an image intensifier for night vision devices are 1) small size; 2) light weight; 3) low power requirements; and 4) low cost. The satisfactory fulfillment of these needs enables image intensifier goggles to serve as head-worn, individual soldier applications. Further development of an image intensifier focuses on longer wavelength spectral responses, higher sensitivity, larger fields of view, and increased resolution. One of the next generation configurations for imaging devices is the electron-bombarded charge-coupled device (EBCCD). EBCCD eliminates the micro-channel plate (MCP), phosphorus screen, and fiber optics; as a result, both improved image quality and increased sensitivity can be obtained in a smaller camera. A transferred electron photocathode (TEP) is coupled directly with a CCD chip in an EBCCD configuration, as shown in Figure 1.3. This is applied to actively illuminated, eye-safe laser imaging, leading to 20% or higher quantum efficiency over the spectral range, which is between 0.95 and 1.7 μm [19]. The approach of using the transferred electron effect in order to extend the threshold of photocathodes into near infra-red lights was conceived and patented by Bell in the 1970s [20]. For InP-based transferred electron photocathode, an internal electric field is applied, so that the conduction band of InP can

be aligned with light-absorbing materials. This electric field further promotes the conduction band electrons to upper conduction valleys. An ideal application of the TE-EBCCD sensor is within a range-gated, laser-illuminated, two-dimensional imaging system [21]. The significant feature of this embodied concept is the wavelength of operation. The TE photocathode enables the operation of practical range-gated systems in the 1.5 – 1.6 μm band, where the eye's tolerance to high-intensity illumination is substantially greater than at longer wavelengths, where traditional photocathodes have sensitivity.

InP and InP-based alloys have suitable band-gaps for shorter- wavelength TE photocathodes. One must review basic photoemission theory to understand how photocathodes work and how to balance engineering tradeoffs.

1.2.3 Spicer's three-step model

The Spicer three-step model is the first comprehensive model explaining the mechanism behind photoemission within a solid. Until 1958, photoemission was considered to be a surface phenomenon. Optical absorption also was believed to be surface-related, and electron transport through a material was not considered [22]. In 1958, Spicer developed a model or theory [23], often called the *three-step model*, which, for the first time, treated photoemission as a bulk process, as described in Figure 1.1. This model explains the photoemission process quantitatively, in terms of bulk optical coefficients, electron scattering lengths, and surface properties, such as the vacuum level at the surface of a solid. The simplicity of the three-step model is that it quantifies the overall probability of photoemissions as a product of the probabilities of each step.

Let us consider a semi-infinite slab of material. Photoemission arises from an infinitesimal slice of thickness dx located at depth x within the slab, as shown in Figure 1.4. The probability of the first step generating photo-excited carriers is expressed by

$$dP_{\alpha} = \alpha(h\nu) \exp(-\alpha(h\nu)x) dx.$$

Since $\alpha(h\nu)$ is the sum of $\alpha_{pe}(h\nu)$ and $\alpha_n(h\nu)$ (α_{pe} : photo-excitation above the vacuum level; α_n : photo-excitation below the vacuum level), and only α_{pe} contributes to the photoelectrons escaping out of a solid, the actual first-step probability is expressed by

$$dP'_{\alpha} = \alpha_{pe}(h\nu) \exp(-\alpha(h\nu)x) dx.$$

The second step requires calculating the probability of electrons reaching the surface with sufficient energy to escape, and is described by

$$P_T = A(h\nu) \exp\left(-\frac{x}{L(h\nu)}\right).$$

....where $L(h\nu)$ is the inelastic mean free path of electrons, and $A(h\nu)$ is a function representing the dominant scattering mechanism. The $P_E(h\nu)$ for the third step is the probability of escape among those electrons that reach the surface with sufficient energy [22].

The production of these three probabilities is the total probability dP :

$$dP = dP'_\alpha \bullet P_T \bullet P_E = A(h\nu)\alpha_{PE}(h\nu)P_E(h\nu)\exp(-(\alpha(h\nu) + \frac{1}{L(h\nu)})x)dx.$$

And the integration, from 0 to infinity, leads to

$$P = A(h\nu)P_E(h\nu)\left(\frac{\alpha_{PE}(h\nu)/\alpha(h\nu)}{1 + L_\alpha(h\nu)/L(h\nu)}\right), \text{ where the absorption length } L_\alpha(h\nu) \text{ is } 1/\alpha(h\nu).$$

The total probability, P , is maximized when the escape depth $L(h\nu)$ is much larger than the absorption length $L_\alpha(h\nu)$, and also when $\alpha_{PE}(h\nu)/\alpha(h\nu)$ is close to unity.

$\alpha_{PE}(h\nu)/\alpha(h\nu)$ is the ratio of the number of photoelectrons excited above the energy of the vacuum level to the total number of photoelectrons, and this can be increased by lowering the vacuum level and having low electron affinity. For a semiconductor, which has relatively low electron affinity, electron-phonon scattering is the major scattering mechanism, which leads to a large escape depth, since the energy lost by electron-phonon scatterings is very small, compared to the energy lost by electron-electron scatterings.

The escape depth can be made larger by having a good quality crystal.

1.3 InP Material Properties

InP has a zincblende crystal structure, as shown in Figure 1.5. The bonding between the In and P atoms is known as an sp^3 – hybridized bond. In: $(5s)^2(5p)^1$ and P: $(3s)^2(3p)^3$ are hybridized to form four bonds in InP. In Table 1.1, the main physical properties of InP are summarized [24]. Figure 1.6 illustrates the lattice constants and

band-gaps of various compound semiconductors, and shows that InP is lattice-matched with InGaAs alloys and InGaAsP alloys. This is a major reason that InP is an indispensable substrate material for lasers and photodetectors in fiber communications, in the wavelength of 1.3 μm and 1.55 μm [25], and for high frequency electronic devices like HEMTs and HBTs [26, 27]. The band gap of InP is 1.35 eV. With the same lattice constant, the band gap of quaternary InGaAsP can be changed from 1.35 eV to 0.74 eV (0.9 μm \sim 1.7 μm). By changing the composition of InGaAsP, the alloy appropriate to the fiber communication wavelength can be obtained with the same lattice constant as the InP substrate [28].

1.4 Techniques

1.4.1 Photoemission Spectroscopy (PES)

The physics behind PES is Einstein's description of the photoelectric effect. The material to be analyzed is exposed to a monochromatic beam of X-rays or ultraviolet light, which induces the photo-ionization of sample atoms. In PES, these photoelectrons are collected and their kinetic energy is determined, resulting in a recorded spectrum of electron intensity, as a function of the measured energy. Using a modified version of Einstein's relation $E_k = h\nu - E_B - \phi_a$, where ϕ_a is the work function of an electron energy analyzer, it now is possible to calculate the binding energy for a certain intensity peak, since the incoming light has a known frequency. The binding energy of any given energy level is material dependent. Moreover, it is affected by the precise chemical state and bonding of the material. By comparing the observed spectrum with tables of known

binding energies for different elements, the chemical contents of the surface can be determined.

Commercial *X-ray Photoemission Spectroscopy* (XPS) instruments include an X-ray source (e.g. aluminum K_{α} radiation). This entire instrument is kept in an ultra-high vacuum (UHV) environment. Usually, the photoelectrons are collected using an electrostatic lens system, though some magnetic lens designs are available. An electrostatic energy analyzer determines the kinetic energy of the collected photoelectrons.

Synchrotron radiation is the best source of photons in the spectral range of interest for photoemission spectroscopy. Synchrotron radiation is the energy-tunable source of vacuum ultraviolet and soft x-ray photons [29]. The characteristics of synchrotron radiation, like high intensity, make some photoemission techniques possible.

The atomic binding energy of an element is not the same in different materials, because the electron density around the atoms is different, due to bonding in the compound. If the electron density around the atom is low, the nucleus tends to attract electrons more tightly, resulting in higher binding energy. In most cases, the chemical states of the element play the most important role; thus, differences in binding energies are called *chemical shift*. Chemical shifts can be determined experimentally. The values of many chemical shifts can be found in [30] and in the references therein.

It is necessary to fit PES spectra with reasonable physics parameters to decompose a peak into individual components, using parameters like Gaussian width, Lorentzian width, spin-orbit splitting, branching ratio, etc. The theoretical line shape for fitting is a Gaussian function that has been convoluted with a Lorentzian function, which

is the so-called *Voigt function*. A Lorentzian shape represents the lifetime of the core hole, while a Gaussian shape contains information regarding the broadness caused by the beam or instruments. Figure 1.7 shows In4d spectra fitted with a branching ratio of 0.667, and a spin orbit splitting of 0.86. The Lorentzian width is fixed at 0.1, whereas the Gaussian width varies. An oxide peak has a larger Gaussian width than a bulk peak, whereas a Cs-induced peak has the same Gaussian width as that of a bulk peak in our peak fitting. Peak positions are normally fixed, as long as photon energy remains the same and there is no band-bending.

1.4.2 Synchrotron Radiation

When charged particles, in particular electrons or positrons, are forced to move in a circular orbit, photons are emitted. At relativistic velocities (when the particles are moving at close to the speed of light), these photons are emitted in a narrow cone in the forward direction, tangential to the orbit. In a high-energy electron or positron storage ring, these photons are emitted with energies ranging from infrared to energetic (short wavelength) X-rays. This radiation is called *synchrotron radiation*. Synchrotron radiation has a number of unique properties: high-level brightness (synchrotron radiation is extremely intense, hundreds or thousands of times stronger than conventional X-ray tubes, and highly collimated), a wide energy spectrum (synchrotron radiation is emitted with a wide range of energies, allowing a large energy range beam to be produced), high polarization, and very short pulses (typically less than one nano-second).

In our study, photon energies in the 20 to 700 eV range are used in order to obtain high energy resolution and high surface sensitivity for the In4d, P2p, O1s core levels. The

beam lines where we conducted this research are SSRL beam line 8-1 and SSRL beam line 10-1. At 8-1, the energy range is about 20 – 180 eV, and 10-1 offers an energy range from 200 – 1300 eV.

1.4.3 Near Edge X-ray Absorption Fine Structure (NEXAFS)

NEXAFS is a powerful surface science tool, using synchrotron radiation, which can be used to study the orientation and bonding of molecular adsorbates on a surface [31 – 33]. NEXAFS is a relatively new technique, and currently is very important and useful in surface science, especially in studies on molecular adsorbates, such as oxygen molecules adsorbed on different substrates [34 – 38].

When X-ray radiation penetrates matter of known thickness, d , its intensity is attenuated according to the Lambert-Beer Law [39]:

$$I(d) = I_o \exp(-\mu\rho d)$$

...where I_o is the incident flux, ρ is the density of the material, and μ is the mass-absorption coefficient, which depends upon the energy of the incoming x-rays. An abrupt increase in the absorption coefficient is an *absorption edge*, which corresponds to the binding edge of a core level. The region from the absorption edge to approximately 40 eV above the edge, often called the *x-ray absorption near edge structure* (XANES) or the *near edge x-ray absorption fine structure* (NEXAFS), is related to the unoccupied density of states which reflect the electronic structure of the material. In addition, the spatial location of neighboring atoms is represented at energies 100 to 1000 eV above the edge,

which is known as the *extended x-ray absorption fine structure* (EXAFS). At energies from 10 to 40 eV above the binding energy, spectral features become apparent, due to multiple scattering resonances. At these energies, the mean free path of the ejected photoelectron is only a few angstroms, and elastic scattering with neighboring atoms results in interference effects called *multiple scattering resonances*. These resonances result in specific spectral features, which are dependent upon the spatial and geometrical arrangement of neighboring atoms [40].

1.4.4 Instruments

The vacuum system is shown schematically in Figure 1.8. A PHI model 10-360 hemispheric capacitor electron energy analyzer with the Omni Focus V small area lens is mounted on the chamber with an angle of $54^{\circ}44'$ (magic angle) with respect to the incoming photon beam direction. This analyzer has a multi-channel detector, and a model 80-365 AHR high-resolution digital SCA controller. The working distance for this analyzer is 19.1 mm. A Cs-doser and a temperature probe using an Al-Cr thermocouple also are available.

The sample manipulator is manufactured by *Thermionics*, under the project number A109H6NW. The manipulator is mounted on a differentially-pumped rotary seal. The sample can be heated up to 1100°C . This sample mounting system is relatively large compared to the working distance of the analyzer, so care must be taken to prevent it from colliding with other equipment inside the chamber, such as the input lens of the analyzer. A *Thermionics STLC-1 Locking Clip Turn-To Lock* sample transfer system is used. In normal operation, the sample is put on the sample transfer fork in the load lock,

then the load lock is pumped by a turbo pump. When the pressure is below 5×10^{-6} torr, the sample is transferred into the chamber for analysis.

1.5 Overview of the work

The purpose of this work is to examine the activation, the decay mechanism, and the energy and angular distribution of Cs/O-activated InP(100) photocathodes. Experiments predominantly were done at the *Stanford Synchrotron Radiation Laboratory* (SSRL). The activated surface has an angular dependence of valence band and O1s core level photoemission spectra, which leads us to suggest that the surface model presents the lateral distribution of Cs peroxides and Cs superoxides. The decay of QE is related to the conversion of Cs peroxides to Cs superoxides, and to the subsequent oxidation of a substrate. The recesiation technique is introduced to simulate sealed commercial tubes in our open UHV system. The energy and angular distributions of photoelectrons from InP(100) photocathodes were studied by means of energy distribution curve (EDC) measurements. In this work, we investigated the activated InP photocathodes with the aid of surface characterization techniques, such as photoemission spectroscopy (PES).

The outline of this work is as follows. *Chapter 1* provides the motivation behind this work and the basic concepts of NEA photocathodes and night vision technologies, and also introduces the experimental techniques and instruments and provides an overview of this work. *Chapter 2* focuses particularly on the chemistry of the Cs/O activation layer on InP. The molecular oxygen species in the layer is introduced, and a lateral distribution model for those oxide species based upon our angle-dependent photoemission (ADPES) is proposed. The agreeable match between experimental data

and calculated values based upon the model also is presented. *Chapter 3* discusses the decay of quantum efficiency and its mechanism, and suggests a way to stabilize the activated surface. The decay of QE initially is accompanied by the transformation of peroxides to superoxides, which is followed by the oxidation of a substrate. The recesiation technique, which is a repetitive dose of cesium during decay, keeps the QE at a certain level. In *Chapter 4*, we present experimental results and discuss the energy and angular distribution of photoelectrons from the InP(100) photocathode, by means of *Energy Distribution Curve* (EDC) measurements, which also can be called *Near Band-Gap Photoemission*. We found that there are two kinds of photoelectrons contributing to the electron distribution out of InP photocathodes during near-bandgap excitation. One group of electrons is thermalized in a Γ conduction band valley, and the other electrons transfer to a higher conduction band valley by inter-valley scatterings with polar optical phonons. These electrons have different angular distributions, due to their different effective masses. This electron distribution changes, because of the vacuum level movement that occurs as the decay proceeds. *Chapter 5* concludes the discussion and suggests future work.

1.6 References

- ¹ O. Wada, H. Hasegawa, ed., *InP-Based Materials and Devices*, John Wiley & Sons Inc. (1999)
- ² T. P. Pearsall, ed., *GaInAsP Alloy Semiconductors*, Wiley, Chichester, West Sussex, England (1982)
- ³ R. L. Bell, *Negative Electron Affinity Devices*, Clarendon, Oxford (1973)
- ⁴ R. Sankaran et al, J. Vac. Sci. Technol. **13**, 932 (1976)
- ⁵ J. S. Escher, IEEE Trans. Elec. Dev. **27**, 1244 (1980)
- ⁶ R. L. Bell et al, Appl. Phys. Lett. **19**, 513 (1971)
- ⁷ J. S. Escher et al, J. Appl. Phys. **49**, 2591 (1978)

- ⁸ R. L. Bell, L. W. James, R. L. Moon, Appl. Phys. Lett. **25**, 645 (1974)
- ⁹ J. S. Escher, R. Sankaran, Appl. Phys. Lett. **29**, 87 (1976)
- ¹⁰ J. S. Escher et al, CRC Crit. Rev. Solid State Sci. **5**, 577 (1975)
- ¹¹ R. L. Bell, W. E. Spicer, Proc. IEEE **58**, 1788 (1970)
- ¹² H. Sonnenberg, Appl. Phys. Lett, **14**, 289 (1969)
- ¹³ A. F. Milton, A. D. Baer, J. Appl. Phys. **42**, 5059 (1971)
- ¹⁴ L. W. James, J. J. Uebbing, Appl. Phys. Lett. **16**, 370 (1970)
- ¹⁵ A. H. Sommer, H. H. Whitaker, B. F. Williams, Appl. Phys. Lett. **17**, 273 (1970)
- ¹⁶ J. M. Chen, Surf. Sci. **25**, 457 (1971)
- ¹⁷ D. G. Fisher et al, J. Appl. Phys. **43**, 3815 (1972)
- ¹⁸ W. E. Spicer, Appl. Phys. **12**, 115 (1977)
- ¹⁹ X. Xu, J. Guo, SPIE Vol. **4919**, 536 (2002)
- ²⁰ R. L. Bell, Long-Wavelength Photoemission Cathode, Patent Number 3,958,143
- ²¹ K. Costello, V. Aebi, G. Davis, R. La Rue, R. Weiss, SPIE Vol. **2550**, 177 (1995)
- ²² W. E. Spicer, A. Herrera-Gomez, SPIE Vol. **2022**, 18 (1993)
- ²³ W. E. Spicer, Phys. Rev. **112**, 114 (1958)
- ²⁴ M. O. Manasresh, ed., *InP and related compounds: materials, applications and devices*, Gordon & Breach, Amsterdam (2000)
- ²⁵ K. Onabe, Jpn. J. Appl. Phys. **21**, 791 (1982)
- ²⁶ Papers in the Proc. 8th Int. Conf. on InP and Related Materials, Schwabisch Gmund (1996)
- ²⁷ Papers in the Proc. 9th Int. Conf. on InP and Related Materials, Hyaniss (1997)
- ²⁸ W. J. Turner, W. E. Reese, G. D. Pettit, Phys. Rev. **136**, A1467 (1964)
- ²⁹ G. Margaritondo, *Introduction to Synchrotron Radiation*, Oxford, (1988)
- ³⁰ Handbook of X-ray photoelectron spectroscopy, Perkin-Elmer Corporation, Physical Electronics Divisions, Oct., (1992)
- ³¹ J. Stohr, *NEXAFS spectroscopy*, New York, Springer (1992)
- ³² J. Stohr, D. A. Outka, Phys. Rev. B, **36**, 7891 (1987)
- ³³ J. Stohr, R. Jaeger, Phys. Rev. B, **26**, 4111 (1982)
- ³⁴ J. Stohr, J. L. Gland, W. Eberhardt, D. Outka, R. J. Madix, F. Sette, R. J. Koestner, U. Doebler, Phys. Rev. Lett., **51**, 2414 (1983)
- ³⁵ M. W. Ruckman, J. Chen, S. L. Qiu, P. Kuiper, M. Strongin, Phys. Rev. Lett., **67**, 2533 (1991)
- ³⁶ D. Norman, J. Stohr, R. Jaeger, P. J. Durham, J. B. Perdrey, Phys. Rev. Lett., **51**, 2052 (1983)
- ³⁷ U. Hofer, A. Puswchmann, D. Coulman, E. Umbach, Surf. Sci., **211/212**, 948 (1989)

³⁸ W. Worth, J. Stohr, P. Feulner, X. Pan, K. R. Bauchspiess, Y. Baba, E. Hudel, G. Rocker, D. Menzel, Phys. Rev. Lett., **65**, 2426 (1990)

³⁹ E. Gullickson, X-ray Data Booklet edited by A. Thompson and D. Vaughan, Lawrence Berkeley Labs, Berkeley, p. 1-38 (2001)

⁴⁰ M. Belli, A. Scafati, A. Bianconi, S. Mobilio, L. Palladino, A. Reale, E. Burattini, Solid State Commun., **35**, 355 (1980)

| | |
|--|---|
| Crystal Structure | Zinc Blend |
| Lattice constant | 5.869 Å |
| Density | 4.787 g/cm ³ |
| Melting point | 1335 K |
| Vapor pressure at melting point | 27.5 atm |
| Linear expansion coefficient | 4.5 x 10 ⁻⁶ /deg |
| Thermal conductivity | 0.70 W/cm K |
| Dielectric constant | 12.5 |
| Band gap at room temperature (R. T.) | 1.35 eV |
| Optical transition type | Direct |
| Intrinsic carrier concentration at R. T. | 2.0 x 10 ⁻⁷ cm ⁻³ |
| Electron mobility at R. T. | 4,500 cm ² /V s |
| Hole mobility at R. T. | 150 cm ² /V s |

Table 1.1 Selected physical properties of InP

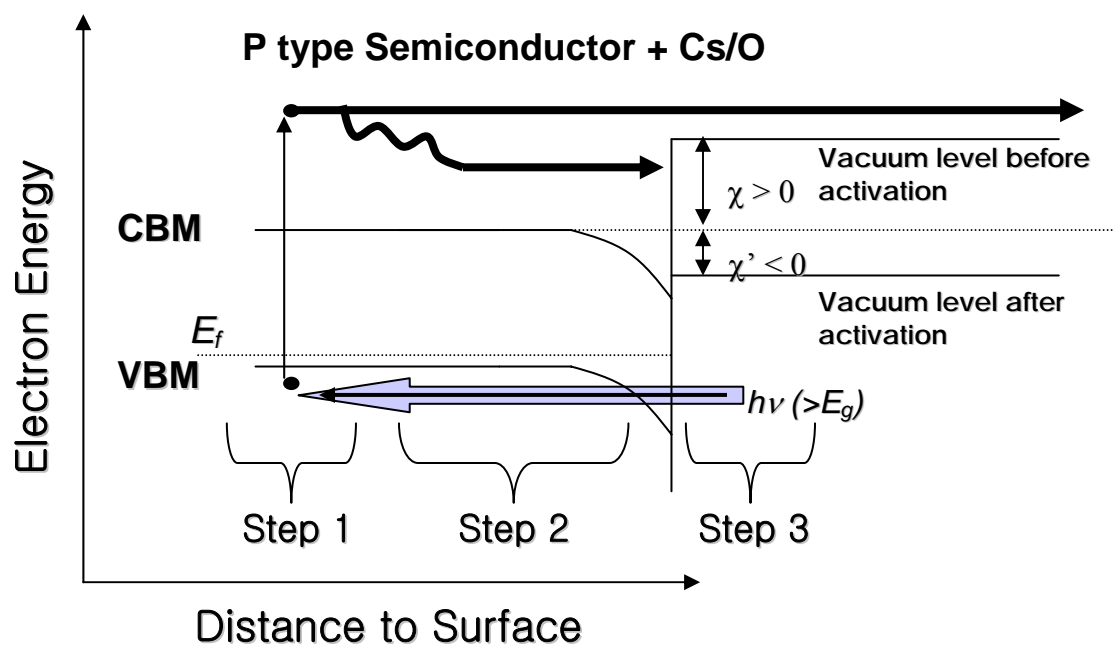


Figure 1.1 The process of photoemission from negative electron affinity photocathode: step 1 is the excitation of electrons, step 2 is the transport of electrons to the surface, and step 3 is the escape of electrons into the vacuum.

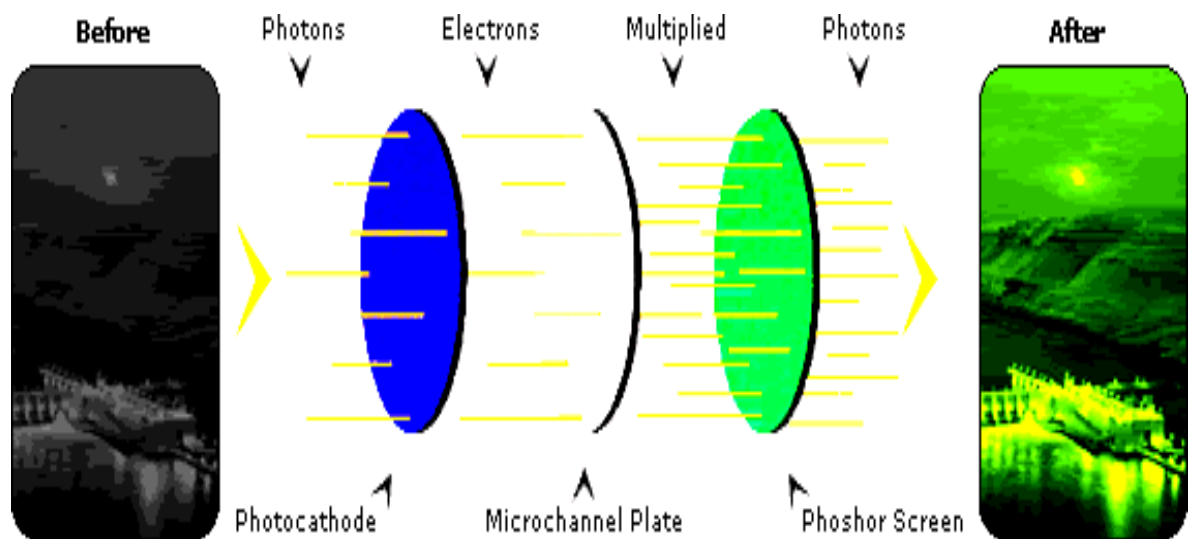


Figure 1.2 The schematic diagram of the image-intensifying process in a night vision tube

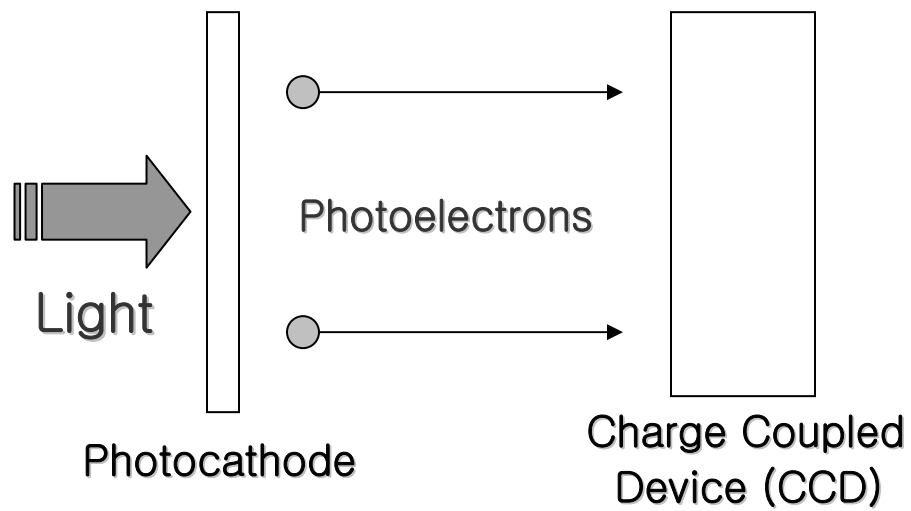


Figure 1.3 Electron Bombarded CCD (EBCCD) diagram is presented.

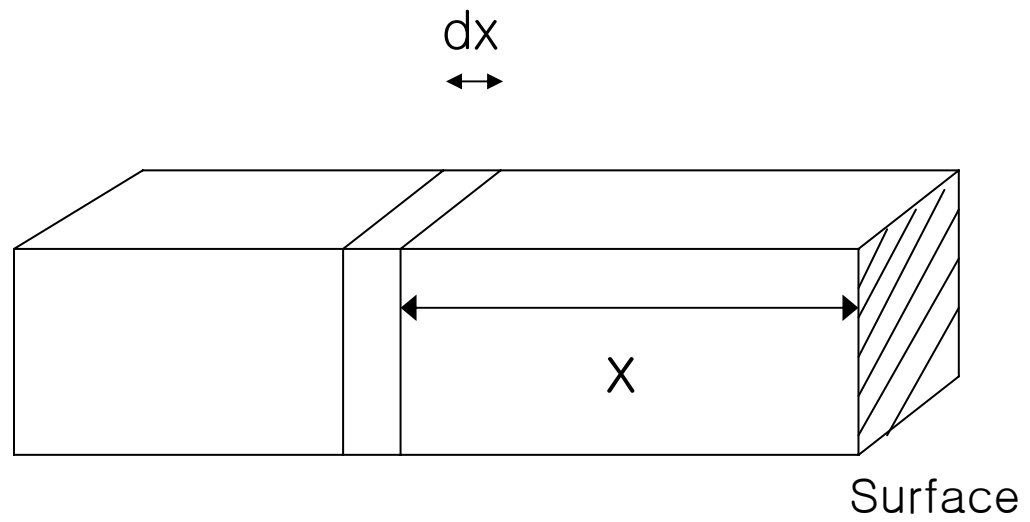


Figure 1.4 The absorption of photon in the semi-infinite slab is described.

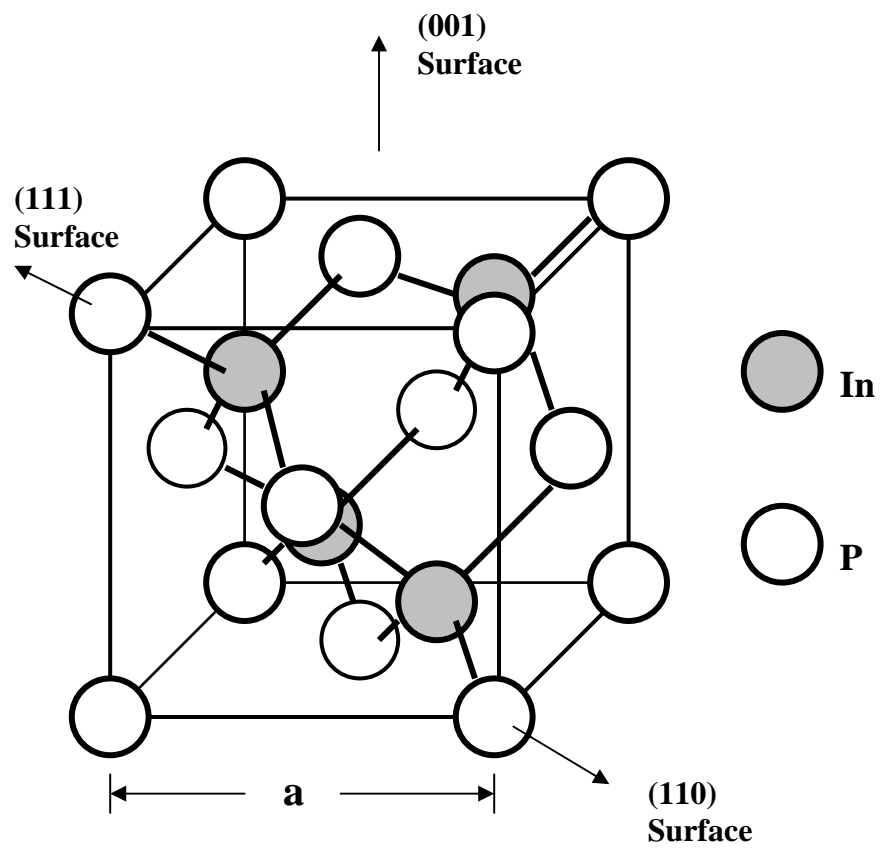


Figure 1.5 Zincblende structure. a is a lattice constant.

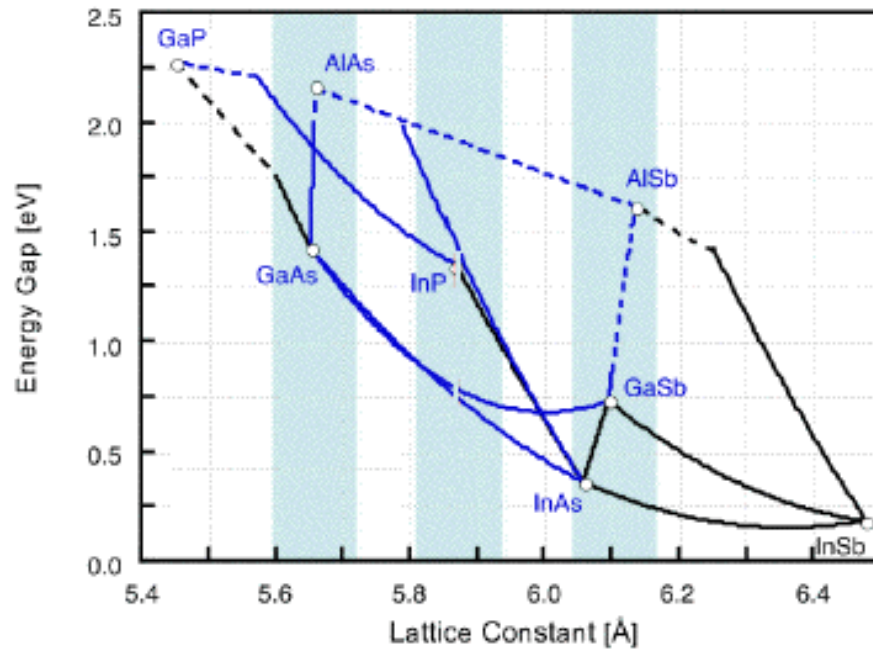


Figure 1.6 Lattice constants and band-gaps of various III-V compound semiconductors

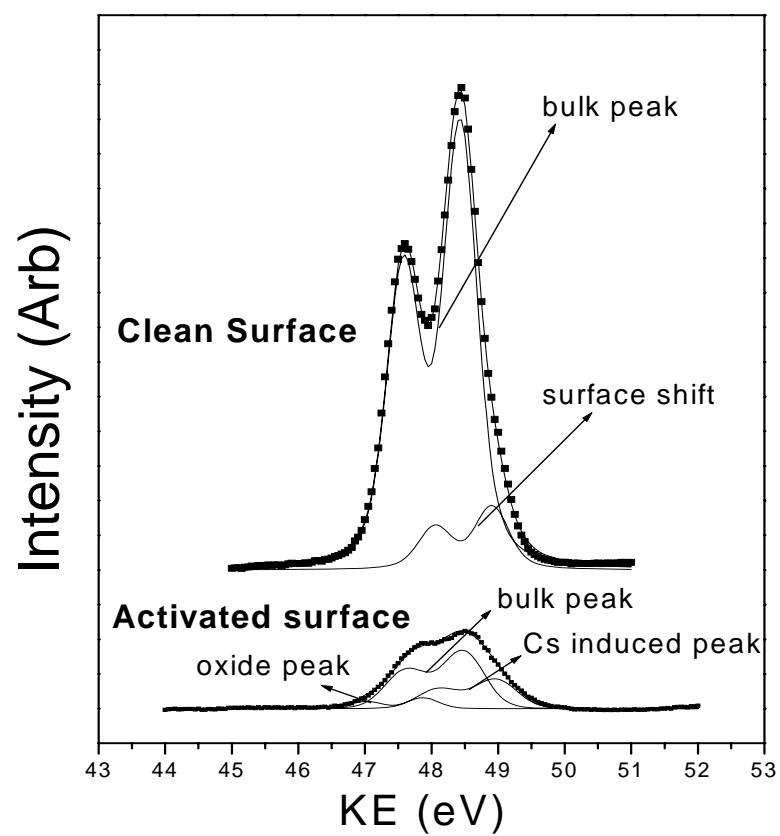


Figure 1.7 In4d fitting of a clean surface and an activated surface

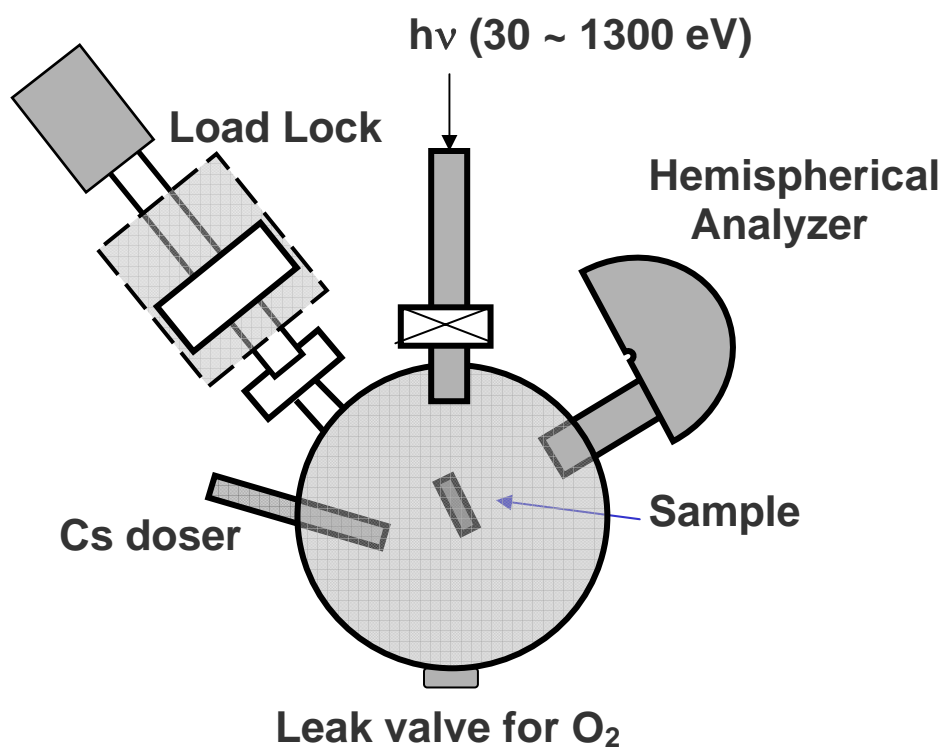


Figure 1.8 Schematic diagram of the PES system viewed from above. A hemispherical analyzer is mounted at the magic angle with respect to the incoming photon beam. Thermocouple and Cs doser are also available.

2. ACTIVATION LAYER OF INP(100) PHOTOCATHODES

2.1 Introduction

A negative electron affinity (NEA) state is achieved when the vacuum level becomes lower than the bulk conduction band minimum. This NEA state is necessary to obtain a high quantum yield in the application of photocathodes. To achieve an NEA state, the photocathode is activated by co-depositing Cs and O on III-V semiconductor surfaces [1]. Among III-V semiconductors, GaAs has been a primary material among researchers and in industrial applications. However, InP recently has been recognized as an important photocathode material, since its lattice matches $\text{In}_{1-x}\text{As}_x\text{Ga}_y\text{P}_{1-y}$ band-gap engineering materials, and it has an efficient emitting surface [2].

Three different models for the Cs/O activation layer of an NEA III-V photocathode have been proposed. One is the *dipole model*, which explains how the vacuum level is lowered via the formation of electrical dipoles between a Cs/O layer and a semiconductor substrate [3 - 6]. The other two models are the *heterojunction model* [7 - 9] and the *cluster model* [10]. The heterojunction model contains the incorrect assumption of a thick Cs oxide layer. None of the three models successfully explains the chemistry that takes place in the Cs/O activation layer. Two major questions that remain unanswered are: 1) what is the chemical composition of the Cs/O layer; and 2) what is the atomic arrangement of this layer?

In this study, we investigated the activation layer of Cs/O on an InP substrate using synchrotron radiation photoemission spectroscopy (SR-PES). We were able to

distinguish two different cesium oxides, namely Cs peroxides and Cs superoxides. Using angle-dependent photoemission spectroscopy (ADPES), we discovered that oxygen in each cesium oxide is located differently in the activation layer and proposed a structural model for each oxide species.

2.2 Experiment

The samples used in this study were Zn doped p-type InP(100) crystals provided by *Wafer Technology, UK* and *American Crystal Technology*, with doping concentrations of $5 \times 10^{17} \text{ cm}^{-3}$ and $2.3 \times 10^{18} \text{ cm}^{-3}$, respectively, and a wafer thickness of 0.35 mm. To clean the InP(100) surface, we used the two-step cleaning process described in [11]. All the chemical cleaning was performed in a glove bag that had an Ar-purged environment. Cesium was evaporated from a SAES Cs getter chromate source. This Cs getter was carefully out-gassed before use, as described in reference [12]. Molecular oxygen was leaked through a leak valve, and the oxygen pressure was maintained below $1 \text{E-}8$ torr. An ion gauge was not used during activation, because ionized oxygen contributes to the oxidation of III-V semiconductors, an effect not desired in this study [13]. During the co-deposition of Cs and O, the temperature of the sample was held at room temperature. A He-Ne laser (632.8nm) was used to generate photoelectrons, so that the activation process could be monitored. When the Cs evaporator was turned on, the photoelectron emission current increased until it reached a maximum at 0.5 ML of Cs, after which the photocurrent dropped. At that point, oxygen intentionally was leaked in, causing the photocurrent to increase again, and subsequently turned off when the photocurrent began

to decrease again. This process of modulating the amount of oxygen was repeated, each time achieving a higher QE than before, until no higher QE could be achieved. However, if the oxygen flux is well matched to the Cs flux, modulation of oxygen is not needed, as shown in Figure 2.1. For each measurement of the photocurrent, the QE was calculated from the power of the He-Ne laser measured by a photodiode.

We changed the emission angle by rotating the sample with respect to the analyzer, so as to change the surface sensitivity in ADPES. Figure 2.2 shows two extreme configurations. In the configuration with a 90° emission angle, the probing depth was maximized at a given photon energy (relatively bulk-sensitive), while the probing depth became smaller in the configuration with a 30° emission angle (relatively surface-sensitive).

2.3 Results & Discussion

2.3.1 Angle-Dependent Photoemission Spectroscopy (ADPES) Measurements

It is known that Cs forms several different kinds of oxide when it reacts with oxygen. CsO_2 , Cs_2O_2 and Cs_2O are produced when the amount of oxygen is comparable to the amount of Cs. Sub-oxides, like Cs_{11}O_3 , Cs_7O , and Cs_3O are formed at low temperatures, when Cs reacts with a small amount of oxygen. Previous ultra-violet photoemission spectroscopy (UPS) studies have investigated the formation of these Cs oxides, by introducing oxygen to bulk Cs [14 - 21]. Photoemission studies of oxygen species in the activation layer also have been undertaken on other III-V photocathodes, such as GaN [22]. In this study, the VB spectrum observed after activation is shown in Figure 2.3, in which we detected three main peaks. We believe peak A (with kinetic energy of 62.5 eV) is related to peroxide O_2^{2-} , while peaks B (with kinetic energy of 60.7

eV) and C (with kinetic energy of 56.9 eV) are related to superoxide O_2^- . It is well known that Cs forms Cs superoxides and Cs peroxides when enough oxygen is present; nevertheless, the real peak assignment requires us to analyze valence band spectra and compare them with the literature. The binding energies of peaks A, B and C in the valence band spectra are agreeable with the binding energies (BEs) of oxygen species O_2^{2-} and O_2^- in other UPS studies of bulk Cs oxidation, as shown in Table 2.1. Small deviations have been reported in different sources in the literature; but, generally speaking, it has been found that Cs peroxide (Cs_2O_2) have three features, with kinetic energies of about 3.3 eV, 6.1 eV and 7.5 eV, which correspond to π_{2p}^* , π_{2p} and σ_{2p} molecular orbital for O_2^{2-} . Cs superoxide (CsO_2) have four features, with binding energies of 4.7 eV, 5.8 eV, 6.2 eV and 8.5 eV, the first two of which are from the π_{2p}^* orbital of O_2^- ; the third and fourth are from π_{2p} and σ_{2p} , respectively [2].

The Fermi level measured using an Au sample is at 65.5 eV photon energy. Using this Fermi level as the reference, the binding energies of peaks A, B and C can be measured as 3.0 eV (peak A), 4.8 eV (peak B) and 8.6 eV (peak C). Other features cannot be resolved satisfactorily. Notice that, in our assignment, the superoxide peaks for B and C are noted to have an energy difference by Su [14] and Woratschek [15], while peak separation between B and C matches Su's findings fairly well. This energy difference may be due to the fact that we study a thin Cs/O layers instead of the bulk Cs oxide studied by Su and Woratschek. This energy shift for Cs superoxide peaks also exists in Su's [14] and Woratschek's work [15] and was attributed to the open shell nature of the $O_2^- \pi_{2p}^*$ orbital, which enables the environment to have a stronger effect on O_2^- energy levels [2].

The O1s spectrum is shown in Figure 2.4, and two types of oxygen species are clearly seen. Peak A, with kinetic energy of 103.3 eV, is assigned as oxygen in peroxides, and peak B, with kinetic energy of 100.8 eV, is assigned as oxygen in superoxides, since Cs peroxides are richer in electrons than Cs superoxides. Consequently, oxygen in Cs peroxides has a lower binding energy (higher kinetic energy) than oxygen in Cs superoxides. The angular dependence of oxygen intensities in cesium oxides is shown in O1s core level spectra. When an emission angle becomes larger, the intensity of peak A (Cs peroxide) becomes relatively large, while the intensity of peak B (Cs superoxide) becomes relatively small. This result provides us with evidence that cesium peroxides are located deeper in the Cs/O activation layer, while cesium superoxides are nearer to the surface, because photoemission with the 90° emission angle is relatively bulk-sensitive, and photoemission with the 30° emission angle is relatively surface-sensitive. The three main peaks in the valence band spectra (Figure 2.3) have an angular dependence, similar to the peaks of O1s core level spectra. Immediately after activation (Figure 2.3(a)), peak A (cesium peroxide) exhibits greater intensity at the 90° emission angle than at the 30° emission angle, while peak B (cesium superoxide) and peak C (cesium superoxide) exhibit weaker levels of intensity at the 90° emission angle.

One may wonder if the angular dependence is due to the polarization of an incidence beam, instead of surface sensitivity, since previous investigators have reported that the valence band spectra exhibit wide variations in amplitude, depending upon the polar angle of emission and optical polarization [23 – 25]. In order to verify the origin of the angular dependence of photoemission spectra, we performed Near Edge X-ray Absorption Fine Structure (NEXAFS) in O1s K-edge experiments on the activated InP

photocathode. If oxygen molecules in the Cs/O activation layer are oriented either vertically or laterally, NEXAFS spectra should show a resonance at certain incidence angle, either a glancing incidence angle (p-polarization, Figure 2.5(a)) or a normal incidence angle (s-polarization, Figure 2.5(b)). Our NEXAFS results (Figure 2.6), however, do not exhibit any sharp features, which should be very distinct, as reported in the literature, if there is polarization dependence [26 – 33]. This is clear evidence that the angular dependence of our PES spectra is not due to the polarization of the beam, but to the surface sensitivity; hence, we should be confident that oxygen molecules do not have a fixed orientation in the Cs/O activation layer. Another clear piece of evidence which enable us to exclude polarization-dependence is that O1s core level spectra do not have any polarization-dependence, because of the spherical distribution of electron density.

Figure 2.7 illustrates a simplified model of cesium peroxides and superoxides in the activation layer on an InP(100) substrate. The model is based upon the structure of bulk Cs peroxides and superoxides [34], and captures the most important fact: that oxygen is in the same plane as Cs with superoxides, whereas oxygen is placed between Cs planes with peroxides, as shown in Figure 2.8. These two Cs oxide species are found to be laterally distributed, instead of being vertically stacked, because of the thickness of the Cs/O layer, as shown in Figure 2.7. We calculated the total thickness of the activation layer (t) from the attenuation of the In4d core level intensity by a Cs/O layer, and the estimated thickness is $7 \pm 2 \text{ \AA}$. The equation used for the estimation of the Cs oxide layer is shown as Equation 2.1, where I'_{In4d} is the intensity of the In4d core level after activation, and I^0_{In4d} is the intensity before activation. λ is the inelastic mean free path of electrons, which here is estimated as $5 \pm 2 \text{ \AA}$ for the photoelectrons from the In4d core

level at a photon energy of 70 eV (kinetic energy of 48 eV). This Cs/O layer thickness is much less than the estimated thickness of vertically-distributed Cs oxides ($\sim 13 \text{ \AA}$), so we can exclude a vertical distribution, which has Cs superoxides lying on top of Cs peroxides.

$$I'_{In4d} = I^o_{In4d} \bullet e^{-t/\lambda} \quad (2.1)$$

According to the structural difference of each Cs oxide, the angular dependence of the oxygen intensity in each oxide species is different in Cs peroxides and in Cs superoxides, as reflected in Equations 2.2 and 2.3, where I_p is the total intensity of oxygen in the peroxides, and I_s is the total intensity of oxygen in the superoxides; A is a common coefficient, which includes parameters like cross-sectional area, etc.; X_p and X_s are the coverage of cesium peroxides and superoxides. θ is an emission angle; and t is the total thickness of a Cs/O layer. In Equation 2.2, the oxygen in Cs peroxides is attenuated by the half of the Cs/O layer which has the thickness of $t/2$. In Equation 2.3, the first term is the oxygen in the second layer of Cs superoxides, which is attenuated by the whole Cs/O layer of thickness t ; whereas the second term is the oxygen in the first layer of Cs superoxides, which is not attenuated.

$$I_p = A \bullet X_p e^{-t/2\lambda \sin \theta} \quad (2.2)$$

$$I_s = A \bullet X_s e^{-t/\lambda \sin \theta} + A \bullet X_s \quad (2.3)$$

Using these equations and given parameters, we performed least squares fitting of the experimental data of I_p/I_s using calculated relative oxygen intensities, based upon the model. Values of I_p/I_s at each emission angle are expressed, as shown in Equation 2.4. The sum of squares of the difference between the experimental value of I_p/I_s and the calculated values containing X_p and X_s is expressed in Equation 2.5.

$$\frac{I_p}{I_s} = \frac{X_p e^{-7/10 \sin \theta}}{X_s e^{-7/5 \sin \theta} + X_s} \quad (2.4)$$

$$S = ((I_p/I_s)_{90^\circ} - 1.049)^2 + ((I_p/I_s)_{60^\circ} - 0.842)^2 + ((I_p/I_s)_{45^\circ} - 0.745)^2 + ((I_p/I_s)_{30^\circ} - 0.565)^2 \quad (2.5)$$

The best fit, which leads to the minimum S in Equation 2.5, yields 2.71 as the ratio of X_p/X_s ($X_p + X_s = 1$). Based upon this result, theoretical relative intensities were calculated and compared with the experimental data, as shown in Figure 2.9. The error bar for the calculated value is from the uncertainties of the electron escape depth λ , and is not related to experimental error in the common sense. The calculated values and the experimental data agree with each other well, although there are some discrepancies between the two. These discrepancies might be due to the simplicity of the lateral distribution model, the approximation of the attenuation using Equations 2.2 and 2.3, and the surface roughness, which can affect the uniformity of the Cs/O layer. In addition, there may be some chemical or physical deviations from a well-defined Cs/O layer, since the thinness of the Cs/O layer may lead to the distorted structure of oxides in the Cs/O layer, compared with bulk Cs oxides.

2.3.2 Time Decay Results of ADPES of Valence Band

The QE of an activated InP photocathode decayed in our vacuum system, accompanied by changes in the intensities of both the O1s and VB spectra [2]. In short, peaks related to superoxides grew, while peaks related to peroxides became smaller over time; and, at the same time, substrate oxidation mainly on In sites grew. The angular dependence of O1s and VB spectra were tracked in this decay process. For the O1s spectra, we found that the angular dependence was kept during decay, as was the angular dependence of VB spectra in the early state of decay. In the later stage of decay, peaks A and B in VB still kept this angular dependence. Peak C, however, reversed its angular dependence later (Figure 2.3(d)). We believe that this is because peak C is composed of two components, cesium superoxides and the O2p bonding orbital of substrate oxides, which cannot be resolved due to the closeness of the peak positions. At the beginning of decay (i.e. Figures 2.3(a) and (b)), the contribution of oxygen intensity from substrate oxides is very small, so that the angular dependence of peak C at the beginning of decay largely is due to the characteristics of the Cs superoxide component. As temporal decay proceeds, the InP substrate is oxidized [2]. Since substrate oxide is formed on the substrate, and the Cs oxide layer is on top of it, substrate oxides are located deeper than both the Cs superoxides and Cs peroxides. Therefore, it exhibits the opposite dependence as Cs superoxides (i.e. relatively larger at normal emission angles versus relatively smaller at larger emission angles). Because peak C is due to both Cs superoxides and substrate oxides, this substrate oxide leads to the reversed angular dependence of peak C, shown in Figure 2.3(d). It needs to be pointed out that peak B also is partly due to

substrate oxides. The cross-sectional area of substrate oxides for peak B, however, is not as large as for peak C, such that the angular dependence is not reversed by the substrate oxide contribution. The overall angular dependence of the valence band spectra at different times is depicted in Figure 2.10. The angular dependencies of peak A and B remain the same until 2 hours after the completion of activation. Peak A, however, disappears after 2 hours, as shown in the figure.

Since we know that the O1s and the VB spectra change with time, one might question if our earlier angular dependence actually is due to this time decay, since different spectra were measured at different times. Another ADPES experiment was performed to verify that the angle dependences of the valence band and the O1s core level spectra are not due to time-decay, but to the surface sensitivity of each oxide species. As shown in Figure 2.11(a), the peroxide peak recovers its intensity when the emission angle changes from 30° (13 minute) to 90° (20 minute). This trend also is evident in the O1s core level spectra of Figure 2.11(b). These intensity changes in peaks A and B are against the trend of time-decay, in which the peroxide peak becomes smaller with time, which means that it mostly is due to angular dependence.

2.4 Conclusions

A very thin Cs/O layer ($7 \pm 2 \text{ \AA}$) was observed on the activated surface of the InP(100) photocathode. We identified two different kinds of cesium oxide, as well as a substrate oxide in the valence band spectra and core level spectra of O1s, after activation of InP. We identified those cesium oxides as cesium peroxides and cesium superoxides, according to our ADPES data and the previous literature. Oxygen molecules in peroxides

and superoxides displayed different angular dependences in both valence band spectra and O1s core level spectra, which leads us to propose a simple lateral distribution model for cesium superoxides and cesium peroxides. The relative intensities of oxygen molecules in cesium superoxides and peroxides were calculated, based upon this layer model, and they matched well with the ADPES O1s core level data.

2.5 References

- ¹ R. L. Bell, Negative Electron Affinity Devices, Clarendon, Oxford (1973)
- ² Y. Sun, Ph.D. Dissertation, Stanford University (2003)
- ³ A. H. Sommer, H. H. Whitaker, B. F. Williams, Appl. Phys. Lett. **17**, 273 (1970)
- ⁴ B. F. Williams, J. J. Tietjen, Proc. IEEE **59**, 1489 (1971)
- ⁵ D. G. Fisher, R. E. Enstrom, J. S. Esher, B. F. Williams, J. Appl. Phys. **43**, 3815 (1972)
- ⁶ C. Y. Su, W. E. Spicer, I. Lindau, J. Appl. Phys. **54**, 1413 (1983)
- ⁷ H. Sonnenberg, Appl. Phys. Lett. **14**, 289 (1969)
- ⁸ J. J. Uebbing, L. W. James, J. Appl. Phys. **42**, 5095 (1971)
- ⁹ W. E. Spicer, Appl. Phys. **12**, 115 (1977)
- ¹⁰ M. G. Burt, V. Heine, J. Phys. C, **11**, 961 (1978)
- ¹¹ Y. Sun, Z. Liu, F. Machuca, P. Pianetta, W. E. Spicer, J. Vac. Sci. Technol. A **21**, 219 (2003)
- ¹² P. Pianetta, In Situ Processing by Gas or Alkali Metal Dosing and by Cleavage, chapter of the book Specimen Handling, Preparation, and Treatments in Surface Characterization, edited by Czanderna et al. Kluwer Academic / Plenum Publishers, New York, (1998)
- ¹³ P. Pianetta, I. Lindau, C. M. Garner, W. E. Spicer, Phys. Rev. B **18**, 2792 (1978)
- ¹⁴ C. Y. Su, I. Lindau, W. E. Spicer, Chem. Phys. Lett. **87**, 523 (1982)
- ¹⁵ B. Woratschek, W. Sesselmann, J. Kuppers, G. Ertl, J. Chem. Phys. **86**, 2411 (1987)
- ¹⁶ J. Jupille, P. Dolle, M. Besancon, Surf. Sci. **260**, 271 (1992)
- ¹⁷ P. Dolle, M. Tommasini, J. Jupille, Surf. Sci. **211/212**, 904 (1989)
- ¹⁸ E. Bertel, F. P. Netzer, G. Rosina, H. Saalfeld, Phys. Rev. B, **39**, 6082 (1989)
- ¹⁹ G. Ebbinghaus, W. Braun, A. Simon, Phys. Rev. Lett. **37**, 1770 (1976)
- ²⁰ A. Simon, J. Sol. Stat. Chem. **27**, 87 (1979)
- ²¹ G. Ebbinghaus, A. Simon, Chem. Phys. **43**, 117 (1970)

- ²² F. Machuca, Z. Liu, Y. Sun, P. Pianetta, W. E. Spicer, R. F. W. Pease, J. Vac. Sci. Technol. B, **21**, 1863 (2003)
- ²³ J. Smith, J. Anderson, G. J. Lapeyre, Phys. Rev. Lett., **37**, 1081 (1976)
- ²⁴ E. W. Plummer, T. Gustafsson, Science, **198**, 165 (1977)
- ²⁵ K. C. Prince, G. Paolucci, A. M. Bradshaw, Surf. Sci., **175**, 101 (1986)
- ²⁶ J. Stohr, *NEXAFS spectroscopy*, New York, Springer (1992)
- ²⁷ J. Stohr, D. A. Outka, Phys. Rev. B, **36**, 7891 (1987)
- ²⁸ J. Stohr, R. Jaeger, Phys. Rev. B, **26**, 4111 (1982)
- ²⁹ J. Stohr, J. L. Gland, W. Eberhardt, D. Outka, R. J. Madix, F. Sette, R. J. Koestner, U. Doebler, Phys. Rev. Lett., **51**, 2414 (1983)
- ³⁰ M. W. Ruckman, J. Chen, S. L. Qiu, P. Kuiper, M. Strongin, Phys. Rev. Lett., **67**, 2533 (1991)
- ³¹ D. Norman, J. Stohr, R. Jaeger, P. J. Durham, J. B. Perdry, Phys. Rev. Lett., **51**, 2052 (1983)
- ³² U. Hofer, A. Puswchmann, D. Coulman, E. Umbach, Surf. Sci., **211/212**, 948 (1989)
- ³³ W. Worth, J. Stohr, P. Feulner, X. Pan, K. R. Bauchspiess, Y. Baba, E. Hudel, G. Rocker, D. Menzel, Phys. Rev. Lett., **65**, 2426 (1990)
- ³⁴ M. Pedio, M. Benfatto, S. Aminpirooz, J. Haase, Phys. Rev. B, **50**, 6596 (1994)

| Ionic oxygen | Binding energies (eV) | References |
|--------------------------|--|--|
| Peroxide O_2^{2-} | 3.3, 6.4, 7.8 2.6, 5.5, 7.0 3.3, 6.1, 7.5 3.0, 6.0, 7.4 3.1 | Su et al ⁴ Dolle et al ⁷ Woratschek et al ⁵ Jupille et al ⁶ This study |
| Superoxide O_2^{1-} | 4.7, 5.8, 8.5, 10.7 2.8, 3.4, 6.3, 8.4 3.9, 5.2, 8.0 3.4, 4.8, 7.3, 9.8 5.1, 9.0 | Su et al ⁴ Dolle et al ⁷ Woratschek et al ⁵ Jupille et al ⁶ This study |

Table 2.1 Binding energies of multiplet peaks of cesium oxides in the valence band spectra

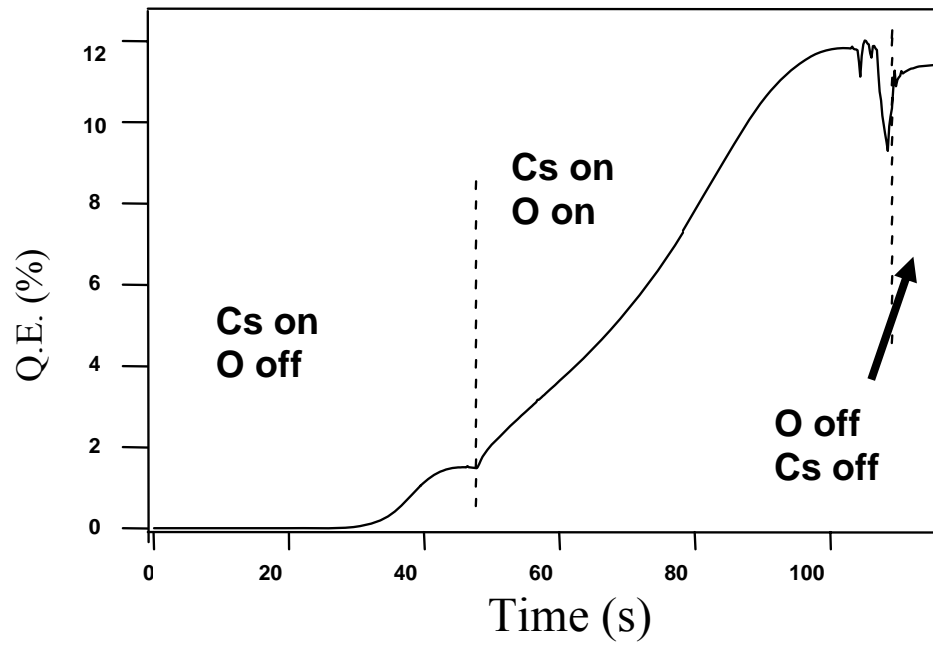


Figure 2.1 QE vs Time curve during activation. For this activation, there was no need to modulate the amount of oxygen once it is initially matched with Cs flux. The normal cases of activation require further modulations of the amount of oxygen.

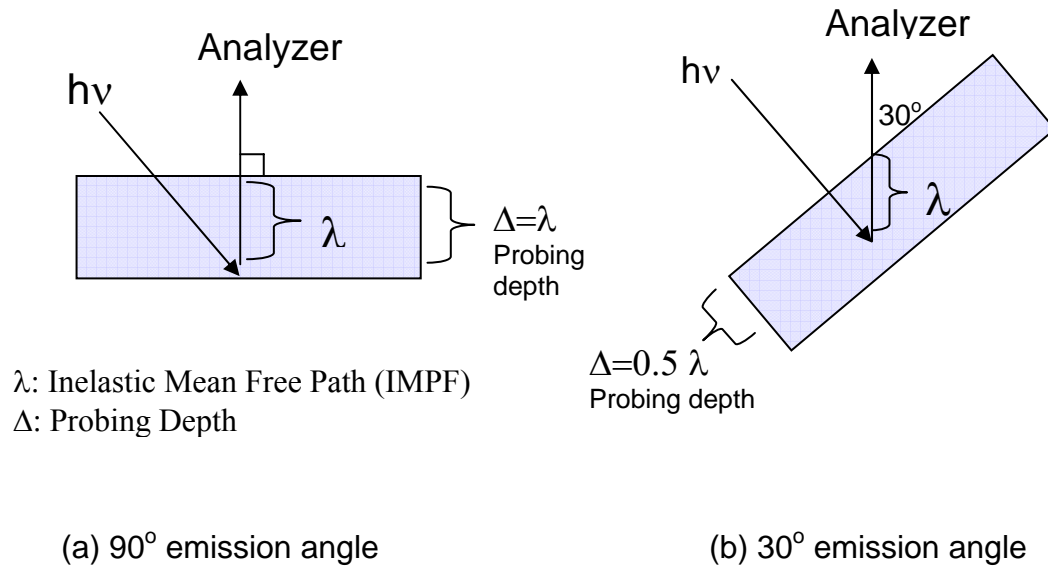


Figure 2.2 Sample configuration with respect to the analyzer. In the configuration of (a), the probing depth is maximized to deliver relatively bulk sensitive information, while in the (b) configuration the probing depth is small so it is more surface sensitive.

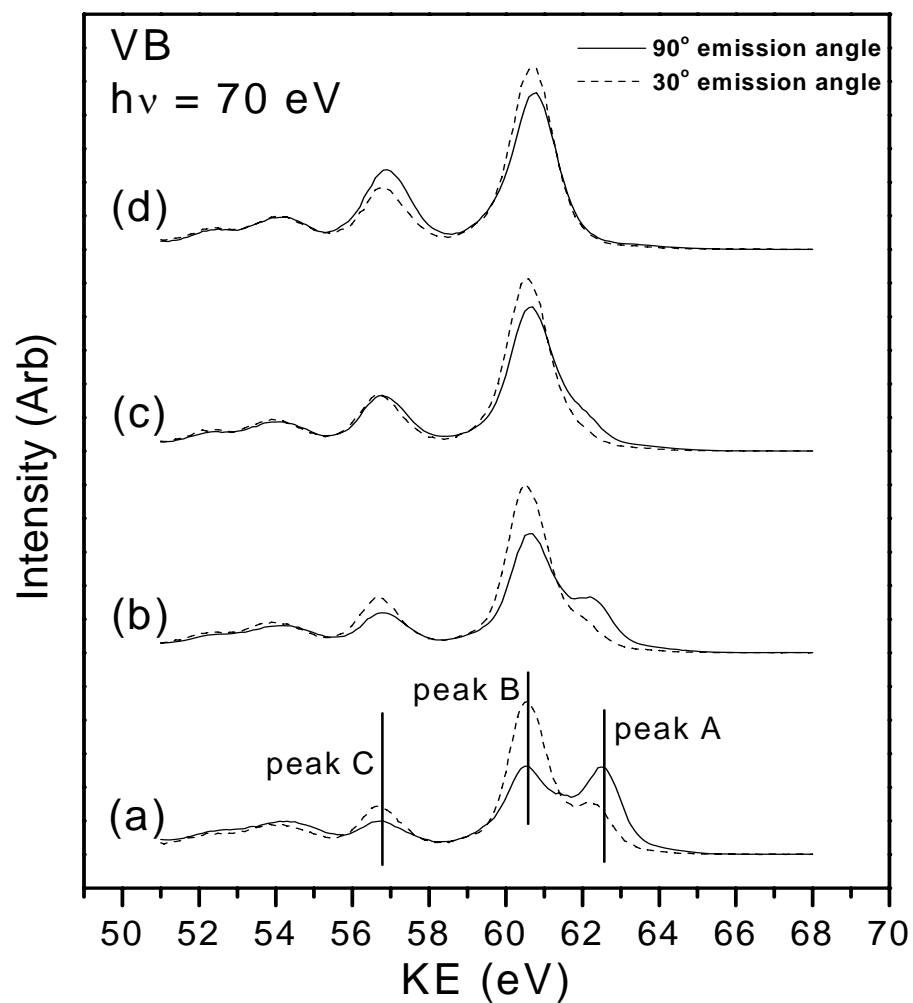


Figure 2.3 ADPES valence band spectra at $h\nu = 70$ eV (solid line: 90° emission angle, dotted line: 30° emission angle) at different times after activation. (a) 5 minutes (b) 70 minutes (c) 148 minutes (d) 424 minutes after activation

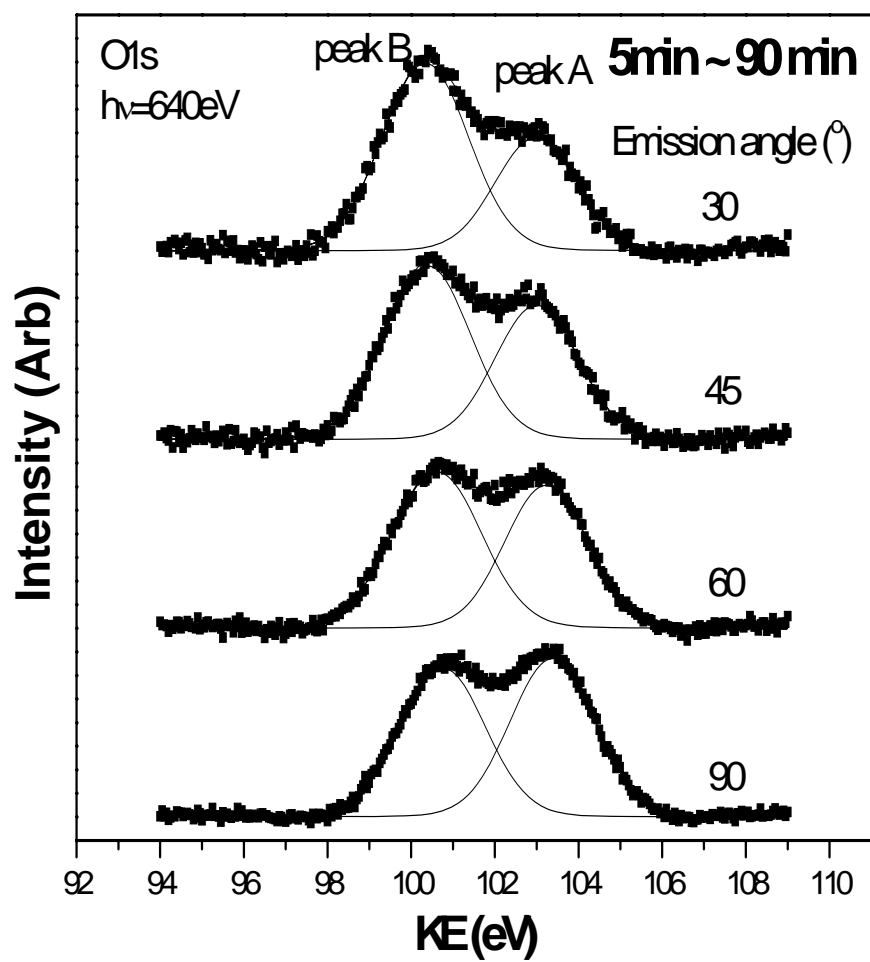
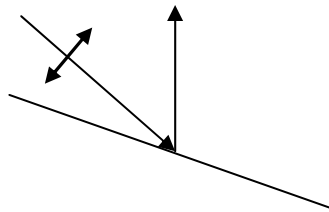
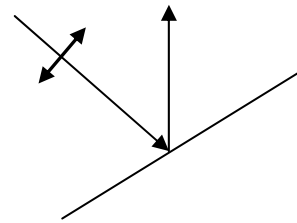


Figure 2.4 O1s core level spectra at $h\nu = 640$ eV. Spectra are taken at four different emission angles. The 90° emission angle is the most bulk sensitive, while the 30° emission angle is the most surface sensitive.



P-polarization
Glancing incidence

(a)



S-polarization
Normal incidence

(b)

Figure 2.5 Polarization at each incidence angle (a) P-polarization at glancing incidence angle (b) S-polarization at normal incidence angle

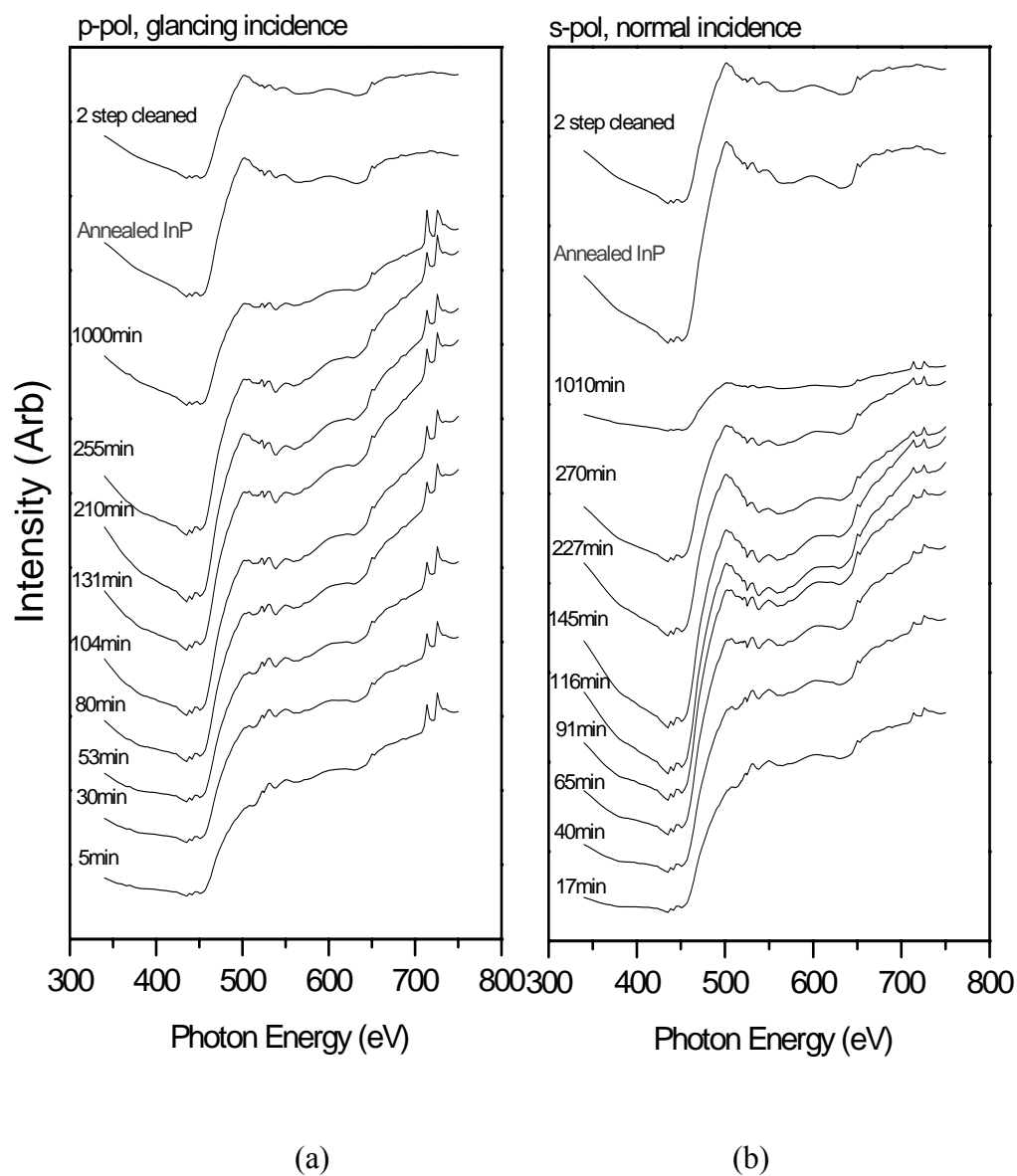


Figure 2.6 NEXAFS of O K-edge data on InP photocathode at different times after activation with (a) a glancing incidence angle (p-polarization) (b) a normal incidence angle (s-polarization)

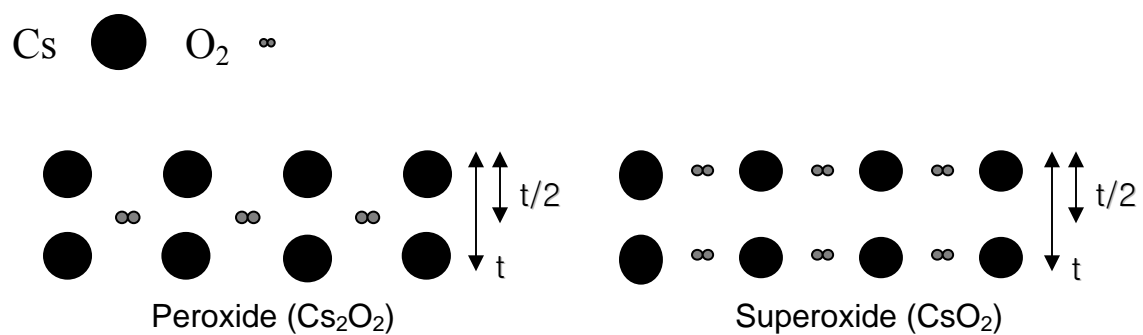


Figure 2.7 Layer model of cesium superoxides and peroxides in the activated surface of InP(100) photocathode. The total thickness of the activation layer (t) is $\sim 7\text{\AA}$.

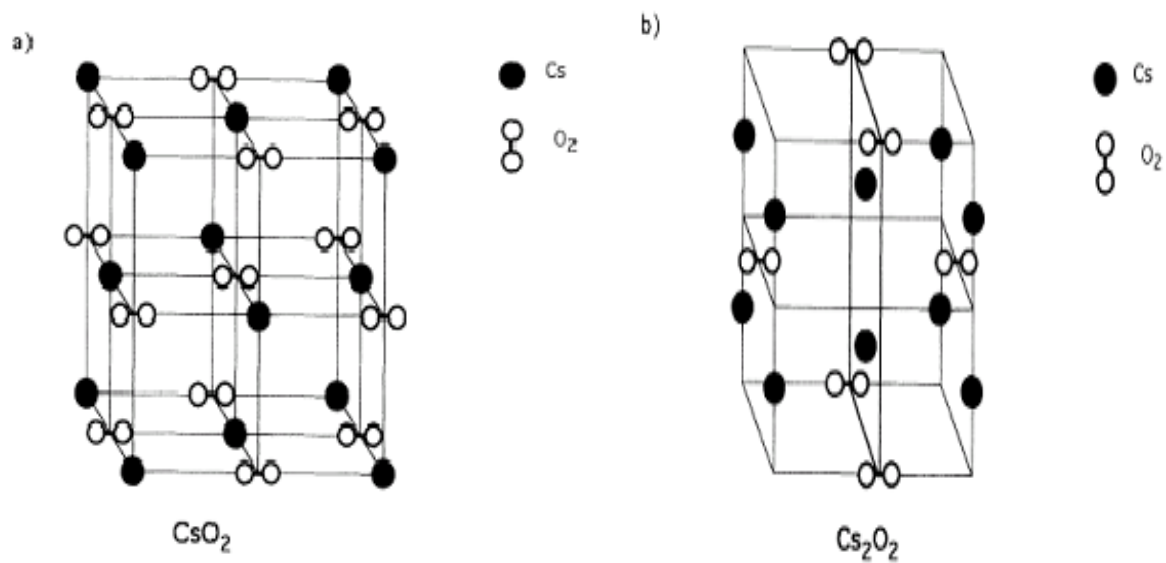


Figure 2.8 (a) Bulk Cs superoxide: calcium carbide structure (b) Bulk Cs peroxide: distorted calcium fluorite structure [34]

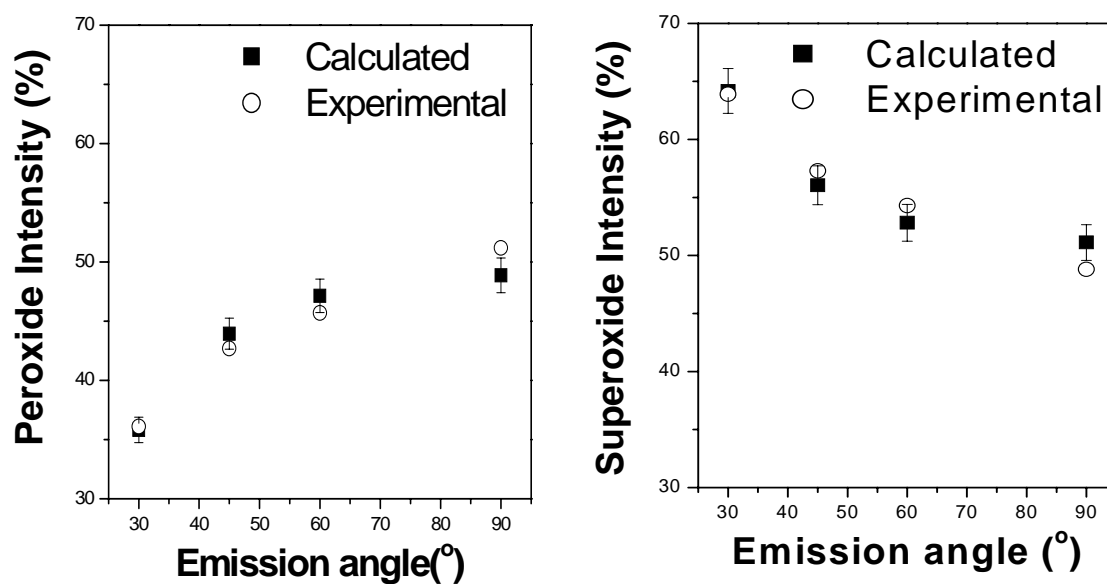


Figure 2.9 Relative intensity of peroxides ($I_s/(I_s+I_p)$) plot vs the emission angle and relative intensity of superoxides ($I_s/(I_s+I_p)$) plot vs the emission angle

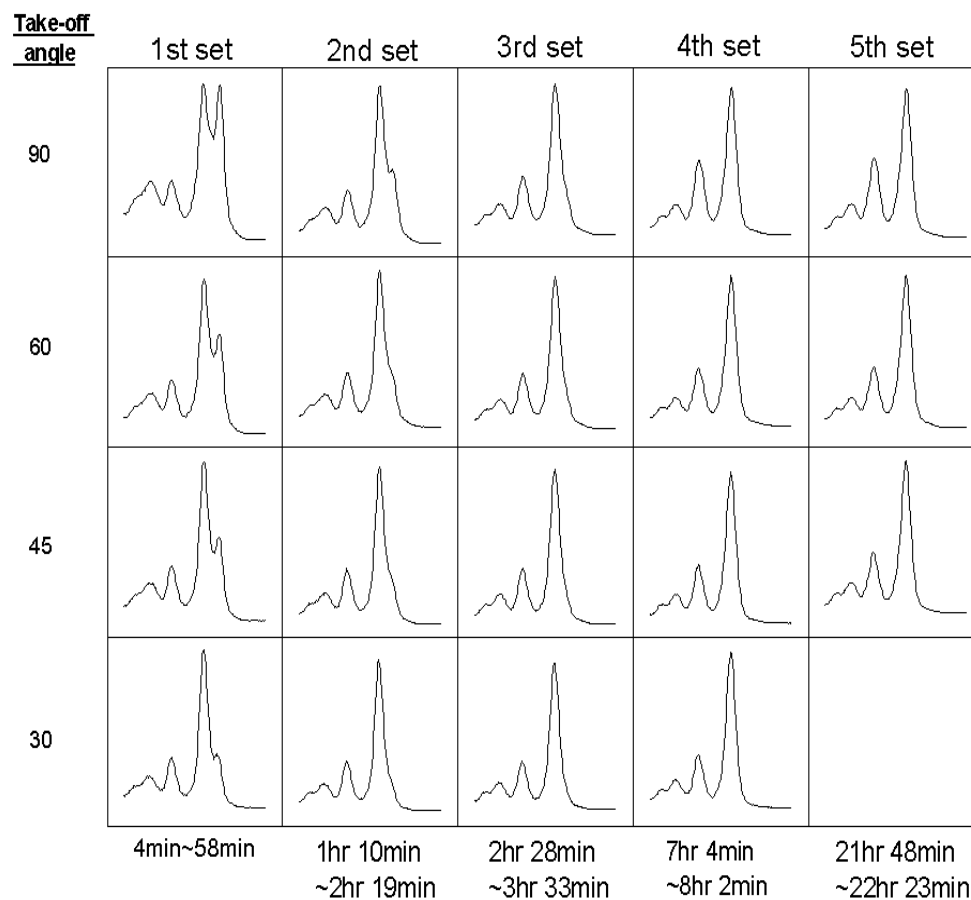
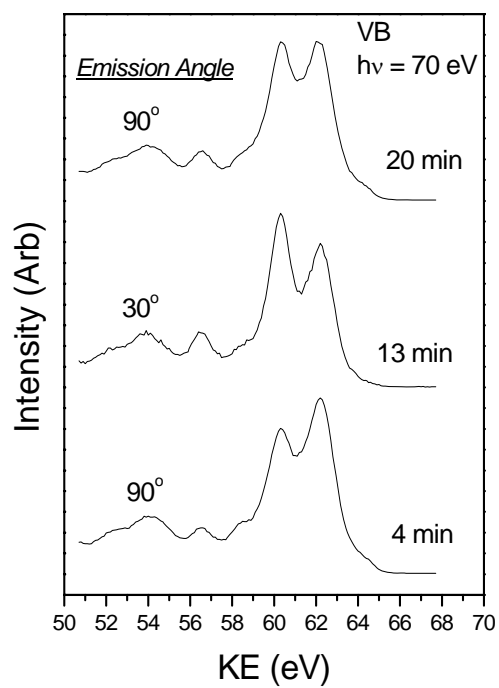
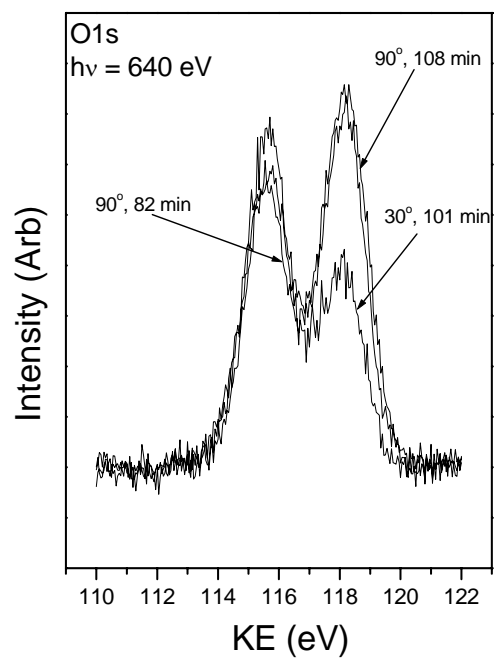


Figure 2.10 Valence band spectra at different times and at different take off angles. 90° take off angle is the most bulk sensitive, and 30° take off angle is the most surface sensitive.



(a)



(b)

Figure 2.11 VB and O1s core level spectra at different angles and different times (a) VB photoemission spectra at 70 eV (b) O1s core level spectra at 640 eV photon energy

3. QUANTUM EFFICIENCY DECAY MECHANISM OF THE INP(100) PHOTOCATHODE

3.1 Introduction

Negative electron affinity (NEA) III-V photocathodes have been used widely in the technological applications of sensitive photomultipliers, Gen-III night vision devices, and e-beam sources, due to their beam properties, such as high sensitivity and high spin-polarization [1], and low energy spread [2, 3]. One of the concerns raised in the usage of Cs/O-activated photocathodes is their relatively short lifespan, since industry requires that they perform reliably for long periods. This lifespan issue is precipitated by the fact that the Cs/O layer of an activated NEA photocathodes is extremely sensitive to contamination, which destroys the NEA properties of the surface and reduces its Quantum Efficiency (QE) [4]. One effort being made to extend the lifespan of photocathodes is to provide cesium atoms to a cathode, either continuously or intermittently, during its operation. This supply of Cs maintains the proper cesium balance at the surface, thereby preserving the quality of the emitting surface [5 - 9].

For some applications, such as night vision goggles, a GaAs-based photocathode is sealed in glass tubes, which has the environment of Cs overpressure, so that the surface can be kept Cs rich to prolong the lifespan of the cathode. However, this sealed tube is not applicable to open systems, like e-beam lithography. To identify some way to achieve a stabilized surface in an open system, it is necessary to know the exact chemistry and physics of the surface. This study aims to provide these pieces of information, as well as

basic scientific knowledge to aid in the understanding of the activated surface, which is crucial for future development of III-V based photocathodes.

In this study, we investigated the decay mechanism of a Cs/O-activated InP(100) photocathode by means of synchrotron radiation photoemission (SR-PES). The decay of QE and the increase in electron affinity are due to the transformation of Cs peroxides into Cs superoxides and subsequent substrate oxidation. These changes are illustrated in our simple lateral distribution model, presented in the previous chapter, and are the consequence of the thermal stability of Cs superoxides compared to Cs peroxides at room temperature, whenever residual oxygen is present. In our study, the redeposition of Cs atoms was performed to simulate a sealed photocathode tube in our UHV system. We found that the redeposited Cs atoms 1) recover QE by building up partial dipoles; and 2) slow down Cs peroxides from transforming into Cs superoxides.

3.2 Experiment

A P-type InP sample was prepared and activated by Cs and oxygen, as described in Chapter 2. Photoemission spectroscopy experiments and quantum efficiency measurements were done during the decay of photocathodes. Electron affinities of photocathodes were measured, during decay, from the low energy cut-off of energy distribution curves (EDC) of photoelectrons emitted from the cathode.

3.3 Results & Discussion

3.3.1 Decrease in Photocurrent and Chemical Changes during Decay

After the sample is activated, the photocurrent starts to decrease, and the decay is usually different with different chamber pressures. Two typical decay curves of QE are presented in Figure 3.1. The decay rate with a chamber pressure at 2×10^{-10} torr is significantly slower than at 8×10^{-10} torr, which indicates that the amount of residual oxygen in the chamber is one of the factors that determines the decay rate, since the total amount of oxygen in the Cs/O activation layer increases during decay [10]. This decay phenomenon is due to the increase in the vacuum level because, with a higher vacuum level (i.e. higher work function), fewer electrons can escape from the surface.

Since electron affinity is the difference between the vacuum level and the bulk conduction band minimum, the increase in the vacuum level is the same as the increase in electron affinity. Electron affinity is calculated from the low energy cut-off of energy spread measurements, using a 1.96 eV He-Ne Laser. A 5-volt negative bias is applied to the sample, causing the photo-excited electrons to be collected in a hemispherical energy analyzer, which has a minimum 40 meV energy resolution, for subsequent energy analysis. The work function of the energy analyzer is predetermined by the position of the Au4f core level spectra, and also corroborated by the Au Fermi level. Figure 3.2 reveals a simplified band diagram. The Fermi levels initially were lined up between the sample and analyzer because they are in electric contact. The result of the Fermi level alignment is the contact potential between the sample and analyzer, which is the difference in their work function ($-\phi_a + \phi_s$). Photoelectrons from the sample will be either accelerated or decelerated by this potential (depending upon the values of ϕ_a and ϕ_s) when they reach the analyzer, so that the kinetic energy of the photoelectrons when entering the analyzer will be changed by $(-\phi_a + \phi_s)$. When we applied this bias to the

sample, the kinetic energy of photoelectrons reaching an analyzer was changed from the kinetic energy just out of the surface by the amount of $(Bias - \phi_a + \phi_s)$, as described in Equation 3.1. We can obtain ϕ_s by measuring the cutoff of the EDC curve, as shown in Equation 3.2, because the kinetic energy just out of the surface is 0 at the cutoff.

$$E_k^a = E_k^s + Bias - (\phi_a - \phi_s) \quad (3.1)$$

$$\phi_s = E_k^a - Bias + \phi_a (E_k^s = 0) \quad (3.2)$$

We then need to calculate the electron affinity from ϕ_s . The work function ϕ_s is the difference between the vacuum level (E_{vac}) and the Fermi level (E_F).

$$\phi_s = E_{vac} - E_F$$

$$\Rightarrow E_{vac} = E_F + \phi_s$$

Electron Affinity (χ) is the difference between the vacuum level and the conduction band minimum (E_{CBM}).

$$\chi = E_{vac} - E_{CBM}$$

$$= E_{vac} - E_{VBM} - E_G = E_F + \phi_s - E_{VBM} - E_G$$

$$= (E_F - E_{VBM}) + \phi_s - E_G$$

... where E_{VBM} is the energy of the valence band maximum and E_G is the band gap. The difference between the Fermi level and the valence band maximum was calculated from the doping level of our sample, and was determined to be 0.04 eV. Since E_G is known (1.34 eV) and the work function ϕ_s is calculated from equation 3.2, the

electron affinity can be calculated easily. The resulting electron affinity increases with time, as shown in Figure 3.3. From the plot, we can see that, just after activation, the surface is NEA (i.e. Electron Affinity is negative); but, after awhile, the electron affinity changes to positive.

This decay of QE as a result of changes in electron affinity is due to the chemical changes of a Cs/O activation layer, as evidenced by the photoemission spectra of the O1s core level and the valence band in Figure 3.4, and by the oxidation of the InP substrate, as shown in Figure 3.5. As shown in Figure 3.4(a), the higher kinetic energy peak (peroxide peak) decreases in intensity with time, while the lower kinetic energy peak (superoxide peak) increases in intensity. This change in intensities of the two peaks also is apparent in the valence band spectra at different times after activation (Figure 3.4(b)); the peroxide peak decreases and the superoxide peak increases. We were able to observe the oxidation of the substrate during decay, by the de-convolution of the In4d core level spectra, as shown in Figure 3.5. The oxide peak on the left side became larger, while the cesium-induced peak decreased significantly in the area during decay. These In4d core level spectra show that the substrate has been oxidized. The P2p core level reveals the same trend: a reduction in the Cs induced component and an increase in the oxide component [10].

To understand why those chemical changes reduce quantum efficiency, we first need to look into the dipole model of our NEA photocathode. There initially is a potential barrier on the surface, due to the work function of the sample, as shown in Figure 3.6(a). When a surface dipole is formed, the electric field is created perpendicular to the surface, so that the surface dipole changes the potential gradually, in a linear way, as shown in

Figure 3.6(b). Since the thickness (t) of the Cs/O activation layer is very thin, photoelectrons can tunnel through the new potential barrier on the surface, such that the band diagram is simplified, as shown in Figure 3.6(c). There are two sources of dipoles formed on the photocathode surface: 1) A Cs-induced surface dipole (a dipole between the Cs and the substrate); and 2) dipoles in the Cs/O layer. Cs-induced surface dipoles on semiconductors are due to the charge transfer from Cs to charged substrate. This charge transfer makes the Cs layer positively charged and the substrate negatively charged; thus, dipoles are constructed, oriented to lower the surface barrier for electrons (~ 3.4 eV for GaAs) [11], which leads to electron affinity reducing as a function of coverage [12]. The strength of the dipoles in the Cs/O layer, however, is not well understood quantitatively. It involves accurately calculating the position of all the Cs and oxygen atoms at the surface, as well as the shape of their orbital, so that an accurate charge distribution of the Cs/O layer can be obtained. Our simple model of the surface given in the previous chapter does not have this quantitative information, so more detailed work on the theoretical simulation, which involves intensive computation, is needed for this purpose. However, a qualitative explanation was given by Zhi Liu [11].

The decay of QE can be explained by the transformation of Cs peroxides into Cs superoxides and the oxidation of a substrate. We believe that the dipole strength of Cs peroxides is larger than the dipole strength of Cs superoxides, because of the relative position of oxygen molecules to Cs atoms, in accordance with the simplified structure model discussed in Chapter 2. In Cs superoxide structure, dipoles (Cs/O layer) formed by the positively-charged Cs ions and negatively-charged O_2^{-1} anions are in the horizontal direction. No net potential drop is provided in the vertical direction. In Cs peroxide

structure, the situation is a little more complicated. The oxygen is sandwiched between two layers of Cs atoms; then you have a dipole from oxygen in the top layer of Cs and a dipole from oxygen in the bottom layer of Cs. At first glance, these two dipoles should cancel each other out, because they are in opposite directions. However, if we look carefully, we should notice that these two layers of Cs atoms are not the same. In the top layer, the Cs atoms transfer their valence electrons to oxygen, thus becoming +1 charged. The Cs atoms in the bottom layer not only donate their charge to oxygen, but to the substrate as well. The nominal charge state still is +1. However, due to the fact that the InP substrate does not attract the electron charge as strongly as oxygen, the charge is shared slightly between Cs and InP. So the real charge state is less than one. Then the dipole from the oxygen to the top layer of Cs actually is slightly larger than the dipole from the oxygen to the bottom layer of Cs. The net effect is that there is a small dipole in the Cs/O layer to help reduce the work function of the photocathode. Substrate oxidation also leads to a decrease in QE, because the substrate oxide reduces the charge transfer between Cs atoms and InP substrate; thus, this component of the dipole is reduced [10].

Figure 3.7 illustrates the decay steps of a Cs/O layer, based upon the simplified structural model. Early in decay, the residual oxygen molecules approach the surface of the Cs/O layer, as shown in Figure 3.7(a). As the residual oxygen molecules come into the activation layer, oxygen molecules in the Cs peroxides are forced down to the second layer of Cs atoms, as shown in Figure 3.7(b), (c), and the resulting chemical species is Cs superoxide. Some oxygen molecules in the bottom layer of the activation layer are dissociated and oxidize the substrate, as shown in Figure 3.7(d). This dissociation of O_2^{2-} is facilitated by the filling of the anti-bonding orbital of O_2 [10].

This transformation from Cs peroxides to Cs superoxides also is thermodynamically favorable, since Cs superoxides are more stable than Cs peroxides at room temperature, as shown in Equation 3.2.



According to Equation 3.2, the reaction rate is proportional to the concentration of Cs peroxides, which is proportional to the coverage; consequently, the concentration of Cs peroxides is expected to decrease exponentially, as expressed in Equations 3.3 and 3.4, since the reaction is the first order of $[\text{Cs}_2\text{O}_2]$, and here C is $1/\tau$.

$$\frac{dN_p}{dt} = -N_p \rightarrow \frac{dN_p}{N_p} = -dt \rightarrow d\text{Log}N_p = -dt \rightarrow \text{Log}(N_p / N_p^o) = -C \bullet t \quad (3.3)$$

$$N_p = N_p^o \exp(-t / \tau) \quad \Longrightarrow \quad \text{Log}_e N_p = \text{Log}_e N_p^o - t / \tau \quad (3.4)$$

To calculate the Cs peroxide concentration (coverage), we use 1) the equations in Chapter 2 with the restriction $X_p + X_s (=1)$ being introduced in the denominator to remove the unknown factor in X_p when it is reversely expressed as I_p ; 2) the attenuation term; and 3) an unknown constant from the equation in Chapter 2. In the result of a normal emission configuration and estimated thickness, the concentration of Cs peroxides could be calculated from the oxygen intensities of both Cs peroxides and Cs superoxides, as shown in Equation 3.5. For a particular experiment, this Cs peroxide concentration is

plotted in log scale in Figure 3.8. Overall, it follows a straight line, which conforms to our expectation that the change is exponential. The time constant from the linear fit is found to be 32.7 hours.

$$\begin{aligned}
 \text{Log}_e N_p &= \text{Log}_e C \cdot X_p = \text{Log}_e C \cdot \left(\frac{X_p}{X_p + X_s} \right) = \text{Log}_e C \cdot \left(\frac{I_p e^{a/\lambda}}{I_p e^{a/\lambda} + I_s (1 + e^{-2a/\lambda})} \right) \\
 &= \text{Log}_e C \cdot \left(\frac{I_p (e^{a/\lambda} + e^{-a/\lambda})}{I_s + I_p (e^{a/\lambda} + e^{-a/\lambda})} \right) = \text{Log}_e C \cdot \left(\frac{2.51 \times I_p}{I_s + 2.51 \times I_p} \right)
 \end{aligned} \tag{3.5}$$

This 32.7 hr time constant is consistent with the time constant estimated based upon the oxygen partial pressure in our chamber. For the reaction in Equation 3.2 to occur, Cs peroxides should be in contact with oxygen molecules. If we assume that the probability for Cs peroxides reacting with oxygen molecules is unity when they are in contact, the reaction rate will depend upon the proportion of the oxygen molecules that can reach the Cs peroxides, which is proportional to the partial pressure of the oxygen molecules. It is reasonable to assume that the partial pressure of the oxygen molecules is in the order of 1×10^{-11} torr, since our chamber is not totally sealed; hence, the oxygen concentration in the chamber is similar to the oxygen concentration in free air, and we only care about the order of magnitude. Since 1 L (Langmuir) is 10^{-6} torr·sec, we can estimate how much time we need in order to have 1 ML of oxygen molecules on the surface with the oxygen partial pressure set at 1×10^{-11} torr. The estimated time is 27.8 hrs, which is in the same order of magnitude as the time constant (32.7 hrs) from Equation 3.4. Despite being a crude estimate, this is very close. The fact that the change of Cs oxides is slower with a lower chamber pressure also supports the argument

provided above for this estimate, since the less oxygen is available at lower chamber pressures [10].

If we believe that the reaction of Equation 3.2 occurred in the Cs/O layer, then we should expect that the decrease in Cs peroxide coverage to be matched by the increase in Cs superoxide coverage. The coverage change in Cs superoxides and peroxides also can be expressed in terms of oxygen intensities in O1s core level spectra, as shown in Equations 3.6 and 3.7, based upon our lateral distribution model.

$$\frac{\Delta N_s}{2} = C \bullet I_s (1 + e^{-2a/\lambda})^{-1} - \frac{N_s^o}{2} \quad (3.6)$$

$$\Delta N_p = C \bullet I_p e^{a/\lambda} - N_p^o \quad (3.7)$$

We have compared the relative change in the coverage of Cs peroxides with an initial coverage of $(-\Delta X_p)$ versus the relative change in the coverage of Cs superoxides (ΔX_s) , as shown in Figure 3.9. The increase in Cs superoxide coverage is in reasonable agreement with the decrease in the amount of Cs peroxide coverage. However, there is a small discrepancy between ΔX_s and $-\Delta X_p$ in Figure 3.8, which shows greater changes in superoxide versus peroxide coverage. The substrate oxide can explain the discrepancy between ΔX_s and $-\Delta X_p$, since the substrate is oxidized more while the Cs/O layer undergoes the transformation to more stable Cs superoxides, simply because the interface between InP and Cs oxides is not stable with CsO_2 acting as an oxidant [10]. The lower kinetic energy peak in the O1s core level, which we assigned as a superoxide peak, also contains the contribution of substrate oxides that is difficult to separate out, because of

the closeness of the two sub-peaks. This substrate oxide contribution will make the ‘superoxide’ peak seem larger than it should be, thus creating the discrepancy.

3.3.2 Recesiation Experiments

The supply of Cs atoms on the photocathode surface has been suggested as critical in prolonging the lifetime of GaAs photocathodes [5 – 9]. This idea was borrowed from sealed photocathodes, which has Cs overpressure, so that it lasts for a long time. The long lifespan of sealed photocathode tubes is due to the fact that Cs overpressure can getter contaminants left in the sealed tubes because the tubes are isolated from the environment, oxygen and moisture, which reduce the QE, cannot leak in. In this study, we seek a way to slow down the QE decay of InP photocathodes in an open UHV system. Hence, we supplied repetitive doses of Cs atoms.

Figures 3.10 and 3.11(a) demonstrate the photocurrent curves of a decaying InP photocathode with recesiations. Cs deposition was on and off repeatedly during recesiations. As shown in Figures 3.10 and 3.11(a), the photocurrent was recovered partially by recesiations; that is, we could maintain the photocurrent at a certain level without decay. In Figure 3.11(a), repeated Cs dosing was performed to recover QE after 7 hours of decay. The features observed before 7 hours are due to the results of cesiation, and demonstrate how QE behaves differently with Cs dosing at different states of decay. The QE does not show immediate increases in this early period, because there are sufficient Cs atoms on the surface at the beginning of the decay. Figure 3.11(b) shows the O1s core level spectra during recesiations. The superoxide peak at lower kinetic energies increases only slightly in intensity as time proceeds. The peroxide peak, however, does

not appear to change. Remember that, without recesiations, the peroxide peak will decrease and the superoxide peak will increase considerably during the time period shown in the figure. The relatively constant photocurrent during recesiations is due to the constant amount of Cs peroxides produced during recesiations, which suggests that freshly-deposited Cs atoms prevent Cs peroxides from transforming into Cs superoxides. The partial recovery of the photocurrent each time the Cs is turned on is due to the dipole built up on the surface between the redeposited Cs atoms and the Cs/O layer. This dipole is formed by the charge transfer from freshly-deposited Cs atoms to the Cs/O layer. Figure 3.12 illustrates the behavior of the photocurrent during recesiations: (1) When Cs atoms initially are redeposited on the decaying surface, the surface dipole starts to increase. (2) At the point at which the amount of Cs surpasses the optimum amount so that the mutual depolarization effect dominates [13], the photocurrent reaches its maximum and starts to decrease. (3) Once the Cs deposition stops at the optimum point, the photocurrent begins to decay slowly, because residual oxygen enters the Cs/O layer.

We propose the following model for this photocurrent behavior during decay with recesiations. Figure 3.13 shows the band diagram with the vacuum level. The vacuum level before decay is located below the bulk conduction band minimum, indicated as ' E_v '. Recall that there are two sources of dipoles for our NEA cathode. One is the dipole between the Cs/O layer and the substrate; the other is the dipole built inside the Cs/O layer. For this reason, we separate these two sources to increase the vacuum level, since one is due to substrate oxidation (Δ_1) and the other is due to the transformation of Cs peroxide to Cs superoxide (Δ_2).

Redeposited Cs, by transferring charge to the existing Cs oxide layer, will form a new dipole on the surface. This new contribution of dipole strength will compensate for the loss of dipole strength, due to the transformation of Cs oxide (Δ_2). However, this recovery of dipole strength is not 100 percent, since the resulting Cs/O film is not as good as the optimal film that exists just after activation. In addition, the reaction in Equation 3.1 can be slowed down by freshly-deposited Cs, but cannot be reversed.

The increased vacuum level due to ' Δ_1 ', however, cannot be recovered by recesiations. We know that this change is due to substrate oxidation, which leads to the loss of dipole strength between the Cs oxide layer and the substrate. It is understandable that Cs deposited on top of the Cs oxide layer cannot really affect what happens at this interface. Therefore, oxidation of the substrate cannot be reversed via Cs redeposition. This model successfully explains the photocurrent behavior observed during recesiations, as shown in Figure 3.14. Photocurrent is recovered to a certain level after recesiations, because the partial dipoles are recovered by the redeposition of Cs atoms, which removes the contribution of ' Δ_2 '. Nonetheless, the recovered value is not as high as the initial value, since there has been substrate oxidation so that the contribution ' Δ_1 ' has increased, which is irreversible, even with recesiations. We can see that, to some extent, we are trying to imitate the sealed tube by recesiation, but the effect is not as good as with sealed tubes. First, the volume of the chamber is quite large compared to the volume of the tubes, so it is very difficult to have enough Cs overpressure to getter all the contaminants left in the chamber. Second, the chamber is pumped differentially and the vacuum seals of the chamber are not perfect, such that residual oxygen molecules keep coming into the chamber, unlike what happens with sealed photocathodes. Unless a more effective way to

stabilize the photocathode surface in an open system is developed, an InP-based photocathode will not be an ideal candidate for applications like e-beam lithography, even though it can be used successfully in night vision devices.

3.4 Conclusions

The decay of QE and the increase in electron affinity are attributed to the chemical transformation of Cs oxides in a Cs/O activation layer from Cs peroxides to Cs superoxides, and subsequent substrate oxidation. Cs superoxides are thermally more stable than Cs peroxides with residual oxygen present, and the Cs superoxides tend to dissociate, due to the anti-bonding orbital being filled. This decay procedure is in accordance with the simple lateral distribution model of a Cs/O layer. The coverage of each oxide is expressed as a function of oxygen intensities in O1s core level spectra, based upon the distribution model. Their time-dependence is in agreement with the decay mechanism presented, and is correlated to the partial pressure of oxygen in the chamber. A sealed-tube photocathode was simulated in our UHV system, by providing redeposited Cs atoms on the decaying surface, which seems to recover partial QE by building up new dipole strength, as well as by slowing down Cs peroxides from transforming into Cs superoxides.

3.5 References

- ¹ H. Aoyagi et al, Phys. Lett. A **167**, 415 (1992)
- ² C. S. Feigerle, D. T. Pierce, A. Seiler, R. J. Celotta, Appl. Phys. Lett. **44**, 866 (1984)
- ³ J. Schnieider, A. Baum, G. Winograd, R. Pease, M. McCord, W. Spicer, J. Vac. Sci. Technol. B **14**, 3782 (1996)

- ⁴ P. Sen, D. S. Pickard, J. E. Schneider, M. A. McCord, R. F. W. Pease, A. W. Baum, K. A. Costello, J. Vac. Sci. Technol. B **16**, 3380 (1998)
- ⁵ C. A. Sanford, Ph.D. Thesis, Cornell University, Ithaca, NY (1990)
- ⁶ A. W. Baum, J. E. Schneider, R. F. W. Pease, M. A. McCord, W. E. Spicer, K. A. Costello, V. W. Aebi, J. Vac. Sci. Technol. B **15**, 2707 (1997)
- ⁷ P. E. Oettinger, T. D. Howard, J. T. Fronduto, U. S. Patent No. 4,970,392
- ⁸ F. C. Tang, M. S. Lubell, K. Rubin, A. Vasilakis, Rev. Sci. Instrum. **57**, 3004 (1986)
- ⁹ J. X. Zhou, D. E. Golden, J. E. Furst, Nucl. Instrum. Methods B **56/57**, 1171 (1991)
- ¹⁰ Y. Sun, Z. Liu, D.-I. Lee, P. Pianetta, In Preparation
- ¹¹ Z. Liu, Ph.D. Dissertations, Stanford University (2005)
- ¹² J. Topping, Proc. R. Soc. London A 114, **67** (1927)
- ¹³ R. L. Bell, *Negative Electron Affinity Devices*, Clarendon, Oxford (1973)

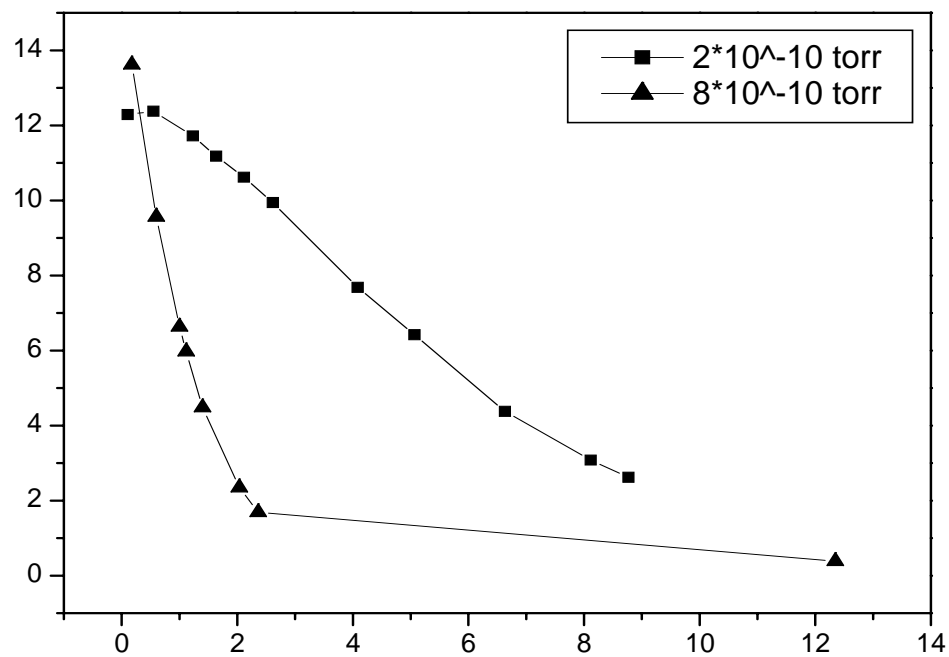


Figure 3.1 Decrease of photocurrent with time at different chamber pressures

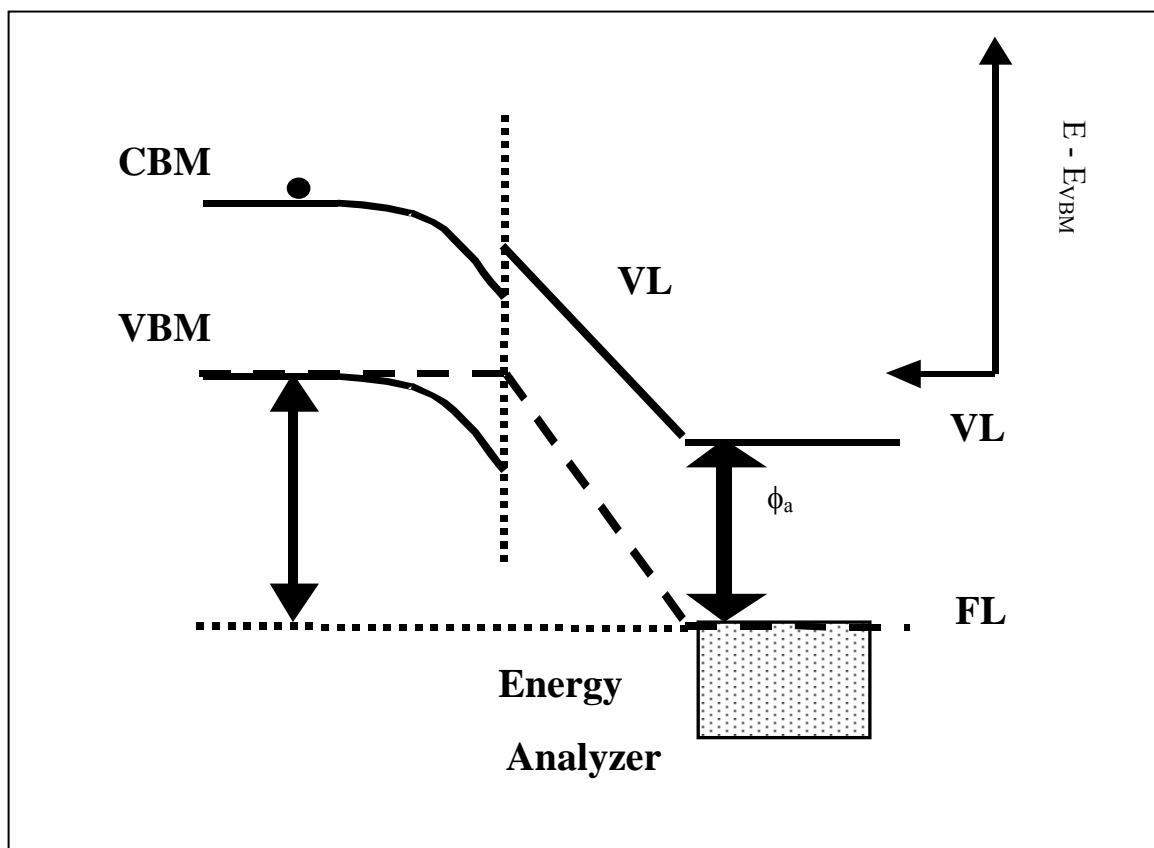


Figure 3.2 Band diagram of the NEA surface under an applied bias between the sample and an analyzer

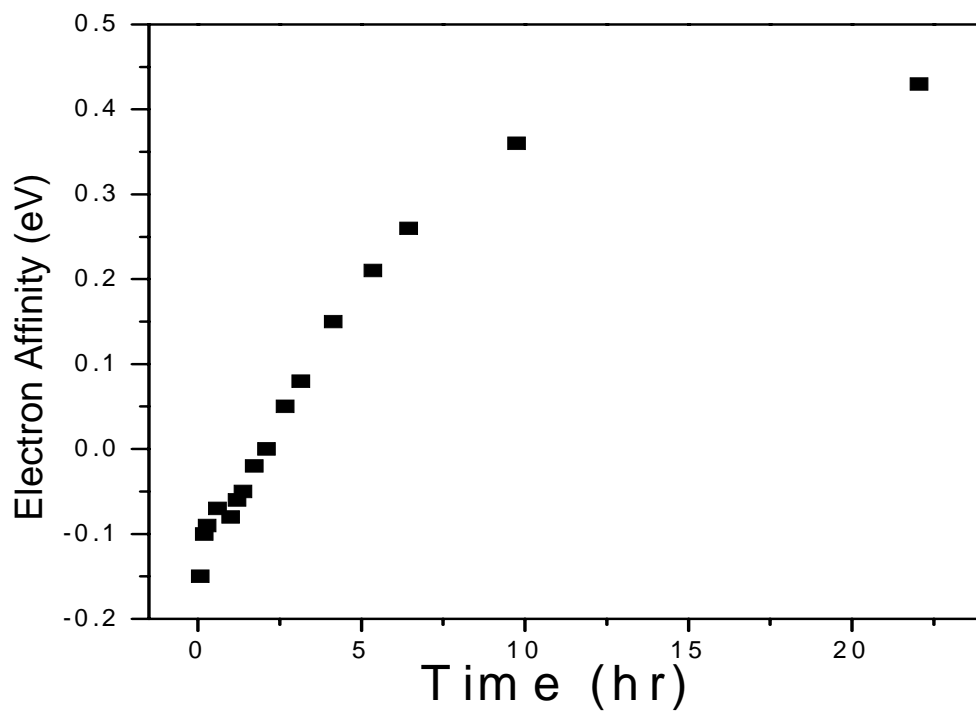


Figure 3.3 Electron Affinity (χ) at different times after activation. The electron affinity is calculated from the measured low KE cutoff of an energy distribution curve. The electron affinity at the beginning of decay is negative thus NEA.

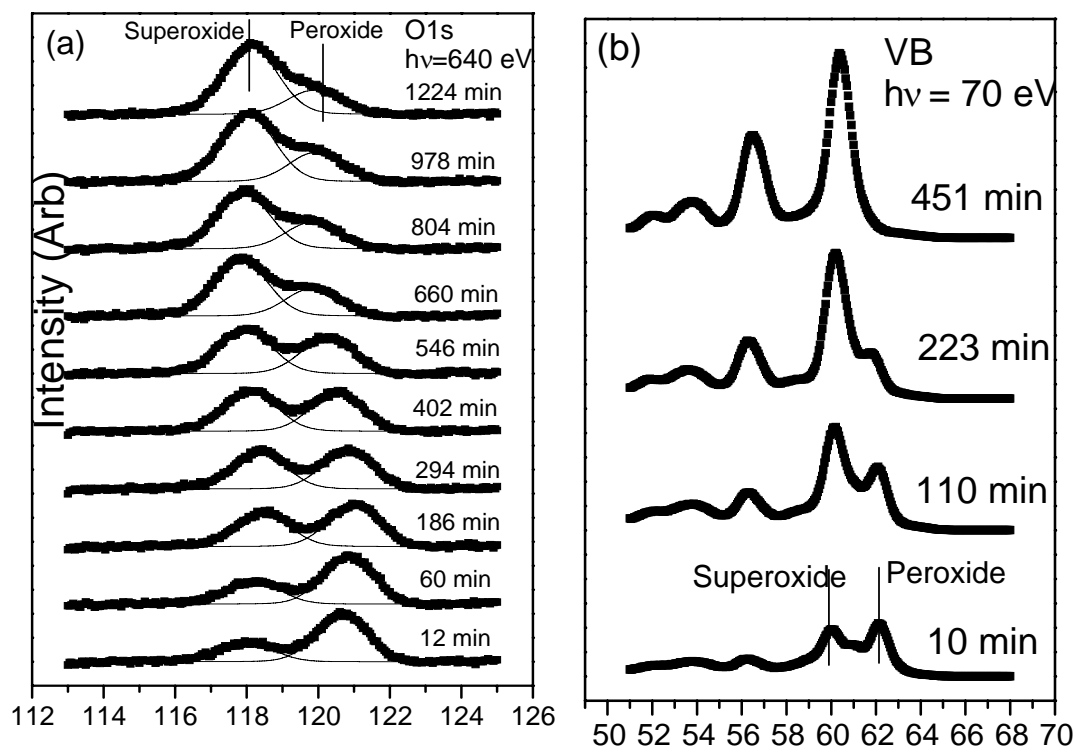


Figure 3.4 Photoemission spectra of an activated InP(100) sample at different times after activation. (a) O1s core level spectra at $h\nu = 640$ eV (b) valence band spectra at $h\nu = 70$ eV

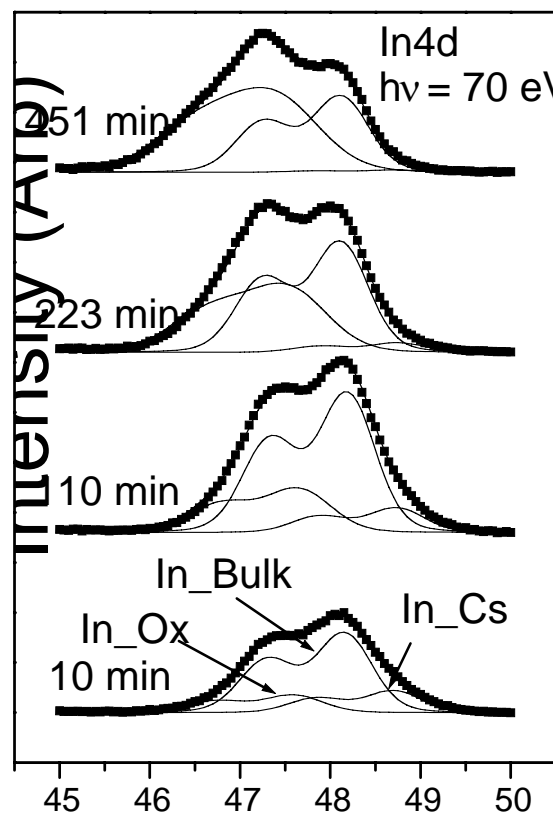


Figure 3.5 In4d core level spectra at different times after activation. In_bulk, In_Cs, and In_Ox are a bulk peak, Cs-induced peak, and oxide peak of In4d core level. They are resolved by the peak fitting of the spectra with the branching ratio of 0.667, the spin-orbit splitting of 0.86, and the lorentzian width of 0.1.

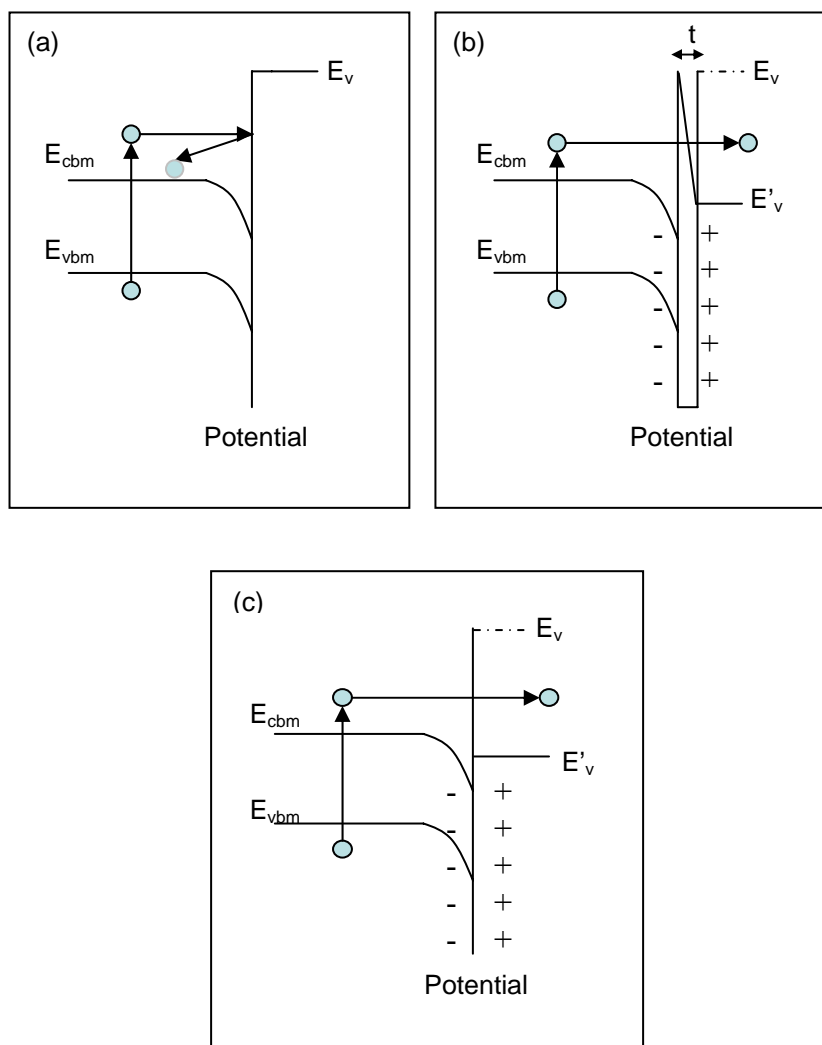


Figure 3.6 (a) Band diagram and surface potential before building up the dipoles by activation (b) Surface potential decreases in a linear way by the formation of dipoles so photoelectrons can tunnel through and escape to the vacuum (c) Simplified band diagram because of the thin Cs/O layer

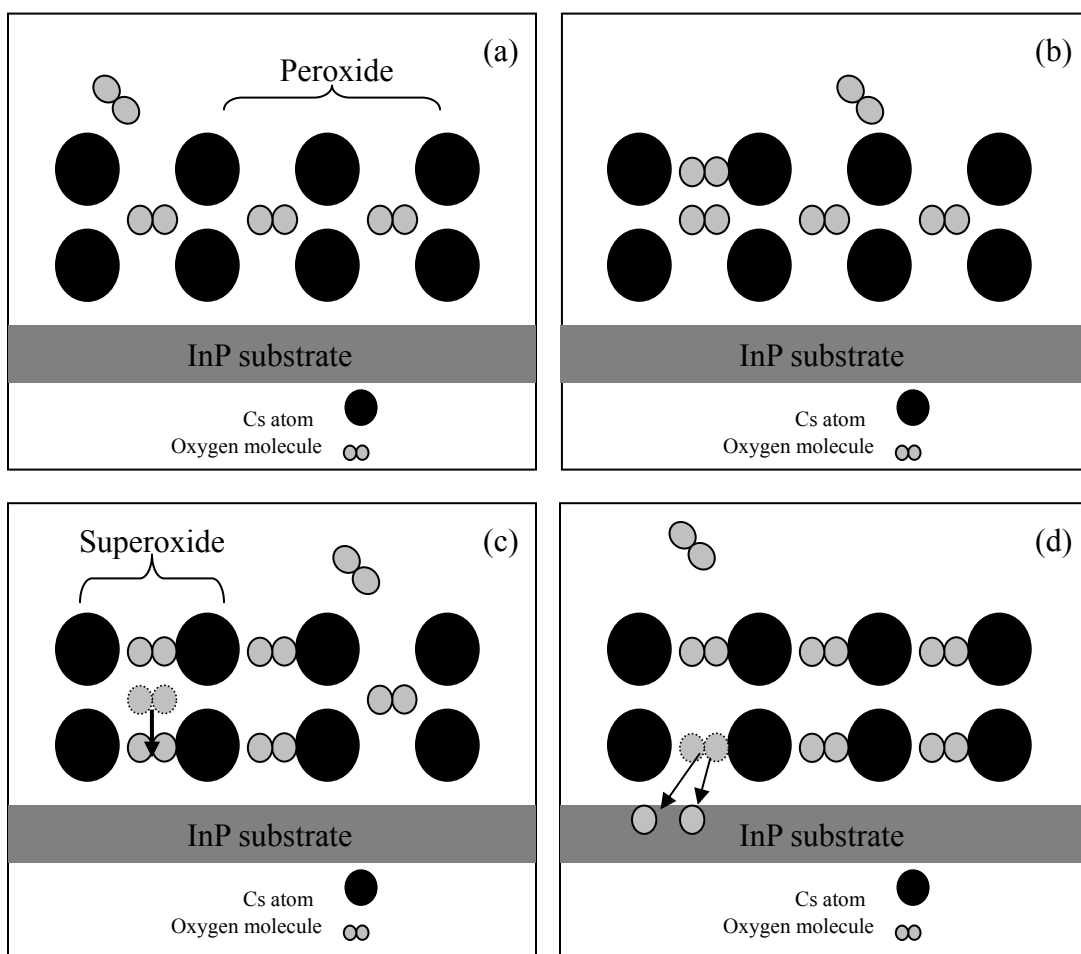


Figure 3.7 Schematic diagram of the transformation of Cs oxides in Cs/O layer based on the simplified structural model. (a) Residual oxygen molecules from a chamber approach the activation layer (b) oxygen molecules are placed on the plane of the first layer of Cs of Cs peroxide (c) the original oxygen molecules in Cs peroxide are forced down to the second layer of Cs (d) the oxygen molecules in the second layer of Cs dissociate and oxidize the InP substrate.

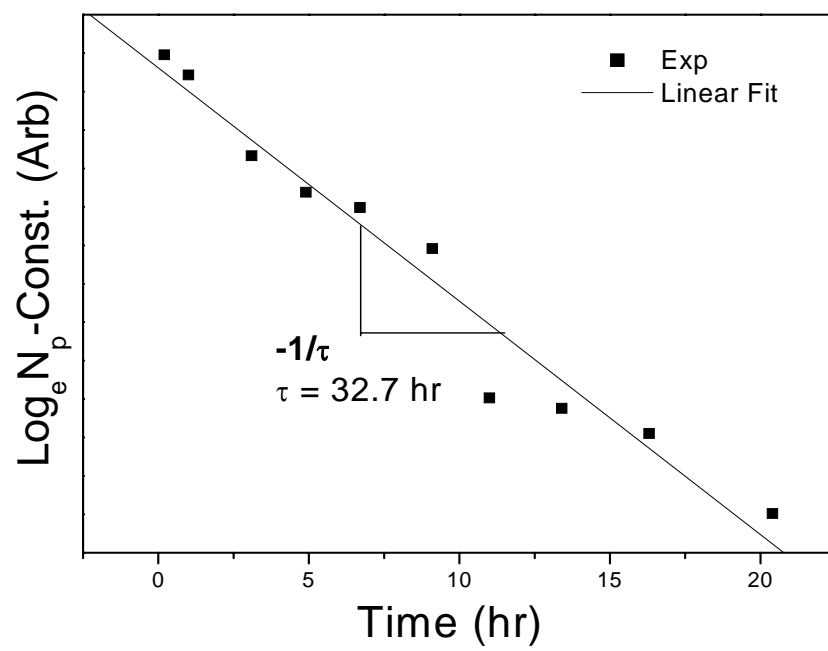


Figure 3.8 The log plot of Cs peroxide concentration vs time. Linear fitting was performed providing the time constant by taking the slope ($-1/\tau$) of a line. Time constant is found to be 32.7 hr.

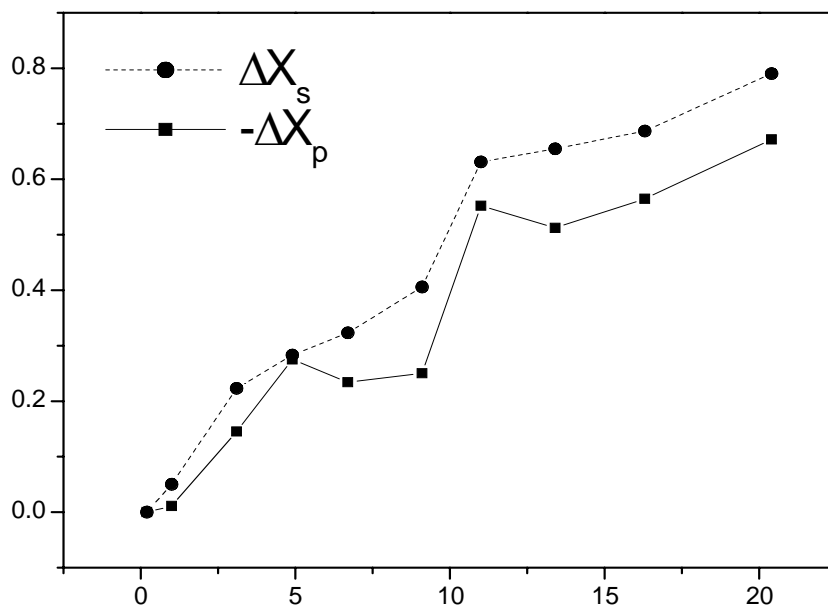


Figure 3.9 The change in the coverage of Cs superoxide (ΔX_s) and the change in the coverage of Cs peroxide (ΔX_p) were plotted as the time decay proceeds. The discrepancy between two coverage changes is due to the substrate oxide in the O1s core level spectra.

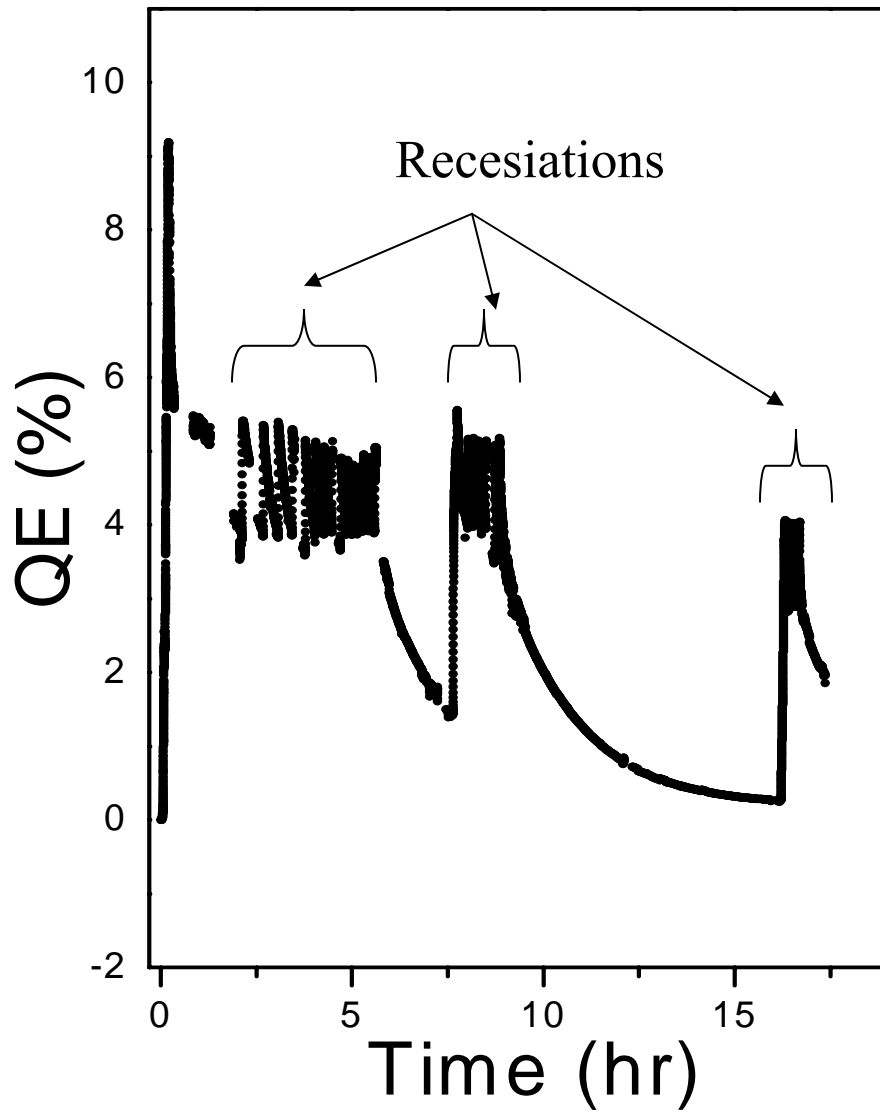


Figure 3.10 The graph of the photocurrent vs. time. Recesiations were performed during decay as indicated in the graph

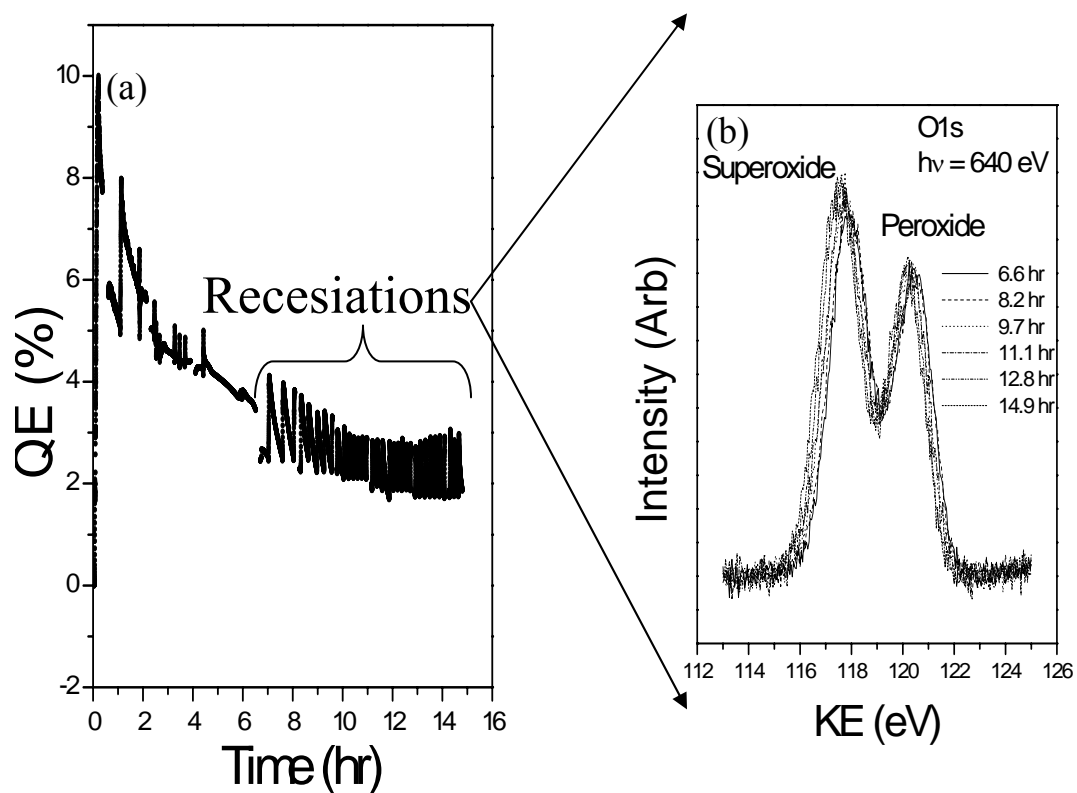


Figure 3.11 (a) The graph of the photocurrent vs. time. Recesiations were performed after 7 hours during decay as indicated in the graph, the features before 7 hours are due to the results of recesiations in the early state of decay; (b) the photoemission spectra of O1s core level during recesiations. The peroxide peak remains at the same intensity, and the superoxide peak grows slightly.

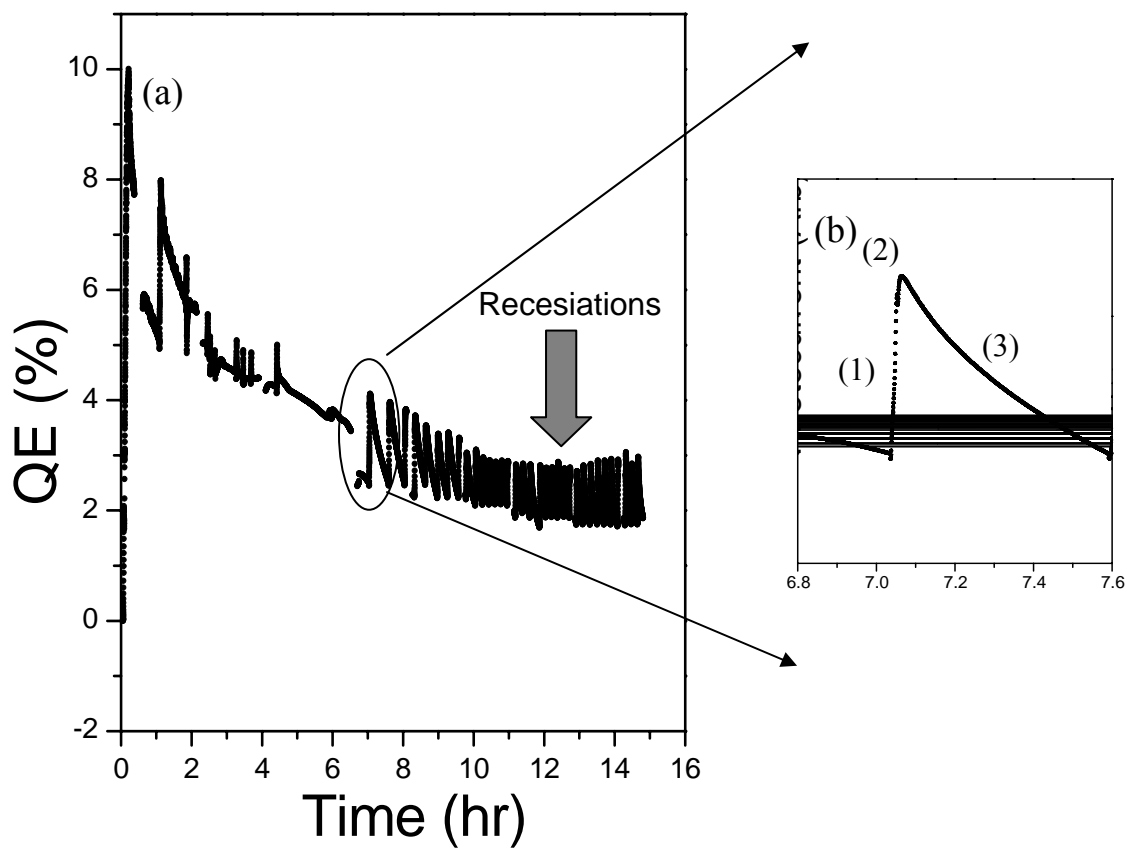
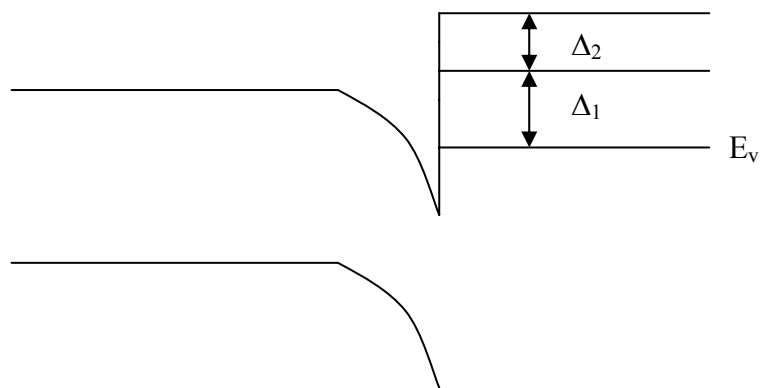


Figure 3.12 The graph of the photocurrent vs. time. (a) recesiation starts at ~7 hrs after activation, which is repeated for 8 hrs. (b) The enlarged curve of the first recesiation cycle.



E_v : Vacuum level lowered by Cs/O Activation
 Δ_1 : Vacuum level increase by substrate oxidation
 Δ_2 : Vacuum level increase by transformation of Cs oxide

Figure 3.13 The model for the increase of the vacuum level. There are two contributions. One is due to the transformation of Cs peroxide and the other is due to substrate oxidation.

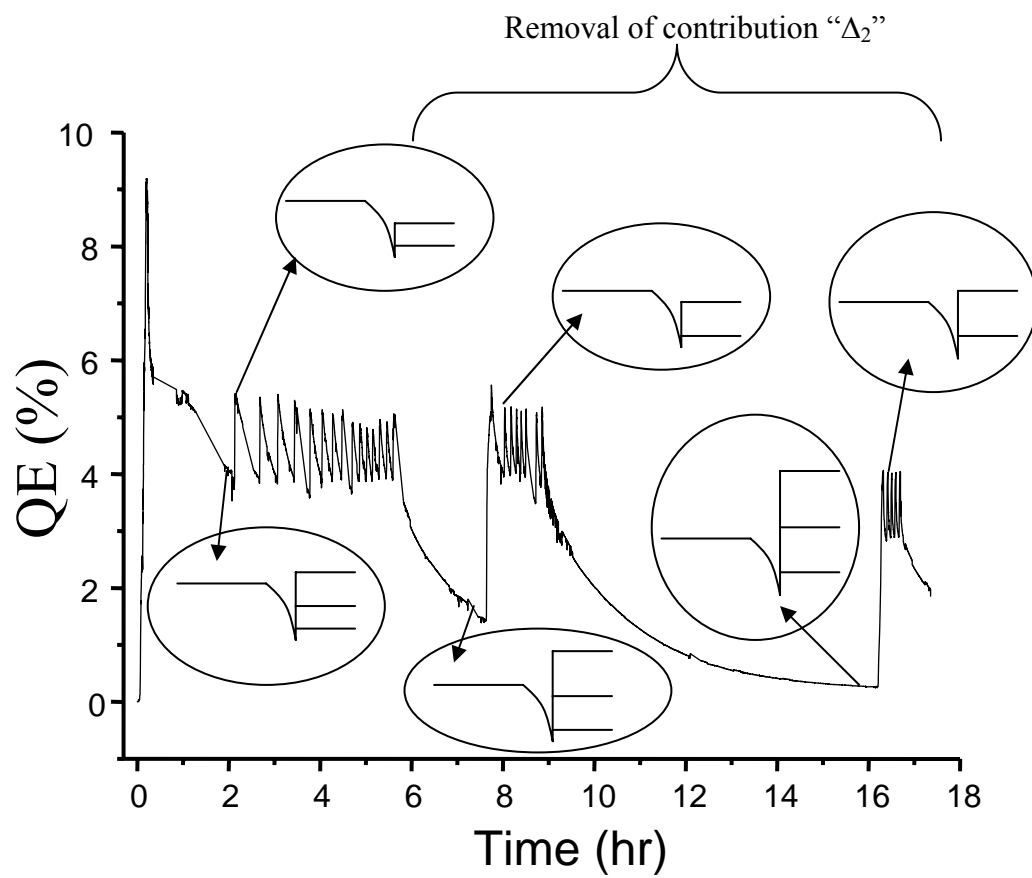


Figure 3.14 A recesiation effect on the photocurrent vs time curve is explained by the model in Figure 3.13

4. ENERGY AND ANGULAR DISTRIBUTION OF PHOTOELECTRONS FROM INP(100) PHOTOCATHODE

4.1 Introduction

InP photocathodes recently have been recognized as having important applications in near IR (infrared light) transferred electron (TE) photocathode. The TE photocathode initially was proposed and demonstrated by Bell *et al* [1]. TE photoemission is based upon the fact that, for certain III-V semiconductors, electrons can be promoted to upper conduction band valleys, with reasonable efficiency, by means of an electric field on the order of 10^4 V/cm [2]. An activated NEA surface provides us with a unique opportunity to study these properties thoroughly, since the vacuum level is lower than the bulk conduction band minimum; electron distribution outside of a solid represents the full spectrum of available electron density states, modified by the scattering and recombination of carriers. Energy distribution studies on GaAs photocathodes have been useful sources to better understand the electron scattering in, and energy losses of GaAs photocathodes [3 - 11]. However, studies on InP photocathodes are scarce, despite their arising importance in current technologies. There are a few recent energy distribution studies on InP photocathode, which are more concerned with the band structure of InP [12, 13] or with field-assisted photoemission [14, 15]. Knowledge pertaining to the scattering and energy loss properties of InP NEA (negative electron affinity) photocathodes is critical for us to understand the behavior of such photocathodes and will facilitate the development of the next generation of near-IR InP-based photocathodes and related devices.

In this chapter, we used energy distribution curve (EDC) measurements to investigate electron transport and scattering in a bulk InP, and also in a band bending region (BBR). We varied the photon energy from 1.64 eV to 2.89 eV to identify the origin of features in EDCs. We also performed angular-dependent EDC measurements on InP and GaAs to investigate the angular distribution of photoelectrons. Bias from 3.6 V to 5.2 V was applied to the sample to determine how bias affects electron distribution. The change of energy distribution during decay also was investigated.

4.2 Experiment

A P-type InP sample was prepared and activated by Cs and oxygen, as described in Chapter 2. The experimental setup for EDC measurements is illustrated in Figure 4.1. The light source was a 250 W quartz halogen lamp system with a monochromator. The lamp system (ORIEL F/0.7 Qth source, model number 66998) uses a quartz halogen lamp with maximum power of 250 W (model number 6334) and a 40 – 300 W radiometric power supply (model number 69931). During our measurements, the power level is set as 120 W.

The monochromator is an ORIEL cornerstone 130 system (model number 74047), which consists of two gratings; one is a 600 l/m, 750 nm blazing wavelength grating (model number 74027) with a wavelength region of 450 – 2000 nm and a reciprocal dispersion of 13.2 nm/mm, the other is a 600 l/m, 1600 nm blazing wavelength grating (model number 74035) with a wavelength region of 900 – 3000 nm and a reciprocal dispersion of 12.2 nm/mm. In our study, only the 750 nm blazing wavelength grating is used. The relationship between the resolution of the light and the slit size is given by

Equation 4.1. The effect of the slit size on the resolution of the EDC can be clearly seen in Figure 4.2. In order to obtain a good resolution while at the same time to keep a reasonable light intensity, a slit size 0.2 mm x 0.2 mm is chosen, which results in a resolution of 2.64 nm. This is equivalent to 13 meV at 500 nm.

$$\text{Resolution (Bandwidth)} = \text{Slit width (mm)} \times \text{Reciprocal dispersion (13.2 nm/mm)} \quad (4.1)$$

The range of photon energy was from 0.62 eV to 2.76 eV, and the intensity of the monochromatic light at every 10 nm wavelength data point was measured carefully, using a Si photodetector, as shown in Figure 4.3. In order to remove the contribution of the 2nd order light, we placed a filter in front of the monochromator output. We used the 400 nm order-sorting cut-on filter for wavelengths ranging from 400 nm to 800 nm, and used the 800 nm order-sorting cut-on filter for wavelengths larger than 800 nm. The light was focused by an optical lens and reflected by an optical mirror, so that it traveled through a viewport to the sample. The light spot was on the order of 1 cm x 1 cm, so we were not concerned with the alignment of the beam with the focal point of the electron energy analyzer, because the beam spot is much larger than the analyzer analysis area (0.5 mm diameter) used in our study.

A band diagram of the analyzer and sample, including an applied bias between the sample and an analyzer, is shown in Figure 3.2 in Chapter 3. We applied 3.6 V to 5.2 V negative bias to collect photoelectrons in our hemispherical electron energy analyzer, because, without bias, the kinetic energy of photoelectrons is too small to overcome the electric field between the sample and the analyzer with these near band-gap excitations.

The analysis area of our analyzer is set as 0.5 mm with aperture #2 and this will give a acceptance angle of $\pm 2^\circ$ (large area, small angle mode). The smallest pass energy of 0.585 eV is used giving us an instrumental resolution of 40 meV. The work function of the analyzer was predetermined by Au4f core level, as well as the Fermi edge of the Au valence band photoemission, so that we could align the EDC with the valence band maximum of the sample. All the EDC data were referenced to the bulk valence band maximum (VBM) of the sample. The EDC data of InP NEA cathodes were measured at different angles, by rotating the sample relative to the energy analyzer.

4.3 Results & Discussion

4.3.1 Identification of Photoelectron Origin

Figure 4.4 shows the yield curve of photocurrent versus photon energy. As illustrated in the graph, there is a sudden increase of photocurrent at 1.31 ± 0.04 eV, which is close to the band gap of InP, known to be 1.34 eV. Below this point, there is no photocurrent at all. The slight difference between the yield measurement and the band gap may be due to a small energy misalignment of the monochromator and the limited resolution of our system. Notice that the width of the cutoff is about 40 meV, which is slightly larger than the resolution calculated earlier (~ 13 meV). This onset of photoemission at the InP band gap clearly shows that the InP photocathode has a negative electron affinity; as long as there are electrons excited from the valence band maximum to the conduction band minimum, they can be emitted into the vacuum. For a positive electron affinity photocathode, electrons must be excited at a level higher than the vacuum level, so that the onset of photoemission will be larger than the band gap.

Figure 4.5 shows the energy distribution curve of an activated surface with a He-Ne laser as the light source (photon energy is 1.96 eV). The low energy cutoff of EDC is 1.12 +/- 0.04 eV, which is well below the conduction band minimum. This indicates that the vacuum level is also below the conduction band minimum, ensuring that the NEA condition is achieved. The existence of electrons below the conduction band minimum indicates that some electrons lose their energy via electron-phonon scattering in the band bending region [8, 11]. The length of the band bending region of the InP sample with the concentration given is calculated as 137 Å, according to Equation 4.2 [3]; $\epsilon_o\epsilon_r$ is the dielectric permittivity of the InP, and N_a (N_d) is the acceptor (donor) concentration.

$$l_D \approx \left[\frac{2\epsilon_o\epsilon_r}{(N_a - N_d)e^2} \delta V \right]^{1/2} \quad (4.2)$$

δV is the amount of band bending at the surface, calculated from the valence band maximum of our sample, the Fermi level cutoff of the Au valence band spectra, and the doping concentration ($2.3 \times 10^{18} \text{ cm}^{-3}$). The amount of $E_F - E_{\text{VBM, surface}}$ (a) in Figure 4.6 is 0.31 eV, obtained by measuring the difference between the cutoff of the Fermi edge in the Au valence band spectrum and the valence band maximum in the InP valence band spectrum, since the cutoff of the InP valence band represents $E_{\text{VBM, Surface}}$, and the Fermi edge of the Au valence band is E_F . The difference $E_F - E_{\text{VBM, bulk}}$ (b) in Figure 4.6 is the energy difference between the Fermi level and the valence band maximum, which is 0.04 eV as calculated according to Equation 4.3 [16]. E_g is the band-gap of InP, m^* is the

effective mass, and N_A and n_i are the concentrations of acceptors and intrinsic electrons, respectively.

$$E_F - E_{VBM,bulk} = 0.5E_g + 0.75kT \ln\left(\frac{m_p^*}{m_n^*}\right) - 0.026 \ln\left(\frac{N_A}{n_i}\right) \quad (4.3)$$

Since the band bending is $E_{VBM,bulk} - E_{VBM,surface}$, it is calculated as 0.27 eV in accordance with Equation 4.4.

$$E_{VBM,bulk} - E_{VBM,surface} = (E_F - E_{VBM,surface}) - (E_F - E_{VBM,bulk}) = (a) - (b) \quad (4.4)$$

Figure 4.7 shows the energy distribution curve taken at 2.05 eV (photon energy) with the ORIEL halogen lamp and monochromator. A 4 V bias between the sample and the analyzer is applied; later, we will prove that the bias affects the EDC measurement. The low kinetic energy (KE) cutoff is below the bulk conduction band minimum, which means that the photocathode is NEA. There are two distinct peaks in EDC: Peak A at 1.4 eV and Peak B at 1.8 eV. The relative intensities of Peaks A and B change with different photon energies, as shown in Figure 4.8. It is known that, when $h\nu$ is varied, the EDCs are continuously modified, and the evolution of each structure permits its identification relative to the band structure [6, 10, 12, 17]. In the experiment in Figure 4.8, $h\nu$ is changed from 1.76 eV to 2.73 eV. There is only one peak (A) approximately at 1.5 eV kinetic energy when photon energy is low (1.76 eV). The higher kinetic energy shoulder (Peak B) at around KE of 1.9 eV is distinguishable at a higher level of photon energy

(1.89 eV) and dominant at even higher levels. The explanation for this peak evolution relative to energy distribution is shown in Figure 4.9, which depicts the electronic band structure of InP. For photon energies below 1.9 eV, the excitation-escape process is illustrated by the arrow labeled (A) in Figure 4.9. The electrons are excited to the region of the Γ valley and thermalized in that minimum, giving rise to Peak A of emitted electrons. At photon energies above 1.9 eV, however, an additional process (marked (B) in the Figure 4.9) can occur. Through this process, the electron is again excited into the Γ valley but then scatters into the vicinity of the L valley where it is thermalized; Peak B results from this accumulation of electrons. Electrons will scatter into and be thermalized in the L conduction band valley rather than bouncing back to the Γ valley, due to the larger density of states in the L valley and the value of the coupling coefficient between the two valleys [10]. These inter-valley scatterings are caused by polar optical phonons, which are the predominant scatterings of II-VI and III-V compound semiconductors, including InP at room temperature [18]. For these crystals, the motion of negatively and positively charged atoms in a unit cell will produce an oscillating dipole; the vibration mode is called a *polar optical-mode phonon*. The density of states is expressed in Equation 4.5. The effective mass is inversely proportional to the curvature of the density of states, as shown in Equation 4.6. The curvatures near the bottom of the higher conduction valleys (L, X valley) are smaller than that of the Γ valley, leading to a higher effective mass that results in the larger density of states in the L and X conduction band valley.

$$g_c(E) = \frac{m_n^* \sqrt{2m_n^* (E - E_c)}}{\pi^2 \hbar^3} \quad (4.5)$$

$$m^* = \hbar^2 \left(\frac{d^2 E}{dk^2} \right)^{-1} \quad (4.6)$$

In Figure 4.9, the difference between Γ valley minimum and L valley minimum is 0.59 eV, but in our EDC measurement, the peak difference is about 0.4 eV \sim 0.5 eV. We must not mistake the Peak A position as the position of the Γ valley minimum; this is simply due to Γ valley electron distributions being cut by the vacuum level. The real Γ valley peak position, without the vacuum level cutoff, should be observed at a lower energy. In addition, the position of the L valley peak is about 1.7 eV \sim 1.8 eV, not 1.9 eV as expected from the band diagram, because L valley electrons can also lose energy from electron-phonon scattering in the band bending region.

Theoretically, some electrons can transfer into the X valley for photon energies higher than 2.2 eV. Electrons in the X valley, however, tend to relax to the lower energy L valley due to the large coupling coefficient [19, 20]. This is why we do not observe X valley-related features even when the photon energy is high enough. X valley features were not observed in earlier GaAs studies either.

4.3.2 Angular Distribution of Photoelectrons with Room Light

Before examining the angular dependence of the photoelectrons using our monochromatic light source, we measured angle-dependent energy distribution curves (ADEDCs) with room light as the light source. In our angular dependent study, the system setup only allowed us to rotate our sample while both the analyzer and the light source remained stationary; this resulted in different illuminations of the sample so that

the intensity of the photoelectrons was difficult to normalize. However, room light through all of the viewports of our vacuum chamber provided a relatively homogeneous illumination of the sample at different angles. Therefore, this study provides preliminary information about the angular dependence of the photoelectrons.

Figure 4.10 shows the EDCs at different off-normal angles clockwise (4.10a) and anticlockwise (4.10b). Both the intensity and the low energy cutoff changed according to the angle. For this particular experiment, the InP does not achieve NEA, so the vacuum level is actually above the bulk conduction band minimum. To overcome the energy barrier caused by the vacuum level, the electrons not only must have a total energy higher than the vacuum level but, more specifically, an energy component perpendicular to the surface higher than the vacuum level. Therefore, electrons with off-normal angle emission must have total energies higher than electrons emitted at a normal emission angle, since their energy component parallel to the surface will not help. This results in a higher low energy cutoff for the EDC at off-normal angle emission.

Figure 4.11 plots the intensity and low energy cutoff against an off-normal angle. The angular spread is not as narrow as the GaAs photocathode reported by Zhi Liu [21], who observed emission with a 15° angle. This is because we do not have NEA here, so most of the electrons are from the L valley, which has a larger angular spread due to its larger effective mass; this will be discussed later in more detail. Because Liu had a good NEA surface, most of the electrons were from the Γ valley, which led to a narrow angular spread.

As shown in Figure 4.11, the low energy cutoff and intensity of EDCs at different off-normal angles were not symmetrical at 0° . This experiment was repeated several

times with similar results, and the average center of the low energy cutoff and the intensity was about $15^\circ \pm 5^\circ$. This might have resulted from the deflection of the electron path due to the magnetic field in the surroundings. We will now examine the Earth's magnetic force to find out what potential effects it may have had on the photoelectrons.

According to Faraday's law, shown in Equation 4.7, if we use the maximum magnetic field on the Earth's surface (0.6 gauss) and assume that the field is perpendicular to the velocity, then the magnetic force acting upon photoelectrons with a kinetic energy of 5 eV traveling from the sample to the analyzer is $\sim 9.6 \times 10^{-18}$ N.

$$\mathbf{F} = q\mathbf{v} \times \mathbf{B} \quad (4.7)$$

Since we know the mass of an electron (9.11×10^{-31} Kg) and Newton's law ($F = m \times a$), we can estimate the acceleration rate as 1.1×10^{13} (N/Kg). Note that this acceleration changes with the velocity of the electron in the magnetic field; to simplify we can assume that the velocity does not change much, so the acceleration remains constant. Later, we will check to see if this assumption is correct. First, however, the time that it takes for the electrons to travel from the sample to the analyzer must be identified. Because we know the initial velocity of the electrons from Equation 4.8 and the distance between the sample and analyzer is roughly 0.019 m, then assuming that the velocity does not change significantly, we can obtain the approximate traveling time from Equation 4.9.

$$v = \sqrt{\frac{2E_k}{m}} \quad (4.8)$$

$$t = d / v \quad (4.9)$$

Knowing the traveling time and acceleration rate, the distance of each electron's deflection is estimated to be 0.2 cm. This gives us about a 10° deflection of photoelectrons with kinetic energy of 5 eV. Thus, the assumption that the velocity does not change significantly is valid in our rough approximation. This amount of deflection is based upon the assumption of the Earth's maximum magnetic force. Under our experimental conditions, the actual magnetic force could be less than this maximum value, and the direction of velocity is not necessarily perpendicular to the magnetic field. To make things more complicated, other magnets (ion pumps, cold cathode gauges, and SSRL SPEAR ring) may contribute to the magnetic force exerted on the photoelectrons. This estimated deflection, however, is on the same order of magnitude with the center angle of lower energy cutoff and intensity of the EDC measurements using room light. The similar off-center behavior is also observed in the EDC measurements with scattered laser light and the center also averaged about 15° .

It is interesting to note that the deflection $y=0.5at^2$ is inversely proportional to the velocity v . Thus, for high energy photoelectrons like in our normal core level studies, this deflection is so small that it can be ignored. However, for electrons with very small energies, the surrounding fields will have a large effect. For a more detailed study of angular dependent EDC measurements using monochromatic light, which will be discussed in the following sections, each angle is shifted by 15° to compensate for this deflection.

4.3.3 Angular Distribution of Photoelectrons using Monochromatic Light

Figure 4.12 shows the AEDC of an InP photocathode. The total intensity of photoelectrons decreases when we rotate the sample away from the normal position to the analyzer. However, we must be very careful to interpret this as a narrow angular spread. Due to the limitation of our system, we can only rotate the sample to change the illumination because our light source is stationary; this changes the photoelectron intensity aside from the real angular spread. Nevertheless, there is a relative change between the Γ valley electrons and the L valley electrons that is not affected by the change of illumination on the sample. The higher KE side peak (L valley) decreases more slowly at larger off-normal angles than the lower KE side peak (Γ valley), as shown in Figure 4.12. This is evidence that Peak B results from the transfer of electrons with a heavier effective mass to the L valley and that Peak A results from the thermalized electrons in the Γ valley. Zhi Liu (2005) constructs a model to relate the number of electrons ($n(\theta)$) at a certain emission angle (θ) to electron effective mass (m^*), free electron mass, (m_0) and other parameters, as shown in Equation 4.10 [21].

$$n(\theta) = C \cos \theta \left((2E_A / kT_{eff}) \left(1 - \frac{m_0}{m^*} \sin^2 \theta \right)^{-3/2} + \left(1 - \frac{m_0}{m^*} \sin^2 \theta \right)^{-1/2} \right) \times \exp \left(- \frac{E_A}{kT_{eff}} \cdot \frac{\frac{m_0}{m^*} \sin^2 \theta}{1 - \frac{m_0}{m^*} \sin^2 \theta} \right) \quad (4.10)$$

To better understand this equation, we must recall the two selection rules for electrons to escape from semiconductors: the preservation of momentum parallel to the surface and the preservation of total energy. If we designate $E_{//}$ as the energy component parallel to the surface and $p_{//}$ as the parallel momentum, then we have $E_{//}(\text{solid}) = p_{//}^2 / 2m^*$

and $E_{//}(\text{vacuum}) = p_{//}^2 / 2m_0$. Since $m^* < m_0$, we have $E_{//}(\text{solid}) > E_{//}(\text{vacuum})$. However, we must preserve the total energy, meaning that part of the energy component parallel to the surface must be transferred to the energy component perpendicular to the surface; this is the so-called “focusing effect.” The smaller the effective mass m^* is, the larger the focusing effect and therefore the narrower the angular spread. The maximum emission angle can be determined by this boundary condition; the electron does not have any perpendicular momentum inside of a solid. Once electron is omitted, it will gain a perpendicular energy component by $E_{\text{total}} \times (m_0 - m^*) / m_0$, leading to the emission angle as $\sin^{-1}(m^* / m_0)^{0.5}$. This is the same as the maximum emission angle obtained from Equation 4.10.

According to Equation 4.10, the photoelectron intensity reaches 0 at the maximum emission angle, where $(m_0 / m^*) \sin^2 \theta$ is equal to 1. Therefore, the maximum emission angle is expressed as Equation 4.11, which means that a larger effective mass leads to a larger angular spread of photoelectrons, since the maximum emission angle is large. This is consistent with the behavior of Peaks A and B in our ADEDCs. Peak B from the L conduction band valley, which has the larger effective mass ($0.25m_0$), has a larger emission angle than Peak A, caused by the Γ thermalized electrons ($0.062m_0$).

$$\theta_{\text{max}} = \sin^{-1}(m^* / m_0)^{0.5} \quad (4.11)$$

The angular dependence of Peaks A and B is presented more clearly in the angle-dependent energy distribution curves of GaAs photocathodes (shown in Figure 4.13), which have a band structure similar to that of InP. The difference between GaAs EDCs

and the InP EDC curves is the smaller degree of peak separation between A and B, since the energy gap between the Γ conduction band valley minimum and the L conduction band valley minimum is smaller with the GaAs (0.29 eV) band structure than with InP (0.59 eV).

4.3.4 Energy Distribution at Different Biases

Figure 4.14 shows EDCs at different biases. When the bias increases, Peak B increases. This is reasonable because the effective acceptance angle of the analyzer becomes larger with a larger bias so that it can collect more L valley electrons (Peak B), having a larger angular distribution [21 – 23]. We can discuss this effect with some simple approximations in which there is no bias and the acceptance angle is 2° ; the transverse energy of photoelectrons collected by the analyzer is approximated in Equation 4.12. When the bias is applied, the photoelectrons collected by the analyzer should satisfy Equation 4.13 so as to be collected by the analyzer.

$$E_{\perp} \leq E \sin^2(2^\circ) \quad (4.12)$$

$$E_{\perp} \leq (E + V) \sin^2(2^\circ) \quad (4.13)$$

If θ is the effective acceptance angle after applying the bias, then the new equations (4.14 and 4.15) should hold true to the bias and to the effective acceptance angle.

$$E \sin^2 \theta \leq (E + V) \sin^2(2^\circ) \quad (4.14)$$

$$\sin \theta \leq \sqrt{\frac{E + V}{E}} \sin^2(2^\circ) \quad (4.15)$$

When kinetic energy E is extremely close to 0, then the condition will be satisfied automatically so that electrons from all solid angles will be collected. However, if kinetic energy E is larger than $V\sin(2^\circ)$, then the effective acceptance angle should hold to Equation 4.16.

$$\theta \leq \sin^{-1}\left(\sqrt{\frac{E + V}{E}} \sin(2^\circ)\right) \quad (4.16)$$

Figure 4.15 shows the effective angle and the kinetic energy plot at each bias, in accordance with Equation 4.15. There is not a mathematically accurate description of the modification of acceptance angle by sample bias because of the simplicity of our approximation and the assumptions made. The purpose of this plot is to help us to qualitatively understand the effect of the bias on the effective acceptance angle. The acceptance angle increases with the bias at a fixed level of kinetic energy, as expected from the previous argument. The shape of EDC is modified by the applied bias.

Although some factors such as peak position are not significantly affected, we must be careful to quantitatively analyze the EDC data. In Figure 4.14, the intensity of Peak A slightly increases with the bias, much less than with Peak B; it saturates quickly at around 4.2 V due to the small energy and angular spread of the Γ valley electrons. First, for lower energy electrons, the effective acceptance angle is larger than that of high energy

electrons with the same bias. Second, due to the small angular spread, even when there is a small bias, few additional Γ valley electrons are gained from applying a higher bias.

4.3.5 Inter-Valley Scattering in the Band Bending Region

Recall from Figure 4.8 that when the photon energy is 1.89 eV, which is barely enough for the electrons to move into the L valley, a peak already begins to form. This suggests that electrons can be promoted into the L valley in the band bending region. Energetic electrons in the Γ valley excited with 1.89 eV photons do not have enough energy to be scattered into the L valley in the bulk region. However, in the band bending region, these electrons will be accelerated by the electric field caused by the band bending, allowing them to gain more energy. The maximum energy gained equals the magnitude of the band bending, which is 0.27 eV in our study. As a result, they will have enough energy to be scattered into the L valley.

Another experiment supports this inter-valley scattering in the band bending region. Figure 4.16 shows the EDC of the InP photocathode excited by 1.64 eV light with different bias. There is only one peak (A), due to the thermalized electrons in the Γ valley with biases of 4 V and 4.2 V. Peak B, however, starts to appear and grow when we apply higher bias, as shown in the same figure. This should result from electrons scattered to the L valley in the band bending region in the high electric field. As previously discussed, a larger bias will integrate a more solid angle so that the L valley electrons, with a larger angular spread, will have increased intensity in the EDC. In the ECD, the L valley peak becomes prominent when a higher bias is applied.

It is difficult to explain why the high energy cutoff appears to be about 1.85 eV with biases of 4.8 V and 5.2 V. There are several possible reasons. (i) There might be some higher energy photons from the monochromator, although our resolution (~ 13 meV) should result in a much smaller difference (~ 0.2 eV). (ii) There may be some leaked room light if all of the viewports were not blocked properly; however, this is unlikely since the EDC without the light source does not have a very high background intensity. (iii) Electrons scattered into the L valley can actually gain energy when thermalized there. (iv) Our system resolution may have some contribution. (v) There may be some effects of the bias on the EDC that we still do not understand. Nevertheless, even this 1.85 eV high energy cutoff is still lower than the L valley position in the bulk. Therefore, the only explanation is that the L valley electrons are scattered into the band bending region.

4.3.6 Energy Distribution after QE Decay

Figure 4.17(a) shows the EDCs with 2.05 eV excitation at two different times after the completion of activation. One set of data was taken at 20 minutes and the other at 5 hours. As expected from Chapter 3, the low energy cutoff moves to the higher KE side due to the rise in the vacuum level. The vacuum level increases from 1.30 eV to 1.54 eV after the 5-hour decay. At the same time, Peak B moves to the higher KE side as the decay proceeds (about 0.1 eV as shown in Figure 4.17b). We believe that this is due to the change in band bending caused by the oxidation of the substrate, which can be measured from the shift of core level spectra. The decreased number of photoelectrons caused by time decay is more dramatic at lower photon energies (2.05 eV, see Figure 4.17a) than at higher photon energies (2.46 eV, see Figure 4.17b). This is due to the fact

that the increased vacuum level at this stage mainly affects the thermalized Γ electrons rather than the electrons transferred to the L conduction band valley.

In summary, the angular spread of InP (and GaAs) photocathodes depends upon the level of photon energy for the excitation of photoelectrons. When $h\nu$ is slightly higher than the band-gap, most of the emitted electrons will be thermalized electrons in the Γ valley; consequently, the angular spread is small because of the small effective mass of Γ valley electrons. However, when the level of photon energy is large enough, most of the electrons will be transferred to the L valley; hence, the angular spread will be larger because the electron effective mass is larger. A larger photon energy is necessary to obtain a higher QE from the photocathode. Electron beam properties like angular distribution and energy distribution, however, will become worse with higher levels of photon energy or larger bias, because L valley electrons have a greater angular spread than Γ valley electrons and the total spectrum width is larger. As a result, poor resolution for imaging devices and poor emission for electron sources built on such photocathodes are expected with higher energy photon illumination.

Now we must revisit the significance of Negative Electron Affinity (NEA). Recall that NEA will enable a photocathode to have higher quantum efficiency. In addition, NEA enables us to access highly directional Γ valley electrons. Without NEA, we still obtain a QE, although it is smaller but on the same order of magnitude. However, with a positive electron affinity, most of the electrons are from the L valley, which has a much larger angular spread; this is undesirable for many applications. Therefore, the difference of QE is only quantitative, but the ability to access Γ valley electrons makes a significant

qualitative difference. Furthermore, only with a NEA photocathode is the investigation of the electron transport and scattering in the lowest conduction band valley possible.

This study also reveals that it is more difficult to activate InP than GaAs as a NEA photocathode, and the lifetime is harder to maintain. InP has an intrinsic advantage over GaAs: larger energy separation between Γ valley and L valley electrons. The difference between Γ valley and L valley for GaAs is only 0.29 eV. With the electron energy loss in the band bending region, Γ valley electrons and L valley electrons are further mixed in terms of their kinetic energy. For InP, however, the difference is 0.59 eV, making it easier to select only Γ valley electrons instead of L valley electrons, which have a larger angular spread.

4.4 Conclusions

We investigated the electron energy distributions of InP photocathodes via energy distribution curve measurements. We verified that we had obtained a negative electron affinity InP photocathode, by examining the cutoffs of a yield curve and an energy distribution curve. We also found that there are two types of photoelectrons escaping to the vacuum; one is the electron in the Γ conduction band valley minimum, and the other type of electron is a photoelectron, transferred to the L conduction band valley by polar optical phonon scatterings. We observed that the L valley is populated for both InP and GaAs photocathodes as photon energy increases, which can be explained by larger energy density of the states, which, in turn, is caused by the larger effective mass in the higher valley. The angle-dependent energy distribution of InP photocathodes also was studied. Angular distribution was highly directional, and the transferred electrons in the L valley exhibit larger angular spread than the Γ valley electrons, due to their larger

effective mass. Larger bias between the sample and the analyzer leads to an increase in the effective acceptance angle of the electron energy analyzer, and the electrons in L valley become more dominant in EDCs with larger bias. The lower energy cutoff of EDC during decay moves to the higher KE side, which means the vacuum level increase during decay. The direct result of this is the decrease and disappearance of Γ valley electron emissions and the photoelectrons from such positive electron affinity cathodes are mostly L valley electrons with a larger angular spread.

4.5 References

- ¹ R. L. Bell, L. W. James, R. L. Moon, APL, **25**, 645 (1974)
- ² S. M. Sze, *Physics of Semiconductor Devices*, Willey, New York, 743 (1969)
- ³ H.-J. Drouhin, C. Hermann, G. Lampel, Phys. Rev. B, **31**, 3859 (1985)
- ⁴ Z. Liu, F. Machuca, P. Pianetta, W. E. Spicer, R. F. W. Pease, Appl. Phys. Lett., **85**, 1541 (2004)
- ⁵ A. W. Baum, W. E. Spicer, R. F. W. Pease, K. A. Costello, V. W. Aebi, SPIE. Vol. **2550**, 189 (1995)
- ⁶ R. C. Eden, J. L. Moll, W. E. Spicer, Phys. Rev. Lett., **18**, 597 (1967)
- ⁷ C. A. Sanford, N. C. MacDonald, J. Vac. Sci. Technol. B, **8**, 1853 (1990)
- ⁸ H.-J Drouhin, C. Hermann, G. Lampel, Phys. Rev. B, **31**, 3872 (1985)
- ⁹ L. W. James, R. C. Eden, J. L. Moll, W. E. Spicer, Phys. Rev., **174**, 909 (1968)
- ¹⁰ L. W. James, J. L. Moll, Phys. Rev., **183**, 740 (1969)
- ¹¹ A. L. Musatov, V. L. Korotkikh, V. D. Shadin, Sov. Phys. Solid. State, **23**, 540 (1981)
- ¹² L. W. James, J. P. Van Dyke, F. Herman, D. M. Chang, **1**, 3998 (1970)
- ¹³ J. Peretti, H. -J. Drouhin, D. Paget, Phys. Rev. B, **44**, 7999 (1991)
- ¹⁴ J. Peretti, H. -J. Drouhin, D. Paget, Phys. Rev. Lett., **64**, 1682 (1990)
- ¹⁵ J. Peretti, H. -J. Drouhin, D. Paget, Phys. Rev. B, **47**, 3603 (1993)
- ¹⁶ R. F. Pierret, *Semiconductor Device Fundamentals*, Prentice Hall, New Jersey (1995)
- ¹⁷ W. E. Spicer, R. D. Eden, in *Proceedings of the 9th International Conference on the Physics of Semiconductors*, Moscow (1968), edited by S. M. Ryvkin (Nauka, Leningrad, 1968), p65
- ¹⁸ S. S. Li, *Semiconductor Physical Electronics*, Springer, New York (1993)
- ¹⁹ C. Hilsum, H. D. Rees, Electron. Letter., **6**, 277 (1970)

- ²⁰ H. D. Rees, C. Hilsum, *Electron. Letter.*, **7**, 437 (1971)
- ²¹ Z. Liu, Y. Sun, P. Pianetta, R. F. W. Pease, *JVST B*, **23**, 2758 (2005)
- ²² J. H. Pollard, *Proceedings of the 2nd European Electro-Optics Markets and Technology Conference*, 316 (1974)
- ²³ C. A. Sanford, N. C. MacDonald, *J. Vac. Sci. Technol. B*, **6**, 1863 (1990)

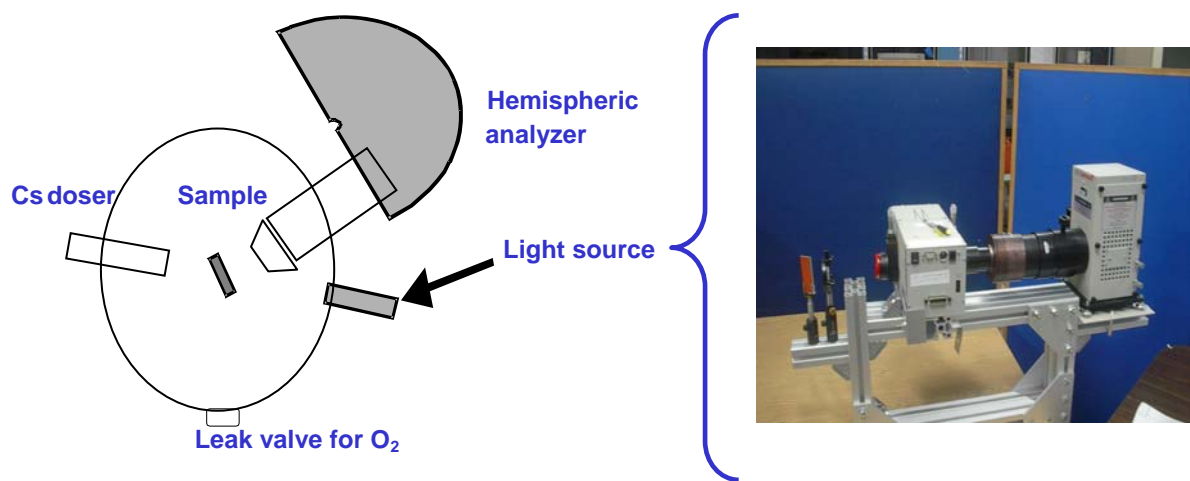


Figure 4.1 Experimental setup for the energy distribution curve measurements

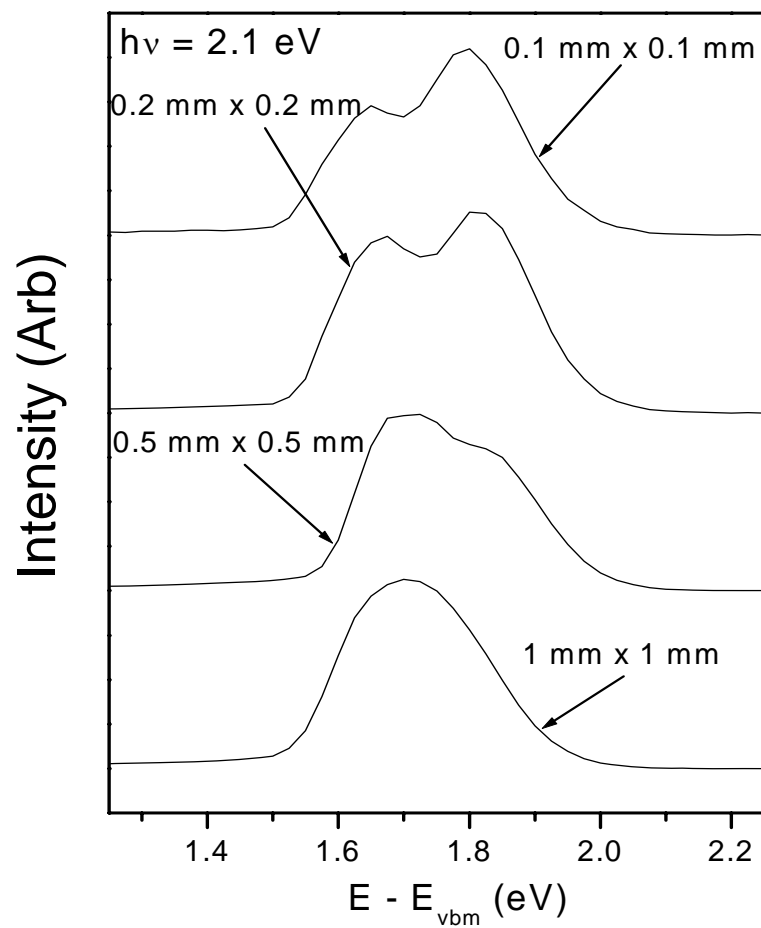


Figure 4.2 EDCs of a InP photocathode taken at $h\nu = 2.1$ eV with different slit sizes. The intensities are normalized to the same height. Without normalization, the intensity of larger slit size is much higher than the intensity of smaller slit size.

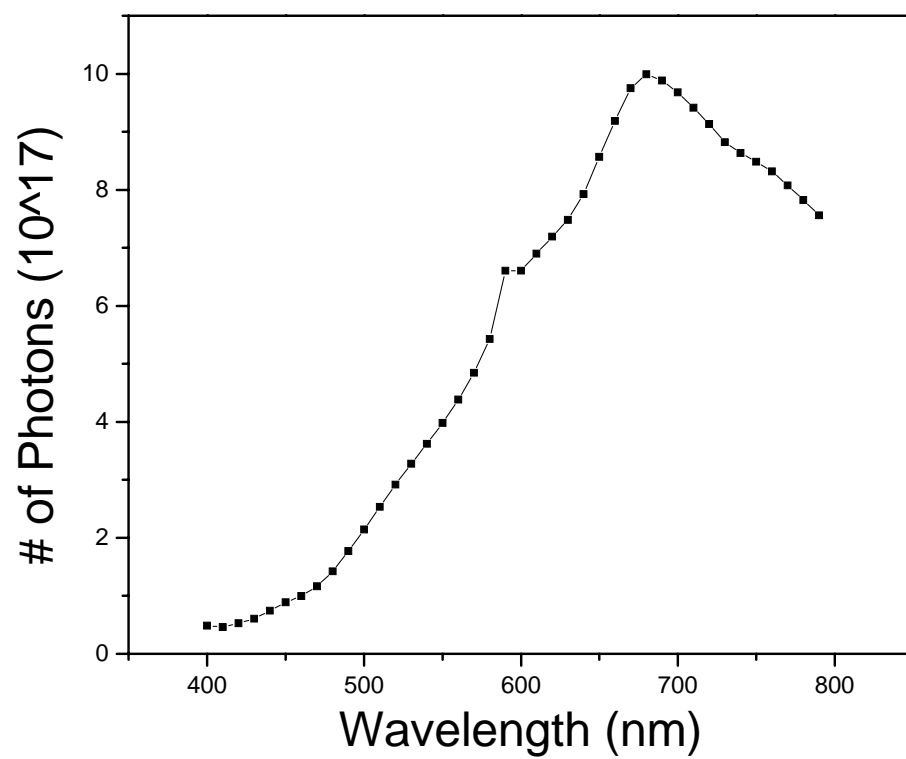


Figure 4.3 Calibration of the number of photons at each wavelength for the 600 l/mm, 750 nm blazing wavelength grating.

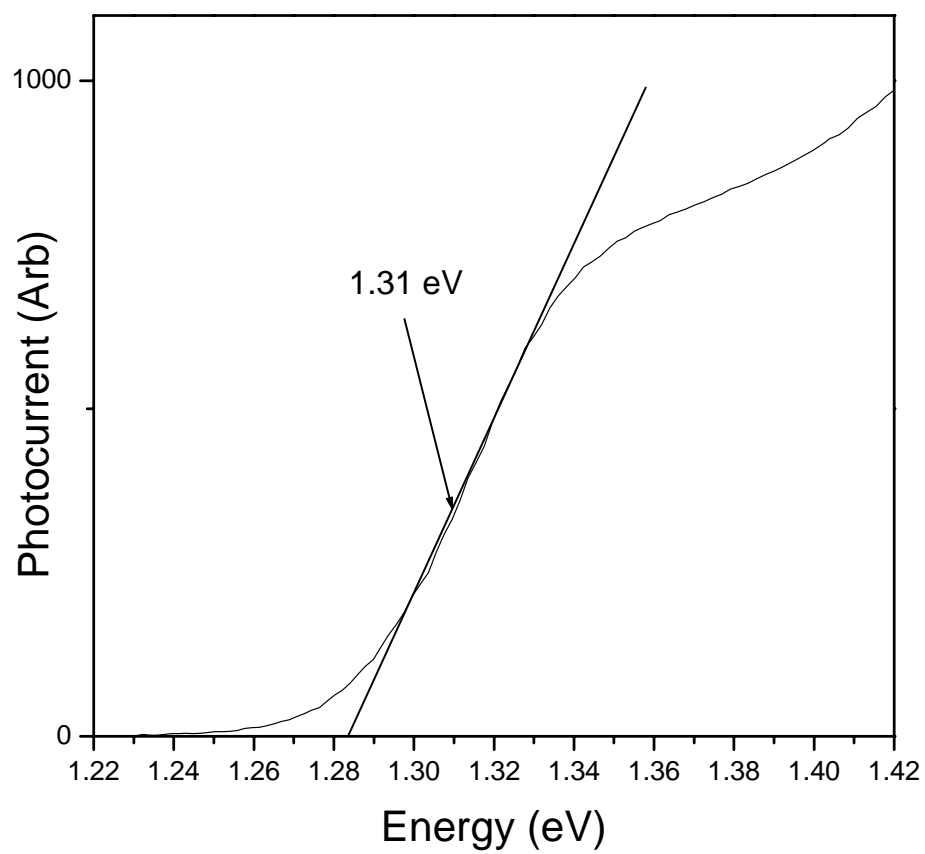


Figure 4.4 Photocurrent vs photon energy curve, normally called “Yield Curve”.

Photocurrent was obtained by measuring the drain current of sample.

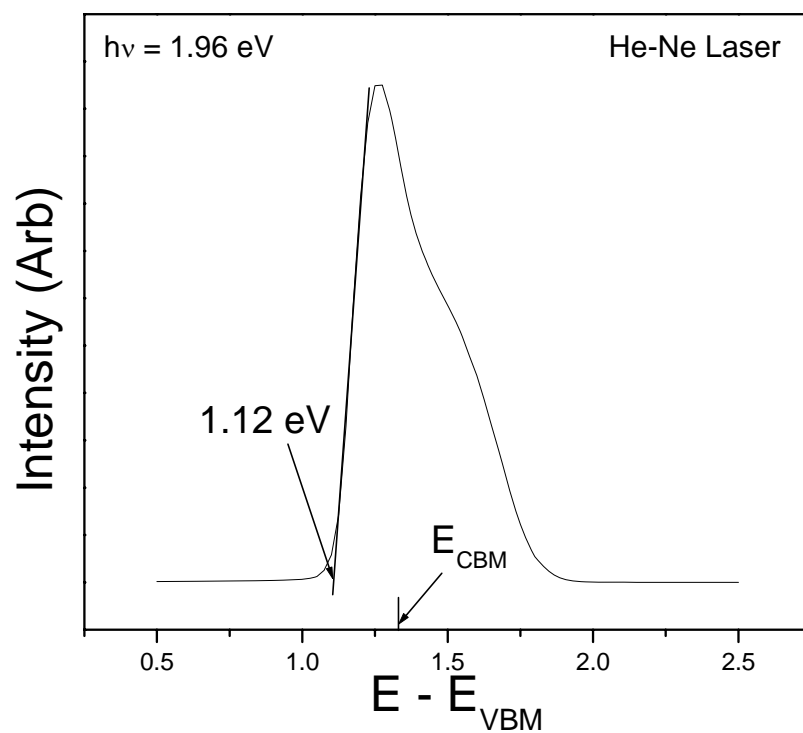


Figure 4.5 Energy distribution curve of InP photocathode at 1.96 eV photon energy by He-Ne Laser.

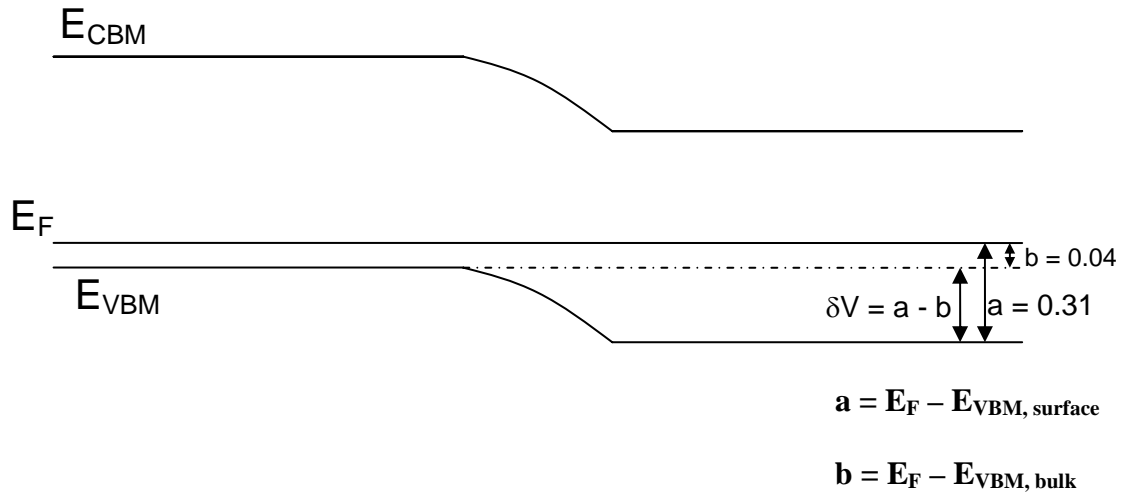


Figure 4.6 Band diagram with a surface band bending. The amount of the band bending is the subtraction of $E_F - E_{VBM, \text{bulk}}$ (b) from $E_F - E_{VBM, \text{surface}}$ (a). (a) is measured from the valence band photoemission spectra of InP and Au. (b) is calculated from the doping concentration of the sample.

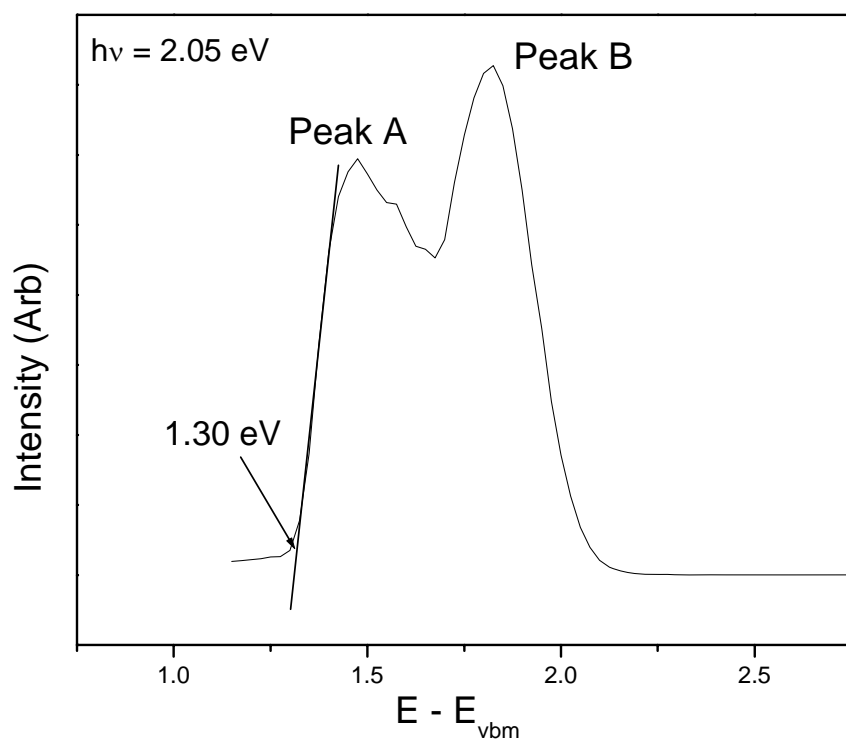


Figure 4.7 Energy distribution curve of InP photocathode at 2.05 eV photon energy with 4 V bias between the sample and the electron energy analyzer.

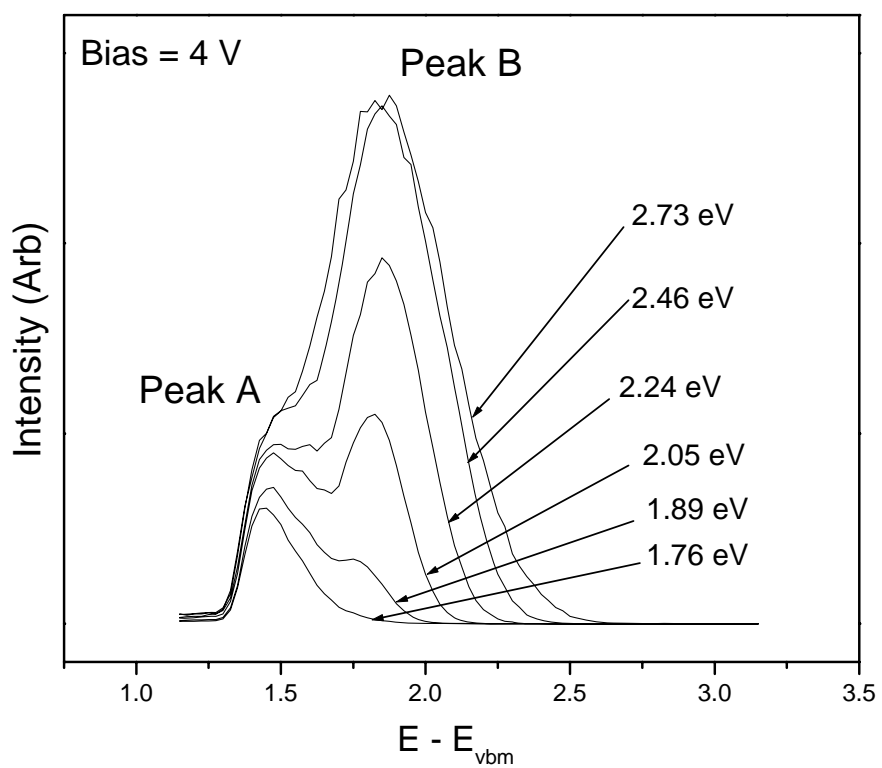


Figure 4.8 Energy distribution curves taken at different photon energy. Applied bias was 4V. All of spectra are normalized by the number of photons.

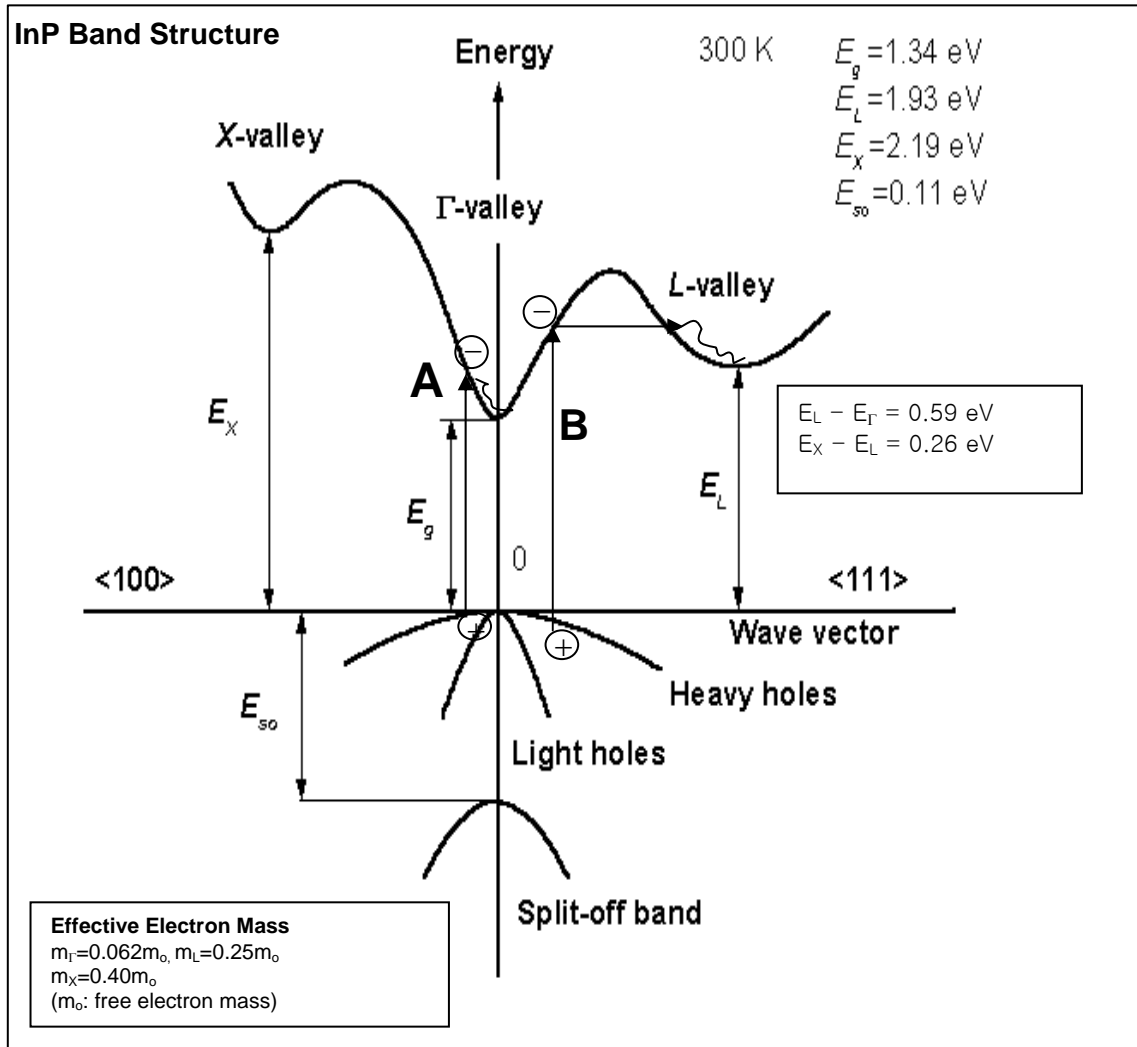


Figure 4.9 InP band structure

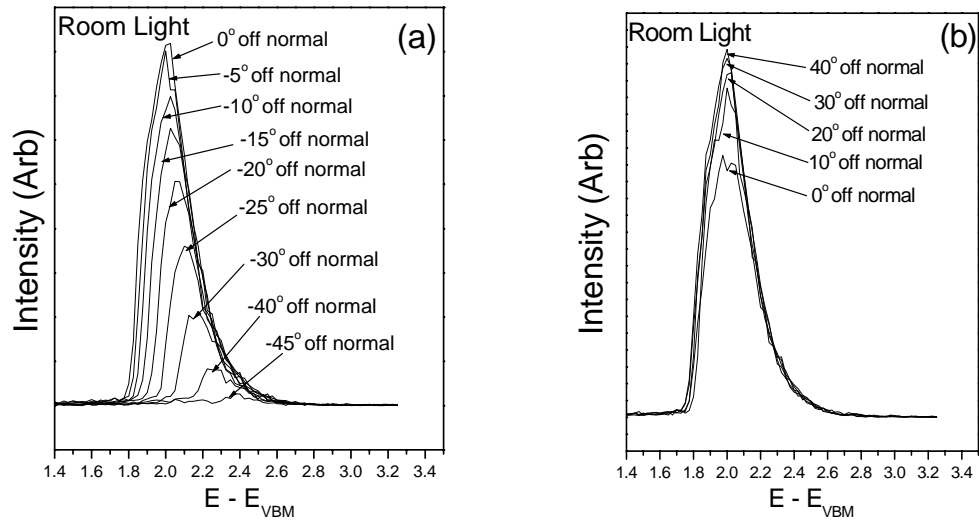


Figure 4.10 Angle-Dependent Energy Distribution Curve (AREDC) of InP

photocathodes with room light (a) off-normal emission angles in one way (b) off-normal angles in the other way

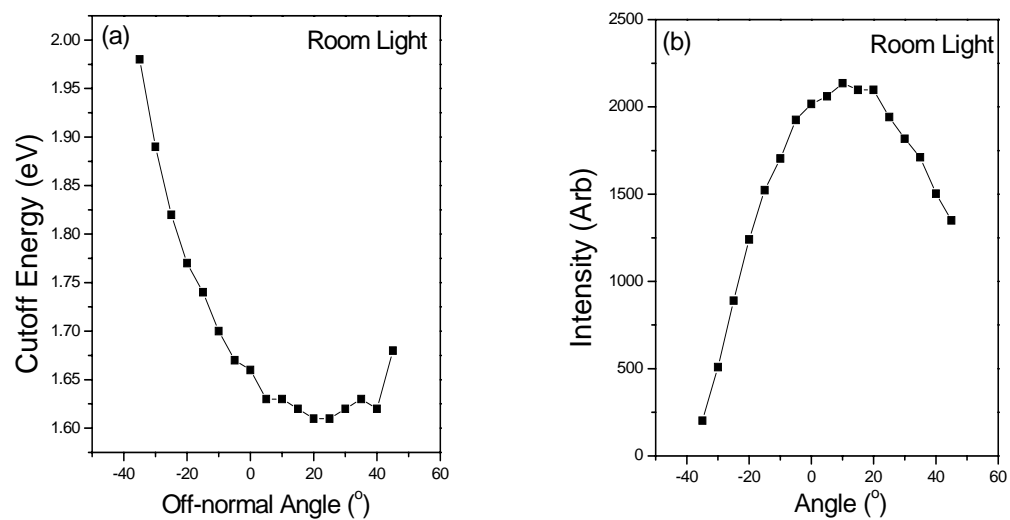


Figure 4.11 InP photocathode activated by Cs/O. (a) Low energy cutoff of EDC at different off-normal angle (b) Intensity of EDC at different off-normal angle

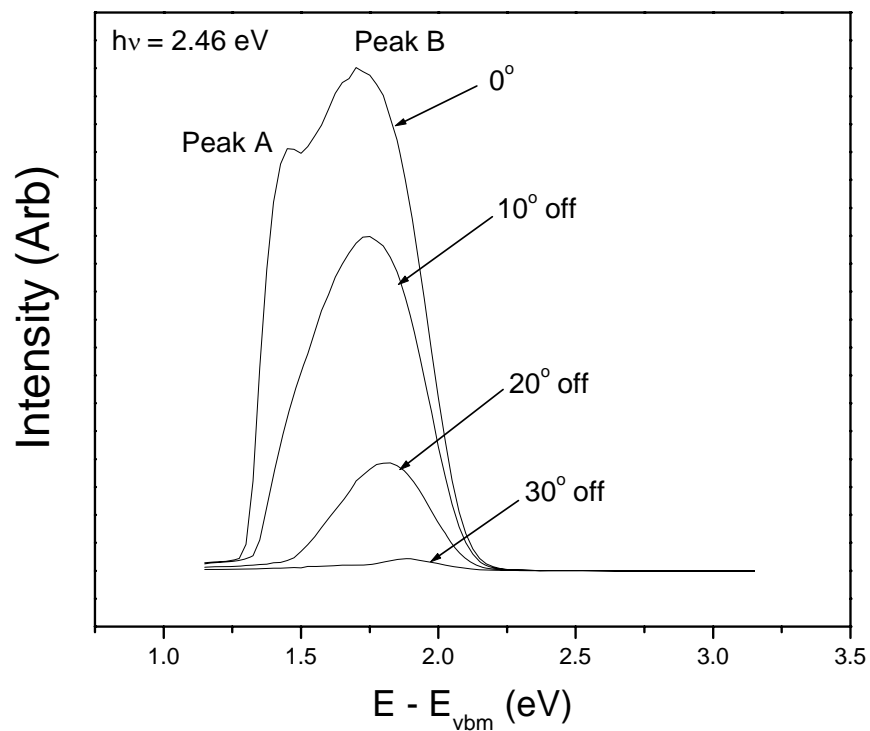


Figure 4.12 Angular Dependent Energy Distribution Curve (ADEDC) of InP photocathode with 500 nm (2.46 eV) light excitation at 4V bias. All the angles are shifted by 15° to compensate the deflection we observed in our experiments.

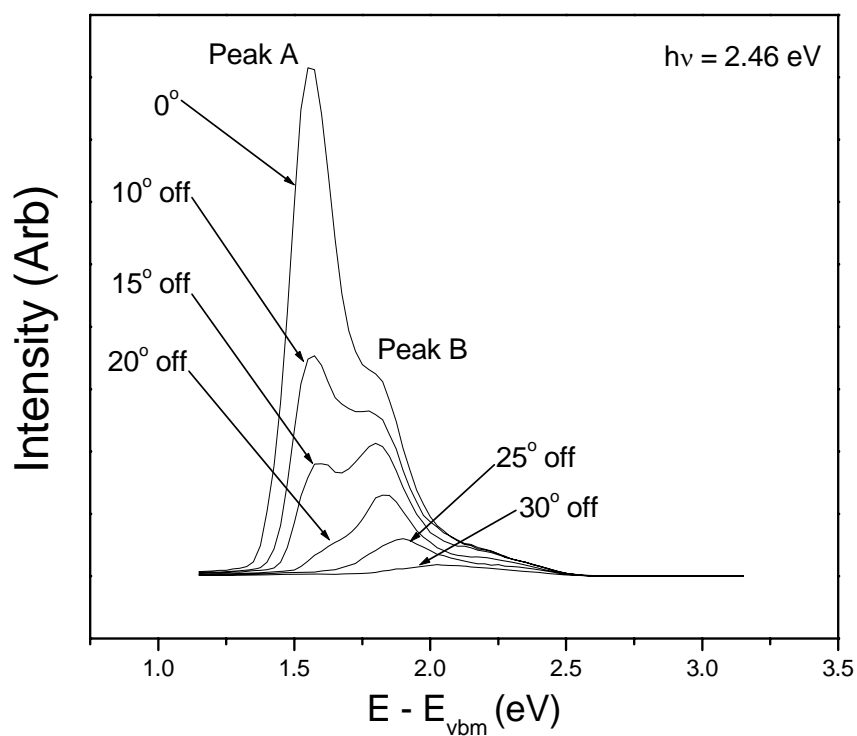


Figure 4.13 Angle-Dependent Energy Distribution Curve (ADEDC) of GaAs photocathodes with 500 nm (2.46 eV) light excitation at 4V bias. All the angles are shifted by 15° to compensate the deflection we observed in our experiments.

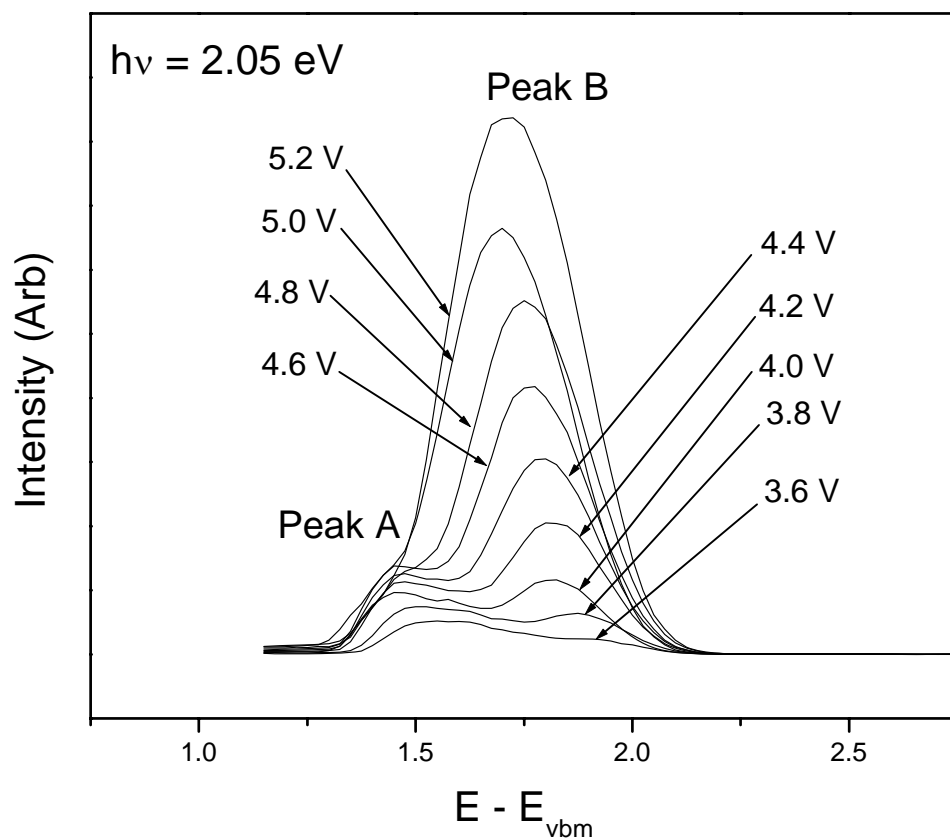


Figure 4.14 Energy distribution curves taken with different biases. Photon energy was 2.05 eV. All of spectra was normalized by the number of photons.

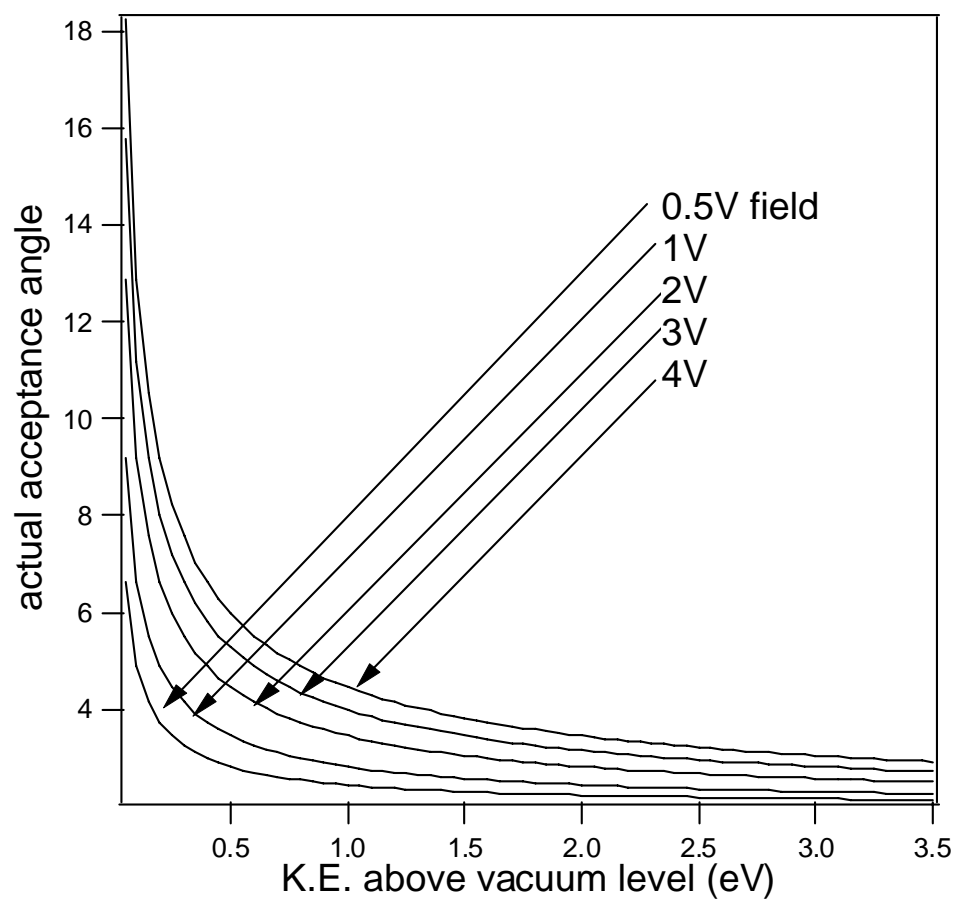


Figure 4.15 The effect of the electric field between the sample and the electron energy analyzer on the effective acceptance angle of the analyzer.

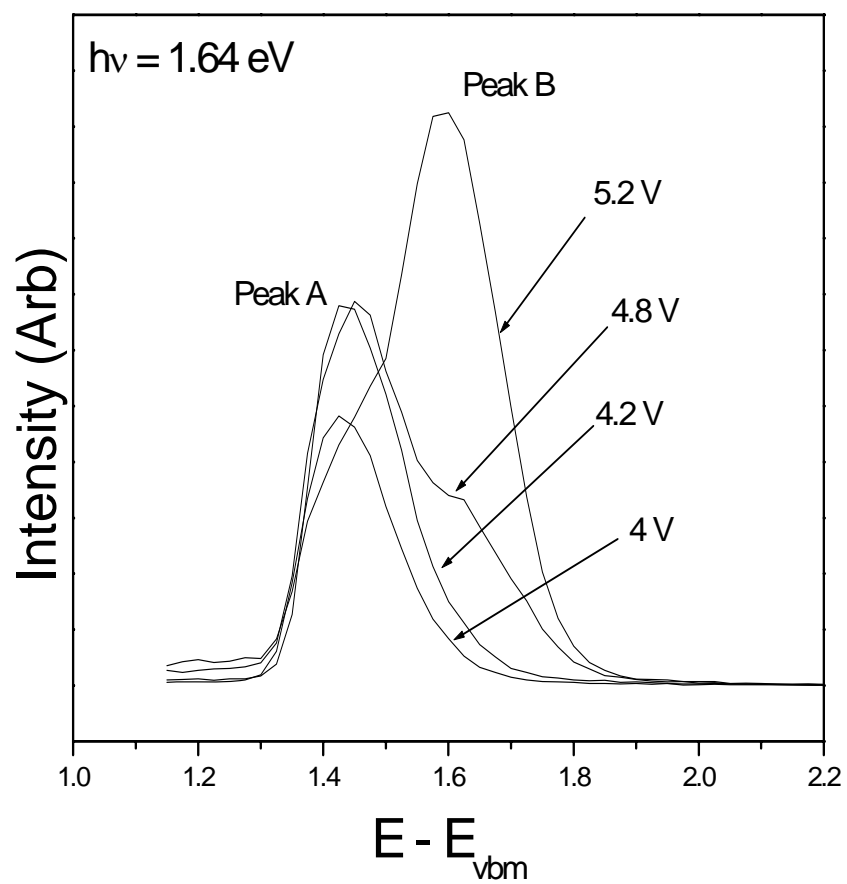


Figure 4.16 The effect of bias on energy distributions at low photon energy (1.64 eV). L valley electrons are observed even though the excitation energy is too low.

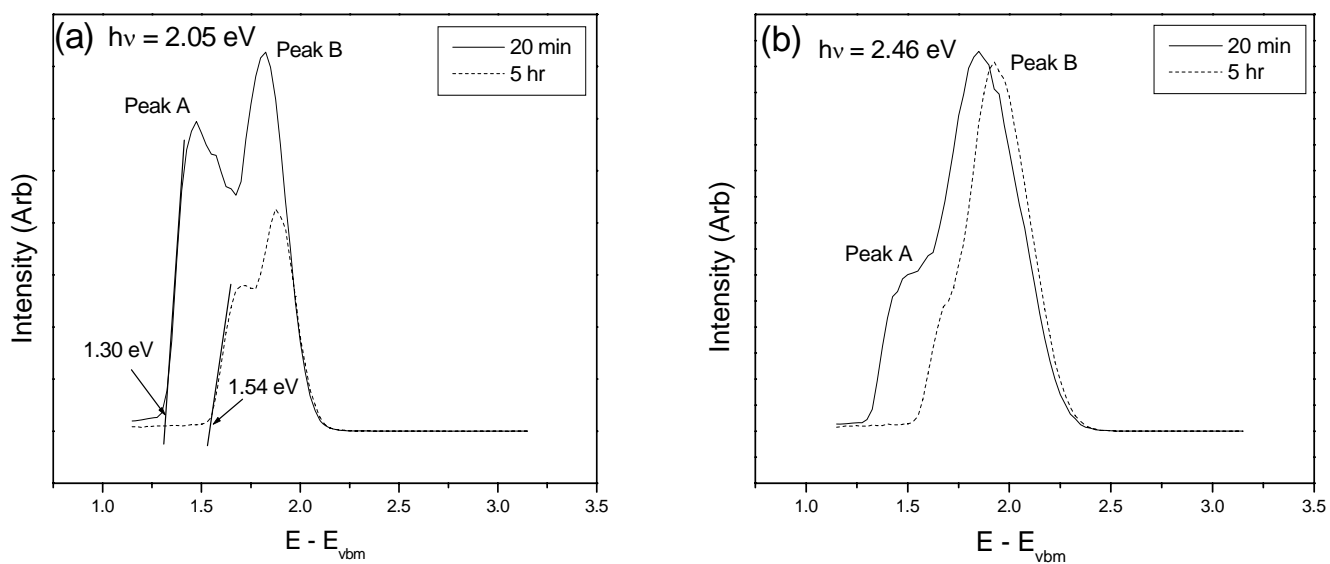


Figure 4.17 (a) EDCs of 2.05 eV photon energy at different times after the completion of activation (20 minutes and 5 hours) (b) EDCs of 2.46 eV photon energy at different time after the completion of activation (20 minutes and 5 hours)

5. CONCLUSIONS

5.1 Overview

InP has become the most important III-V material for long-wavelength NEA photocathodes and high-power and speed devices. The surface chemistry of the Cs/O layer and its interaction with the substrate are important pieces of information, if one wishes to design a reliable and highly-efficient photocathode; and the energy and angular distributions of photoelectrons in InP photocathodes are essential to improving the directionality and brightness of any out-coming electron beam. We utilized synchrotron radiation photoemission spectroscopy (SR-PES) to investigate the activated surface of InP. We also performed SR-PES during decay to elucidate QE decay and its relationship to the chemical changes of the Cs/O layer and substrate, which provided an experimental way to achieve a stable photocathode in an open UHV system. We developed a laterally-distributed model of Cs oxides in an Cs/O layer to explain the activation and decay phenomena, which we observed within our PES data. We measured energy distribution curves (EDC) with near band-gap excitations. We found that the InP photocathode has a highly-directional emission property and the uniqueness of the band structure of InP explains the angle-dependent EDC results.

5.2 Contributions

To date, the chemical species in the Cs/O activation layer and their molecular arrangements have remained unclear. We discovered that the Cs/O activation layer is very thin, less than 1 nm, and that there are two different molecular species of Cs oxide in

that layer: Cs superoxides (CsO_2) and Cs peroxides (Cs_2O_2). According to our angle-dependent photoemission study, oxygen molecules in Cs superoxides are located deeper in the Cs/O layer than the oxygen molecules in Cs peroxides. Since the activation layer is very thin, the oxides are laterally distributed in the layer. Our model, which has oxygen molecules in the same layer of Cs for Cs superoxides, and in-between Cs layers for Cs peroxides, is in accordance with the experimental data.

We also discovered that the NEA photocathode surface is vulnerable to surface contamination, which leads to the weakening of surface dipoles, resulting in increases in the vacuum level and the level of QE decay. The initial QE decay is due to the transformation of oxides from Cs peroxides to Cs superoxides, which are more stable thermodynamically. The later stage of decay is caused by oxidation of the substrate. The number of peroxides molecules decreases in an exponential way, due to a first order thermodynamic reaction of chemical transformations. The time constant of one decay experiment was 32.7 hours, which was consistent with the estimated time we need to have 1 ML of oxygen molecules on the surface.

We determined that the recesiation technique (repetitive depositions of Cs during decay) is effective in maintaining the QE at a certain level in our open UHV system. The O1s core level spectra taken during recesiation show no significant changes in peroxide and superoxide peaks, which indicates that the chemical transformation from Cs peroxide to Cs superoxide is suppressed by recesiation. We decoupled the vacuum level increase into Δ_1 , which is due to substrate oxidation, and Δ_2 , which is due to the chemical transformation in the Cs/O layer. This explains the partial recovery of QE after a long duration of decay, because the QE decay due to substrate oxidation is not reversible.

Redeposited Cs atoms recover some partial dipoles in the Cs/O layer and prevent Cs peroxides from transforming to Cs superoxides, by acting as a protective layer against residual oxygen molecules in the chamber.

The carrier scattering and energy loss properties of InP photocathodes also were studied. We observed two different kinds of photoelectrons arising from InP photocathodes by means of near-band gap excitation. According to the energy resolved energy distribution measurements, one kind of electrons, which comprise the lower KE peak, is electrons thermalized at the bottom of the Γ valley. The other type comprises electrons responsible for the higher KE peak, and represents electrons transferred to the L valley. The maximum emission angle of InP Photocathodes is 30° , which is a highly-directional emission. The remaining photoelectrons, at large emission angles, mostly are from the L valley.

5.3 Future Work

The stability of small band-gap photocathodes, such as InP, must be improved to achieve practical applications. A few possible approaches exist to avoid the rapid decay of QE and prolong lifespan.

Oxygen is essential to lowering the vacuum level further after Cs-only deposition. Oxygen, however, oxidizes the substrate and reduces the charge transfer between Cs and substrate. Some alternative gas, which is less reactive than oxygen, would help to achieve prolonged stability, if that gas can play a similar role to oxygen. NF_3 is a good candidate for this alternative activation gas, but success with it, to date, has been limited.

Finding an alternative gas requires that we attain a better understanding of the oxygen molecules that exist in the Cs/O activation layer. A DFT calculations of Cs oxides, in parallel to the experiments described here, would be extremely helpful in elucidating the role of oxygen molecules in the activation layer.

Lastly, an automatic loop of recesiation in an open UHV system would be effective in prolonging cathode lifespan, according to our recesiation study, if some way can be identified to sensitively supply additional Cs atoms to the surface.